Characterization of Proton-Exchanged and Annealed Planar Optical Lithium Tantalate Waveguides

Dennis Kan

Department of Electrical Engineering

McGill University

Montreal, Quebec

July 19, 1993

A Thesis submitted to the Faculty of Graduate Studies and Research in partial fulfillment of the requirements for the degree Master of Engineering

Name Dennis Kan

Dissertation Abstracts International is arranged by broad, general subject categories Please select the one subject which most nearly describes the content of your dissertation Enter the corresponding four-digit code in the spaces provided

ENGINEERING, Electronics and Electrical — SUBJECT TERM

0544 — SUBJECT CODE

UMI

Subject Categories

THE HUMANITIES AND SOCIAL SCIENCES

COMMUNICATIONS AND THE ARTS
- Architecture 0729
- Art History 0377
- Cinema 0900
- Dance 0378
- Fine Arts 0357
- Information Science 0723
- Journalism 0391
- Library Science 0399
- Mass Communications 0708
- Music 0413
- Speech Communication 0459
- Theater 0465

EDUCATION
- General 0515
- Administration 0514
- Adult and Continuing 0516
- Agricultural 0517
- Art 0273
- Bilingual and Multicultural 0282
- Business 0688
- Community College 0275
- Curriculum and Instruction 0727
- Early Childhood 0518
- Elementary 0524
- Finance 0277
- Guidance and Counseling 0519
- Health 0680
- Higher 0745
- History of 0520
- Home Economics 0278
- Industrial 0521
- Language and Literature 0279
- Mathematics 0280
- Music 0522
- Philosophy of 0998
- Physical 0523
- Psychology 0525
- Reading 0535
- Religious 0527
- Sciences 0714
- Secondary 0533
- Social Sciences 0534
- Sociology of 0340
- Special 0529
- Teacher Training 0530
- Technology 0710
- Tests and Measurements 0288
- Vocational 0747

LANGUAGE, LITERATURE AND LINGUISTICS
- Language
  - General 0679
  - Ancient 0289
  - Linguistics 0290
  - Modern 0291
- Literature
  - General 0401
  - Classical 0294
  - Comparative 0295
  - Medieval 0297
  - Modern 0298
  - African 0316
  - American 0591
  - Asian 0305
  - Canadian (English) 0352
  - Canadian (French) 0355
  - English 0593
  - Germanic 0311
  - Latin American 0312
  - Middle Eastern 0315
  - Romance 0313
  - Slavic and East European 0314

PHILOSOPHY, RELIGION AND THEOLOGY
- Philosophy 0422
- Religion
  - General 0318
  - Biblical Studies 0321
  - Clergy 0319
  - History of 0320
  - Philosophy of 0322
- Theology 0469

SOCIAL SCIENCES
- American Studies 0323
- Anthropology
  - Archaeology 0324
  - Cultural 0326
  - Physical 0327
- Business Administration
  - General 0310
  - Accounting 0272
  - Banking 0770
  - Management 0454
  - Marketing 0338
- Canadian Studies 0385
- Economics
  - General 0501
  - Agricultural 0503
  - Commerce Business 0505
  - Finance 0508
  - History 0509
  - Labor 0510
  - Theory 0511
- Folklore 0358
- Geography 0366
- Gerontology 0351
- History
  - General 0578
  - Ancient 0579
  - Medieval 0581
  - Modern 0582
  - Black 0328
  - African 0331
  - Asia, Australia and Oceania 0332
  - Canadian 0334
  - European 0335
  - Latin American 0336
  - Middle Eastern 0333
  - United States 0337
- History of Science 0585
- Law 0398
- Political Science
  - General 0615
  - International Law and Relations 0616
  - Public Administration 0617
- Recreation 0814
- Social Work 0452
- Sociology
  - General 0626
  - Criminology and Penology 0627
  - Demography 0938
  - Ethnic and Racial Studies 0631
  - Individual and Family Studies 0628
  - Industrial and Labor Relations 0629
  - Public and Social Welfare 0630
  - Social Structure and Development 0700
  - Theory and Methods 0344
- Transportation 0709
- Urban and Regional Planning 0999
- Women s Studies 0453

THE SCIENCES AND ENGINEERING

BIOLOGICAL SCIENCES
- Agriculture
  - General 0473
  - Agronomy 0285
  - Animal Culture and Nutrition 0475
  - Animal Pathology 0476
  - Food Science and Technology 0359
  - Forestry and Wildlife 0478
  - Plant Culture 0479
  - Plant Pathology 0480
  - Plant Physiology 0817
  - Range Management 0777
  - Wood Technology 0746
- Biology
  - General 0306
  - Anatomy 0287
  - Biostatistics 0308
  - Botany 0309
  - Cell 0379
  - Ecology 0329
  - Entomology 0353
  - Genetics 0369
  - Limnology 0793
  - Microbiology 0410
  - Molecular 0307
  - Neuroscience 0317
  - Oceanography 0416
  - Physiology 0433
  - Radiation 0821
  - Veterinary Science 0778
  - Zoology 0472
- Biophysics
  - General 0786
  - Medical 0760

EARTH SCIENCES
- Biogeochemistry 0425
- Geochemistry 0996
- Geodesy 0370
- Geology 0372
- Geophysics 0373
- Hydrology 0388
- Mineralogy 0411
- Paleobotany 0345
- Paleoecology 0426
- Paleontology 0418
- Paleozoology 0985
- Palynology 0427
- Physical Geography 0368
- Physical Oceanography 0415

HEALTH AND ENVIRONMENTAL SCIENCES
- Environmental Sciences 0768
- Health Sciences
  - General 0566
  - Audiology 0300
  - Chemotherapy 0992
  - Dentistry 0567
  - Education 0350
  - Hospital Management 0769
  - Human Development 0758
  - Immunology 0982
  - Medicine and Surgery 0564
  - Mental Health 0347
  - Nursing 0569
  - Nutrition 0570
  - Obstetrics and Gynecology 0380
  - Occupational Health and Therapy 0354
  - Ophthalmology 0381
  - Pathology 0571
  - Pharmacology 0419
  - Pharmacy 0572
  - Physical Therapy 0382
  - Public Health 0573
  - Radiology 0574
  - Recreation 0575
  - Speech Pathology 0460
  - Toxicology 0383
- Home Economics 0386

PHYSICAL SCIENCES

Pure Sciences
- Chemistry
  - General 0485
  - Agricultural 0749
  - Analytical 0486
  - Biochemistry 0487
  - Inorganic 0488
  - Nuclear 0738
  - Organic 0490
  - Pharmaceutical 0491
  - Physical 0494
  - Polymer 0495
  - Radiation 0754
- Mathematics 0405
- Physics
  - General 0605
  - Acoustics 0986
  - Astronomy and Astrophysics 0606
  - Atmospheric Science 0608
  - Atomic 0748
  - Electronics and Electricity 0607
  - Elementary Particles and High Energy 0798
  - Fluid and Plasma 0759
  - Molecular 0609
  - Nuclear 0610
  - Optics 0752
  - Radiation 0756
  - Solid State 0611
- Statistics 0463

Applied Sciences
- Applied Mechanics 0346
- Computer Science 0984
- Engineering
  - General 0537
  - Aerospace 0538
  - Agricultural 0539
  - Automotive 0540
  - Biomedical 0541
  - Chemical 0542
  - Civil 0543
  - Electronics and Electrical 0544
  - Heat and Thermodynamics 0348
  - Hydraulic 0545
  - Industrial 0546
  - Marine 0547
  - Materials Science 0794
  - Mechanical 0548
  - Metallurgy 0743
  - Mining 0551
  - Nuclear 0552
  - Packaging 0549
  - Petroleum 0765
  - Sanitary and Municipal 0554
  - System Science 0790
- Geotechnology 0428
- Operations Research 0796
- Plastics Technology 0795
- Textile Technology 0994

PSYCHOLOGY
- General 0621
- Behavioral 0384
- Clinical 0622
- Developmental 0620
- Experimental 0623
- Industrial 0624
- Personality 0625
- Physiological 0989
- Psychobiology 0349
- Psychometrics 0632
- Social 0451

Master's Thesis Title: Characterization of proton-exchanged and annealed planar optical lithium tantalate waveguides

Author: Dennis Kan, Department of Electrical Engineering

Shortened Title: Characterization of proton-exchanged and annealed $LiTaO_3$ waveguides

For my parents, Raymond and Gemma Kan

Résumé

Des guides d'ondes optiques plan ont été fabriqués dans un substrat de $LiTaO_3$ coupé selon l'axe z par l'échange protonique dans l'acide pyrophosphorique et par la recuisson. Leurs profils de l'indice ont été mesurés, et les paramètres du profil de l'indice ont été reliés aux conditions de fabrication. Ces données seront très utiles pour la conception et fabrication des guides optiques.

Une fonction "step" est utilisée pour modeler le profil de l'indice après l'échange protonique avec précision. La profondeur d_{pe} et l'augmentation de l'indice Δn_e ont été reliés à la température et au temps d'échange au moyen d'équations empiriques. Les pertes de propagation ont aussi été mesurées, et des instabilités de l'indice peuvent être observées.

Une fonction "Gaussienne généralisée" a été utilisée pour modeler le profil de l'indice tout au long de la recuisson avec précision. La profondeur d et l'augmentation de l'indice de surface Δn_s sont reliées au temps de la recuisson par des équations empiriques. Les paramètres de ces équations dépendent aux conditions d'échange et à la température de la recuisson, et les équations qui décrivent cette relation sont établies. Un critère pour obtenir des guides stables est établi. Un modèle mathématique et une simulation numérique de la recuisson sont proposés pour élucider le phénomène de l'augmentation de l'indice de surface.

L'échange protonique avec l'acide diluée offre le possibilité de faire les guides d'ondes avec des profils de l'indice qui ne sont pas possible en utilisant l'acide pur.

Abstract

Planar z-cut $LiTaO_3$ waveguides were fabricated by proton-exchange in pyrophosphoric acid and post-exchange annealing. Their refractive index profiles were measured, and the index profile parameters were related to fabrication conditions. This data will be useful for the design and fabrication of single and multi-moded waveguides and devices.

A step function was found to accurately model the index profile after proton-exchange. Empirical equations relating the waveguide depth d_{pe} and the extraordinary index increase Δn_e to the exchange temperature and time were found. Propagation losses were measured, and index instabilities were detected.

The generalized Gaussian function can be used to accurately model the index profile throughout annealing. Empirical equations relating the depth d and the surface index increase Δn_s to the anneal time were found. Additional empirical relations, establishing the dependence of the parameters of the equations on the anneal temperature and proton exchange conditions, were also found. A criterion for eliminating index instabilities in the waveguide was established, and propagation losses were measured. Mathematical modelling and numerical simulation of annealing was attempted in order to gain insight into the phenomenon of the surface index increase.

Proton-exchange with buffered melts offer the possibility of fabricating waveguides with index profiles that are not possible if using concentrated melts.

Acknowledgements

I would like to thank Professor Gar Lam Yip, my supervisor, for his help and advice on all aspects of this thesis.

I am indebted to John Nikolopoulos, whose master's thesis, "Characterization of Proton-Exchanged Planar Optical Waveguides in $LiNbO_3$", has been an important guide, model and precursor to this one.

My colleagues in the McGill Guided-Wave Optics Laboratory, Philippe Allard, Loic Babin, Jian-Yao Chen, Peter Noutsios, Li Zhong Sun, and Feng Xiang, have provided me with invaluable assistance throughout my stay. Their knowledge and experience helped me through many problems, and I appreciate very much their help and their friendship.

Finally, I thank the Natural Sciences and Engineering Research Council for two years of financial support in the form of a NSERC Post Graduate Fellowship, and an operating grant for all the material and equipment support of this research.

Contents

List of Figures

List of Tables

List of Symbols

a : shape parameter in the generalized Gaussian and Fermi functions

ar_{pe} : the area of the index profile after proton-exchange; $ar_{pe} = \Delta n_e \times d_{pe}$

ar_{pl} : the plateau area - the value at which the area under the index profile stabilizes

α : propagation loss (dB/cm)

b : annealing constant used in $\Delta d = b\, t_a^c$

β : light wave propagation constant (rads/m)

c : annealing constant used in $\Delta d = b\, t_a^c$

d : current waveguide depth (also denotes depth throughout annealing)

d_{pe} : waveguide depth after proton-exchange

d_{pk} : waveguide depth at the Δn_s peak

Δd : change in the waveguide depth due to annealing; $\Delta d = d - d_{pe}$

D_e : effective diffusion coefficient for proton-exchange

D_0 : diffusion constant in expression for diffusion coefficient

e : annealing constant used in $\Delta n_s = \Delta n_e + e t_a^f$

E_a : activation energy (eV)

f : annealing constant used in $\Delta n_s = \Delta n_e + e t_a^f$

g : annealing constant used in $\Delta n_s = \Delta n_{pk} + e t_a^f$

k : free space wave number (m^{-1}) or Boltzmann's constant (eV/K)

n_b : the substrate refractive index

n_{eff} : the effective index of a propagating mode; $n_{eff} = \beta/k$

n_e : extra-ordinary index of refraction

n_o : ordinary index of refraction

n_s : the refractive index at the waveguide's surface

Δn_e : the increase in the extra-ordinary index after proton-exchange; $\Delta n_e = n_s - n_b$

Δn_s : n_s - n_b (Δn_s changes throughout annealing)

Δn_{pk} : the peak Δn_s during annealing

p_1, p_2 : parameters in the H-OH to OH ion rate of conversion equation

q_1, q_2 : parameters in the diffusion coefficient function $D_{OH}(C_{OH})$

r : grid constant used in annealing simulation: $r = \frac{\Delta t}{\Delta z^2}$

t_a : duration of annealing

t_{pe} : duration of proton-exchange

t_{pk} : the time during annealing when Δn_s reaches its peak

T_a : annealing temperature

T_c : Curie temperature

T_{pe} : proton-exchange temperature

Chapter 1

Introduction

1.1 Integrated Optics

The field of integrated optics deals with the control, manipulation, and interaction of light phenomena on planar optical substrates. Information is encoded in light signals instead of electrical signals or radio waves, and the light is conducted by optical waveguides instead of metal wires. Some advantages of an integrated optical circuit (IOC) include high bandwidth, low susceptibility to electromagnetic interference, and small size. Often an IOC is an opto-electronic device residing on an optical substrate, where electro-optic interactions are used to combine electrical signal processing with light transmission. Typical IOC's include phase/amplitude modulators, filters, switches, power dividers, de/multiplexers, couplers, and rf spectrum analysers, etc.

Integrated optics emerged in the late 1960's [1]. Interest in the field accelerated in the 1970's, spurred on by the development of optical fibers, advances in laser diode technology, and the realization of photolithographic techniques capable of submicron linewidths. Many fabrication techniques for IOC's are similar to the ones found in semiconductor IC technology. The field has grown tremendously in the last twenty years, and integrated optic devices are now used in military systems, avionic systems, remote sensing and fault detection applications, and perhaps most prominently, the telecommunications industry.

The field of integrated optics can be organized according to the substrate material, because the form and function of an optical circuit depends very much on a substrate's properties. Below is a table comparing different substrate materials and their properties:

material category	glass	inorganic oxide crystals	III-V semiconductors	organic polymers
examples	SF-6 BK-7	**lithium tantalate** lithium niobate	GaAs AlGaIs	PMMA polyurethane
light source on substrate	No	No	Yes	No
electro-optic interaction	No	Yes	Yes	No
applications	passive devices	electro-optic and acousto-optic devices	monolithically integrated devices	non-linear optics

Table 1.1: Different optical substrates

1.2 Proton-Exchange and Lithium Tantalate

In the 1970's and early 80's, lithium tantalate languished in relative obscurity while lithium niobate, a closely related material, basked in the attention of many researchers. A successful waveguide fabrication process (i.e. the titanium in-diffusion process) was found for $LiNbO_3$, but the same process required complicated modifications for $LiTaO_3$. In 1982, proton-exchange was successfully demonstrated for $LiNbO_3$ [2], followed by $LiTaO_3$ in 1983 [3]. Proton-exchange is rapidly gaining prominence as a waveguide fabrication technique due to its simplicity, low cost, and some improved performance characteristics [4, 5] (see Section 3.3). With the discovery of a suitable fabrication technique, lithium tantalate began to receive closer scrutiny. Lithium tantalate has a very high resistance to optical damage, which renders it eminently suitable for high power and short wavelength applications. Research into proton-exchanged $LiTaO_3$ devices is gaining momentum, and some advanced devices have already been realized on $LiTaO_3$.

Proton-exchange in $LiNbO_3$ has been well characterized and investigated, but similar work in $LiTaO_3$ has been much less extensive. The characterization studies for $LiTaO_3$ are few and often sketchy, and some of the constants and parameters found are not in full agreement with each other [6, 7, 8, 9] (see also Table 7.5). Post-exchange annealing, one of two methods (the other being buffered proton-exchange) for eliminating instabilities and restoring electro-optic performance after proton-exchange, has scarcely received any attention. Clearly, proton-exchanged (PE) and annealed proton-exchanged (APE) $LiTaO_3$ waveguides merit more extensive investigation. The wealth of potential applications for lithium tantalate and the utility of the proton-exchange technique provide the impetus for conducting research in this area.

1.3 Research Objective

The basic goal of this research is to characterize planar optical waveguides fabricated by proton-exchange in lithium tantalate substrates. Accurate fabrication data and characterization results are the foundation for further work. By relating the fabrication conditions to the waveguide's refractive index profile, this study will provide valuable information needed for the design, optimization, and fabrication of more complicated devices on lithium tantalate. Specifically, this thesis attempts to address the following issues:

- **the lack of detailed characterization data for proton-exchange with pyrophosphoric acid in $LiTaO_3$**
- **the lack of characterization data for post-exchange annealing**
- whether pyrophosphoric acid produces waveguides with better properties than benzoic acid, as is the case for $LiNbO_3$
- whether a Fermi or generalized Gaussian index profile model is more accurate than the conventional step-index approximation

- proton-exchange with buffered pyrophosphoric acid, which has not been reported in the literature before

1.4 Original Contributions

- A careful and detailed characterization of planar z-cut $LiTaO_3$ waveguides proton-exchanged in pyrophosphoric acid and buffered pyrophosphoric acid, relating index profile parameters to exchange conditions.
- A careful and detailed characterization of the effects of annealing on proton-exchanged and buffered proton-exchanged waveguides, relating changes in the refractive index profile to the proton-exchange and annealing conditions.
- The development of a mathematical model of annealing in $LiTaO_3$, along with a computer-programmed numerical simulation.

1.5 Thesis Organization

This thesis presents and develops the subject in a coherent and organized manner. Chapter 2 introduces the reader to optical waveguiding. Chapters 3 and 4 survey and summarize the experimental results, theories, explanations, and current developments in proton-exchange and annealing. Chapter 5 describes the experimental procedures and measurement techniques used, and Chapter 6 presents the various analysis and reduction methods performed on the raw data. Chapter 7 is the heart of the thesis, containing experimental data, graphs, tables, plus an analysis and discussion of the results. How the empirically derived formulae and tables can be used to help design and fabricate waveguides is shown. Finally, Chapter 8 concludes by summarizing the results and insights gained from this research. (In addition, Appendix A presents a mathematical model of annealing in $LiTaO_3$, and the results from a numerical simulation based on the model.)

Chapter 2

Optical Planar Waveguides

2.1 Introduction

This chapter presents the theory and mathematical formulation of light propagation in planar waveguides. We begin our derivation with Maxwell's equations, and then make the pertinent assumptions in order to simplify the equations. In this way, we arrive at the scalar wave equation. Exact analytical solutions exist only for a small number of profiles. As an example, we examine the solution for the step profile. For the more general case, approximate methods for solving the wave equation are discussed.

2.2 Derivation of the Wave Equation

We begin with Maxwell's equations:

$$\nabla \times \vec{E}(\vec{r},t) = -\frac{\partial \vec{B}(\vec{r},t)}{\partial t} \tag{2.1}$$

$$\nabla \times \vec{H}(\vec{r},t) = \vec{J}(\vec{r},t) + \frac{\partial \vec{D}(\vec{r},t)}{\partial t} \tag{2.2}$$

$$\nabla \cdot \vec{D}(\vec{r},t) = \rho \tag{2.3}$$

$$\nabla \cdot \vec{B}(\vec{r},t) = 0 \tag{2.4}$$

$$\nabla \cdot \vec{J}(\vec{r},t) + \frac{\partial \rho(\vec{r},t)}{\partial t} = 0 \tag{2.5}$$

where $\vec{E}$ is the electric field, $\vec{H}$ the magnetic field, $\vec{D}$ the electric displacement, $\vec{B}$ the magnetic displacement, $\vec{J}$ the current source, ρ the free electric charge, $\vec{r}$ the position vector in space, and t the time dependence. We can reduce these equations by making several assumptions relevant to light propagation in planar waveguides. First we assume that the fields are time-harmonic, sinusoidally oscillating at a frequency of ω (radians/s). This is true for the laser light sources used in this work. We use a phasor representation and the time derivatives $\partial/\partial t$ may be replaced by $j\omega$. We also assume that the light propagates in a source free ($\rho = 0$), lossless and isotropic media. Though $LiTaO_3$ is an anisotropic material, the effect of anisotropy may be neglected if the birefringence is small [10]. The first two equations then reduce to

$$\nabla \times \vec{E}(\vec{r}) = -j\omega\mu\vec{H}(\vec{r}) \tag{2.6}$$

$$\nabla \times \vec{H}(\vec{r}) = j\omega\epsilon\vec{E}(\vec{r}) \tag{2.7}$$

where μ is the magnetic permeability, and ϵ the electric permittivity. In free space, $\mu = \mu_0 = 4\pi \times 10^{-7}$ H/m and $\epsilon = \epsilon_0 = 8.85 \times 10^{-12}$ F/m. To simplify further, we take the curl of the first equation and substitute this into the second to eliminate $\vec{H}(\vec{r})$:

$$\nabla \times [\nabla \times \vec{E}(\vec{r})] = -j\omega\mu\nabla \times \vec{H}(\vec{r}) = \omega^2\mu\epsilon\vec{E}(\vec{r}) \tag{2.8}$$

To simplify this equation, we use the vector identity

$$\nabla \times [\nabla \times \vec{E}(\vec{r})] = \nabla[\nabla \cdot \vec{E}(\vec{r})] - \nabla^2\vec{E}(\vec{r}) \tag{2.9}$$

Since $\rho = 0$, then $\nabla \cdot \vec{E}(\vec{r}) = 0$, therefore

$$\nabla \times [\nabla \times \vec{E}(\vec{r})] = -\nabla^2\vec{E}(\vec{r}) \tag{2.10}$$

Substituting this into the previous equation, we obtain the wave equation

$$\nabla^2\vec{E}(\vec{r}) + \omega^2\mu\epsilon\vec{E}(\vec{r}) = 0 \tag{2.11}$$

which when expanded gives us

$$(\frac{\partial^2}{\partial x^2} + \frac{\partial^2}{\partial y^2} + \frac{\partial^2}{\partial z^2})\vec{E}(\vec{r}) + \omega^2\mu\epsilon\vec{E}(\vec{r}) = 0 \tag{2.12}$$

Now let us assume plane wave propagation in the z direction. The field is periodic in the z and independent of y. Therefore,

$$\vec{E}(\vec{r},t) = \vec{E}(x,y,z,t) = \vec{E}(x)e^{j(\omega t - \beta z)} \tag{2.13}$$

$$\frac{\partial^2}{\partial z^2}\vec{E}(\vec{r}) = -\beta^2\vec{E}(\vec{r}) \tag{2.14}$$

where β is the propagation constant of the plane wave (radians/m). Let us define k as the wave number (m^{-1}), such that

$$k \equiv \omega\sqrt{\mu_0\epsilon_0} = \frac{2\pi}{\lambda} \tag{2.15}$$

and λ is the wavelength (m). The index of refraction n is defined as $n = \sqrt{\epsilon/\epsilon_0}$ and it may vary with x. Thus $k^2n^2(x) = \omega^2\mu\epsilon$, and we arrive at the one-dimensional wave equation:

$$\frac{\partial^2\vec{E}}{\partial x^2} + (k^2n^2(x) - \beta^2)\vec{E} = 0 \tag{2.16}$$

This wave equation may be decomposed into three separate scalar equations for E_x, E_y, and E_z.

2.3 Modes of Propagation

If we write out each component of this wave equation, noting that all derivatives with respect to y are equal to zero, then we see they are related in the following way:

$$E_x = \frac{\beta}{\omega\epsilon}H_y \tag{2.17}$$

$$E_y = \frac{-j}{\omega\epsilon}(-j\beta H_x - \frac{\partial H_z}{\partial x}) \tag{2.18}$$

$$E_z = \frac{-j}{\omega\epsilon}\frac{\partial H_y}{\partial x} \tag{2.19}$$

$$H_x = \frac{-\beta}{\omega\mu} E_y \tag{2.20}$$

$$H_y = \frac{j}{\omega\mu}(-j\beta E_x - \frac{\partial E_z}{\partial x}) \tag{2.21}$$

$$H_z = \frac{j}{\omega\mu}\frac{\partial E_y}{\partial x} \tag{2.22}$$

Wave propagation may be decomposed into two separate modes. One is called the TE (transverse electric) mode and the other is called the TM (transverse magnetic) mode. The field components of each mode do not depend on those of the other mode, so the two are uncoupled, orthogonal modes.

2.3.1 The TE mode

To derive the TE mode equations, we set $H_y = 0$. From the above relations, we find that also $E_z = 0$ and $E_x = 0$. Thus, only the field components E_y, H_x, and H_z are present and are given by

$$\frac{\partial^2 E_y}{\partial x^2} + (k^2 n^2 - \beta^2) E_y = 0 \tag{2.23}$$

$$H_x = -\frac{\beta}{\omega\mu_0} E_y \tag{2.24}$$

$$H_z = -\frac{1}{j\omega\mu_0}\frac{\partial E_y}{\partial x} \tag{2.25}$$

2.3.2 The TM mode

To derive the TM mode equations, we set $E_y = 0$. From the above relations, we find that also $H_z = 0$ and $H_x = 0$. Thus, only the field components H_y, E_x, and E_z are present and are given by

$$\frac{\partial^2 H_y}{\partial x^2} + (k^2 n^2 - \beta^2) H_y = 0 \tag{2.26}$$

$$E_x = -\frac{\beta}{\omega\epsilon_0 n^2} H_y \tag{2.27}$$

$$E_z = -\frac{1}{j\omega\epsilon_0 n^2}\frac{\partial H_y}{\partial x} \tag{2.28}$$

2.4 The Step-Index Waveguide

After proton-exchange, optical $LiNbO_3$ and $LiTaO_3$ waveguides are generally considered to have a step-index profile. The geometry of the step-index (i.e. slab) waveguide is shown in Figure 2.1. The wave and modal equations were developed with z as the direction of propagation and x as the depth, following the convention. The planar z-cut $LiTaO_3$ waveguides of this study, however, are oriented with z as the depth direction and y as the direction of propagation (according to the crystal's coordinate system). To transpose the previous and the following equations to the orientation of the $LiTaO_3$ waveguides, one simply interchanges x with z, y with x, and z with y.

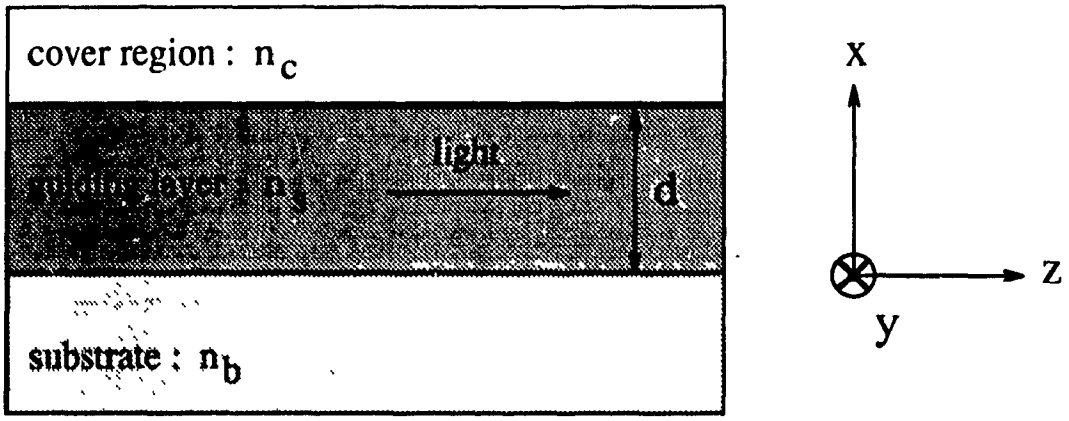

Figure 2.1: The step-index, or slab, waveguide

The guiding layer has an index of n_s and thickness d. Above this layer is the cover region (usally air) with index n_c and below this layer is the substrate with index n_b. To create this guiding layer, usually a dopant is added to the substrate in order to increase its refractive index. Since there are three regions, each with a different refractive index, three scalar wave equations exist. None of the equations depend on x, so an analytic solution is possible. The general field solution to this form of the wave equation is well known [11] and takes the form of a complex exponential. For guided modes, the exponential has a

real power (i.e. field amplitude is exponentially decaying) in the air and substrate regions, and a complex power (i.e. field amplitude is sinusoidal) in the waveguiding layer. For the TE propagation mode, the solution will be in the form:

$$E_y = \begin{cases} E_c exp^{-\gamma_c x} & x > 0 \quad \text{in air} \\ E_s cos(k_x x + \phi_c) & -d < x < 0 \quad \text{in the waveguide} \\ E_b exp^{\gamma_b (x+d)} & x < -d \quad \text{in the substrate} \end{cases} \tag{2.29}$$

If we then define the effective index $n_{eff} = \beta/k$, and substitute these solutions back into the wave equation we get

$$\gamma_c = k\sqrt{n_{eff}^2 - n_c^2} \tag{2.30}$$

$$k_x = k\sqrt{n_s^2 - n_{eff}^2} \tag{2.31}$$

$$\gamma_b = k\sqrt{n_{eff}^2 - n_b^2} \tag{2.32}$$

Matching the tangential field components across the boundaries (at x=0 and x =d) yields

$$E_c = E_s cos(\phi_c) \tag{2.33}$$

$$tan(\phi_c) = \gamma_c/k_x \tag{2.34}$$

$$E_b = E_s cos(k_x d - \phi_c) \tag{2.35}$$

$$tan(k_x d - \phi_c) = \gamma_b/k_x \tag{2.36}$$

By combining these equations, we obtain the dispersion relation, which relates the propagation constant β to physical waveguide parameters. The TM mode can be treated in a similar way by starting from H_y. By taking the inverse tangent of equations 2.34 and 2.36 and rearranging, the dispersion relation for slab waveguides for both TE and TM modes can be expressed as:

$$k_x d - tan^{-1}\left\{\frac{c_1\gamma_b}{k_x}\right\} - tan^{-1}\left\{\frac{c_2\gamma_c}{k_x}\right\} = m\pi \tag{2.37}$$

$$\text{where } c_1 = \begin{cases} 1 & \text{TE mode} \\ (n_b/n_s)^2 & \text{TM mode} \end{cases} \qquad c_2 = \begin{cases} 1 & \text{TE mode} \\ (n_c/n_s)^2 & \text{TM mode} \end{cases} \tag{2.38}$$

This transcendental equation can be solved for β, and hence the effective index n_{eff}, using a numerical root-search technique.

2.5 Dispersion Curves

In our waveguide characterization study, the modal effective indices (i.e. the modal propagation constants) are measured by the prism coupling method. Light is coupled into the waveguide with the aid of high-index prisms. For guided modes, the incident angle of the light can be related to the effective indices. From this data, the waveguide depth d and surface index n_s must be calculated. This is done with the aid of dispersion curves, which plot the effective index n_{eff} against the waveguide depth, for several modes, as in Figure 2.2. More commonly, the x-axis in a dispersion curve is the wavelength of light, not the waveguide depth. In such a case, the waveguide geometry is fixed. In our case, the reverse is true: the wavelength is fixed, so the waveguide depth, which is variable, occupies the x-axis. The general behaviour of effective indices is summarized as follows:

1. Modal indices increase with the waveguide depth.
2. For the same n_s, deeper waveguides support more modes than shallow guides.
3. For the same d, waveguides with a greater n_s support more modes.

Figure 2.2 shows a TM mode dispersion curve calculated with parameters typical for proton-exchanged waveguides in $LiTaO_3$. To calculate d and n_s of the fabricated waveguides, a root-search method is used to find the values of the two variables which give the minimum error between the calculated effective indices and the measured ones. This technique will be described in some detail in Chapter 6.

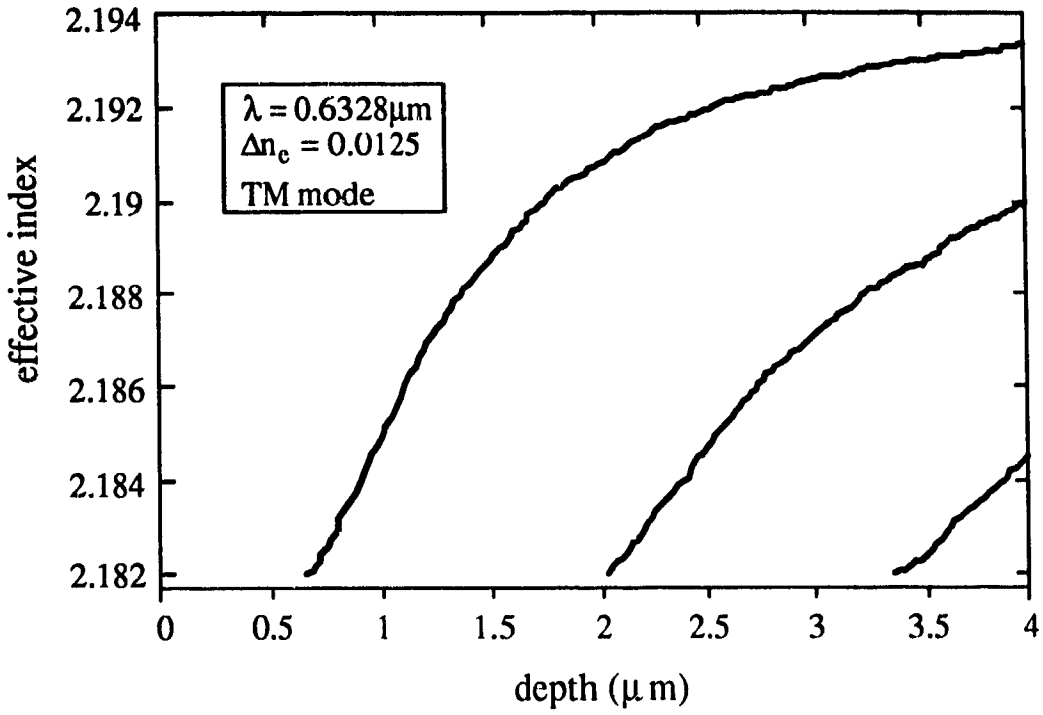

Figure 2.2: Typical step-index dispersion curve for proton-exchanged $LiTaO_3$

Scaling rules [12] may be applied in order to produce universal dispersion curves with normalized parameters. With the proliferation of personal and micro-computers, however, dispersion curves specific to the problem at hand may now be easily and quickly produced, without the need for normalization and universal plots.

One parameter which is of interest is the cut-off: the light frequency or waveguide depth below which a mode no longer propagates. An equation for determining the cut-off in a slab waveguide is easily found by setting the effective index n_{eff} to the substrate index n_b. By doing so, we obtain

$$k\sqrt{n_s^2 - n_b^2}d - tan^{-1}\left[c_2\frac{\sqrt{n_s^2 - n_b^2}}{\sqrt{n_b^2 - n_c^2}}\right] = \left(m + \frac{1}{2}\right)\pi \tag{2.39}$$

$$\text{where } c_2 = \begin{cases} 1 & \text{TE mode} \\ (n_b/n_s)^2 & \text{TM mode} \end{cases} \tag{2.40}$$

2.6 The Ray Optics Approximation

It was possible to analytically solve the wave equation for the slab waveguide because the refractive index was constant in each region. In other specific cases, such as waveguides with a linear or a parabolic index profile, analytic solutions are still possible. However, for an arbitrary index profile $n(x)$, analytic solutions are often not possible. In this section, we examine the ray optics approximation, which will allow us to develop a dispersion relation applicable to waveguides with any index profile [13]. Consider Figure 2.3, which depicts a light ray of a guided mode traversing the waveguide.

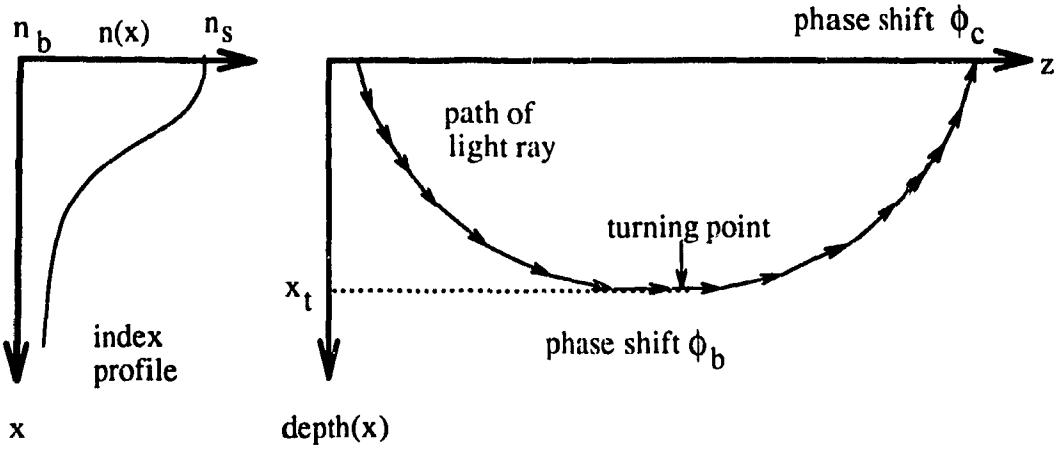

Figure 2.3: The ray optics approximation

As the light ray penetrates deeper into the waveguide, the ray path curves due to refraction because the refractive index decreases with depth. At the turning point, the light approaches grazing incidence and is internally reflected back. It takes a symmetrical path back up to the waveguide's surface, where by total internal reflection it once again begins to descend. If the light strikes the surface at less than the critical angle or if it does not curve enough to reach a turning point, it will radiate out of the guiding layer. Such rays become radiation modes. Guided modes satisfy the transverse resonance condition - the phase delay of one round trip from the surface to the turning point and back again

must be a multiple of 2π. If this condition is not met, the light interferes destructively, attenuates, and does not propagate. The resonance condition is stated as

$$2\int_0^{x_t} \sqrt{k^2 n^2(x) - \beta^2}\, dx + \phi_c + \phi_b = 2m\pi \tag{2.41}$$

where the *integral* is the phase delay of the travelling wave, ϕ_c the phase shift at the cover-waveguide boundary, and ϕ_b the phase shift at the turning point x_t.

The phase shifts ϕ_c and ϕ_b are the phase terms in Fresnel's reflection coefficients. These phase shifts are given by

$$\phi_b = -\frac{\pi}{2} \qquad \text{for both TE and TM mode} \tag{2.42}$$

$$\phi_c = -2tan^{-1}\left\{c_2 \frac{\sqrt{n_{eff}^2 - n_c^2}}{\sqrt{n_s^2 - n_{eff}^2}}\right\} \tag{2.43}$$

where $c_2 = 1$ for TE mode, and $c_2 = \left(\frac{n_s}{n_c}\right)^2$ for TM mode.

Thus, the complete ray optics approximation is stated as

$$\int_0^{x_t} \sqrt{k^2 n^2(x) - \beta^2}\, dx - tan^{-1}\left\{c_2 \frac{\sqrt{n_{eff}^2 - n_c^2}}{\sqrt{n_s^2 - n_{eff}^2}}\right\} = (m + \frac{1}{4})\pi \tag{2.44}$$

Chapter 3

Proton Exchange in $LiTaO_3$

3.1 Introduction

This chapter introduces lithium tantalate as a substrate material and presents a comprehensive review of the state of current knowledge on proton-exchange technology. The material properties of $LiTaO_3$ are described, and the values of some important physical and optical constants are cited. A survey of $LiTaO_3$ waveguide fabrication processes is conducted, and proton-exchange is shown to have numerous advantages over other methods. The techniques of fabrication are described, and the intricate diffusion mechanisms and chemical dynamics of proton-exchange are considered in detail. Proton-exchange with buffered acid melts is also examined.

3.2 Properties of Lithium Tantalate

Lithium tantalate is a dielectric and ferroelectric crystal useful in many diverse integrated optics applications. Its utility stems from the optical phenomena that are possible because of its large linear and non-linear electro-optic coefficients, high acousto-optic figure of merit, and large pyroelectric, piezoelectric, and photoelastic coefficients. Lithium tantalate is closely related to lithium niobate, a more commonly used (and more widely researched) crystal in integrated optics.

In the ferroelectric phase (below the Curie temperature of 610°C), the anisotrophic lithium tantalate crystal consists of planar sheets of oxygen atoms in a distorted hexagonal close-packed configuration (see Figure 3.1). The lithium atoms lie slightly above the plane while the tantalum atoms lie below the plane. The resulting charge separation causes spontaneous polarization, giving rise to the multitude of optical effects present in $LiTaO_3$.

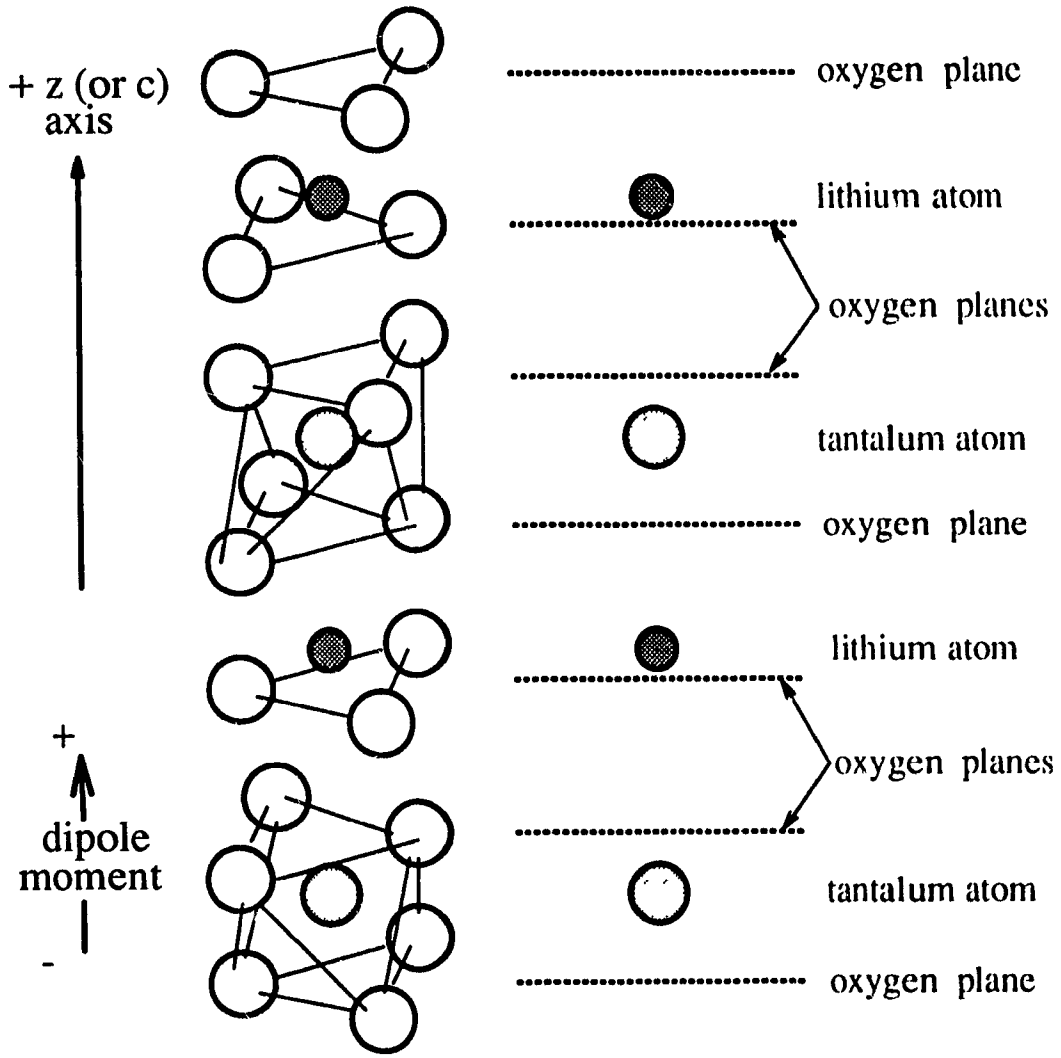

Figure 3.1: Atomic structure of lithium tantalate [11]

Table 3.1 lists the values of some material constants and coefficients for $LiTaO_3$, and Tables 3.2-3.5 cite values for the optical constants and coefficients of $LiTaO_3$ [15].

crystal class	rhombohedral
space group	R3c or C_{3v}^6
point group	3m or C_{3v}
Lattice constants: rhombohedral	a_{Rh} = 5.4710 Å
	α_{Rh} = 56° 10.5'
Lattice constants: hexagonal equivalent	a_H = 5.15428 Å
	c_H = 13.78351 Å
Density	7.45 g/cm^3
Molecular weight	235.88
Melting point	1650°C
Curie point	610°C
Moh Hardness	5.5-6.0
Thermal expansion coefficient (0-110°C)	$\alpha_a = 16.1 \times 10^{-6}$ °C^{-1}
	$\alpha_c = 4.1 \times 10^{-6}$ °C^{-1}
Pyroelectric Coefficient at 27°C	0.019 μC/(cm^2 °C)
Acoustic velocity	$\rho = 6.19 \times 10^5$ cm/s
Acoustic wave propagation loss	Γ = 0.1 dB/(cm GHz^2)
Acoustooptic figure of merit	$M_2 = 1.37 \times 10^{-18} s^3/g$
Electrical resistivity	10^{13} Ω-cm
Transmission window ($I_{trans} > 0.5 I_{incident}$)	0.4-5μm
Propagation loss (at 0.6328μm)	≈ 0.1dB/cm

Table 3.1: Physical properties of $LiTaO_3$

Dielectric permittivity (10^{-9} farads/m)	ϵ_{11}^s	0.377
	ϵ_{33}^s	0.379
	ϵ_{11}^t	0.474
	ϵ_{33}^t	0.384
Nonlinear optical coefficients (10^{-12} m/V at 0.6328 μm)	d_{22}	2.08
	d_{31}	1.28
	d_{33}	19.39

Table 3.2: Dielectric permittivities and nonlinear optical coefficients

	Wavelength (μm)				
Temperature	1.06	0.6328	0.5145	0.4880	0.4579
21°C	5040V	2811V	2197V	1920V	1735V
155°C	4343V	2405V	1805V	1640V	1507V

Table 3.3: Half-wave voltages (E*l)λ/2

wavelength (μm)	ordinary index n_o	extraordinary index n_e
0.15	2.2420	2.2468
0.5	2.2160	2.2205
0.6	2.1834	2.1878
0.6328	**2.1700**	**2.1820**
0.7	2.1652	2.1696
0.8	2.1538	2.1578
0.9	2.1454	2.1493
1.0	2.1391	2.1432
1.2	2.1305	2.1341
1.4	2.1236	2.1273
1.6	2.1174	2.1213
1.8	2.1120	2.1170
2.0	2.1066	2.1115
2.2	2.1009	2.1053
2.4	2.0951	2.0993
2.6	2.0891	2.0936
2.8	2.0825	2.0871
3.0	2.0755	2.0299
3.2	2.0680	2.0727
3.4	2.0601	2.0649
3.6	2.0513	2.0561
3.8	2.0121	2.0473
4.0	2.0335	2.0377

Table 3.4: Refractive Indices

constant strain on crystal (clamped)	r_{13}^s	7.0
	r_{22}^s	0
	r_{33}^s	30.3
	r_{42}^s	20
	$(n_e^3\ r_{33} - n_o^3\ r_{13})^s$	243
constant stress on crystal (unclamped)	r_{13}^t	8.4
	r_{22}^t	-0.2
	r_{33}^t	30.5
	$(n_e^3\ r_{33} - n_o^3\ r_{13})^t$	223

Table 3.5: Linear electro-optic coefficients (10^{-12} m/V at 0.6328 μm)

Crystal Coordinate System

Either a hexagonal or a rhombohedral coordinate system is used to describe the crystalline structure of $LiTaO_3$. The Cartesian x, y, z axes are mapped to the hexagonal axes in the following manner: the z axis coincides with the c axis; the x axis coincides with any of the a_{II} axes (perpendicular to a mirror plane); the y axis, parallel to a mirror plane, is chosen to make the system right handed (see Figure 3.2). Lithium tantalate crystals are commonly sold in the form of plates, designated x-cut, y-cut, and z-cut. Z-cut crystals have the z axis normal to the surface of the wafer, and similarly the x and y axes are perpendicular to the x-cut and y-cut wafer surfaces, respectively. According to the IRE standard, a second letter is attached to the designation which indicates the axis of the longest dimension of the wafer surface. For example, an zy-cut wafer has its surface parallel to the xy plane, and the wafer is longer along y axis than the x axis. If one has a wafer and does not know the direction of the axes, a set of simple tests given by Weiss and Gaylord [14] can be used to determine the crystal orientation.

The crystal is symmetric about three mirror planes, and the c-axis is parallel to these mirror planes and perpendicular to the planar sheets of oxygen. The c-axis is defined as the axis about which the crystal exhibits three-fold rotational symmetry, and is also known as the optical axis. Light propagating parallel to this axis is called *ordinary*, and light propagating perpendicular to the optic axis is *extraordinary*. Because $LiTaO_3$ is a birefringent crystal, it has two indices of refraction: the ordinary index n_o and the extraordinary index n_e, depending on the direction of light propagation. $LiTaO_3$ is a positive uniaxial crystal, which means that $n_e > n_o$.

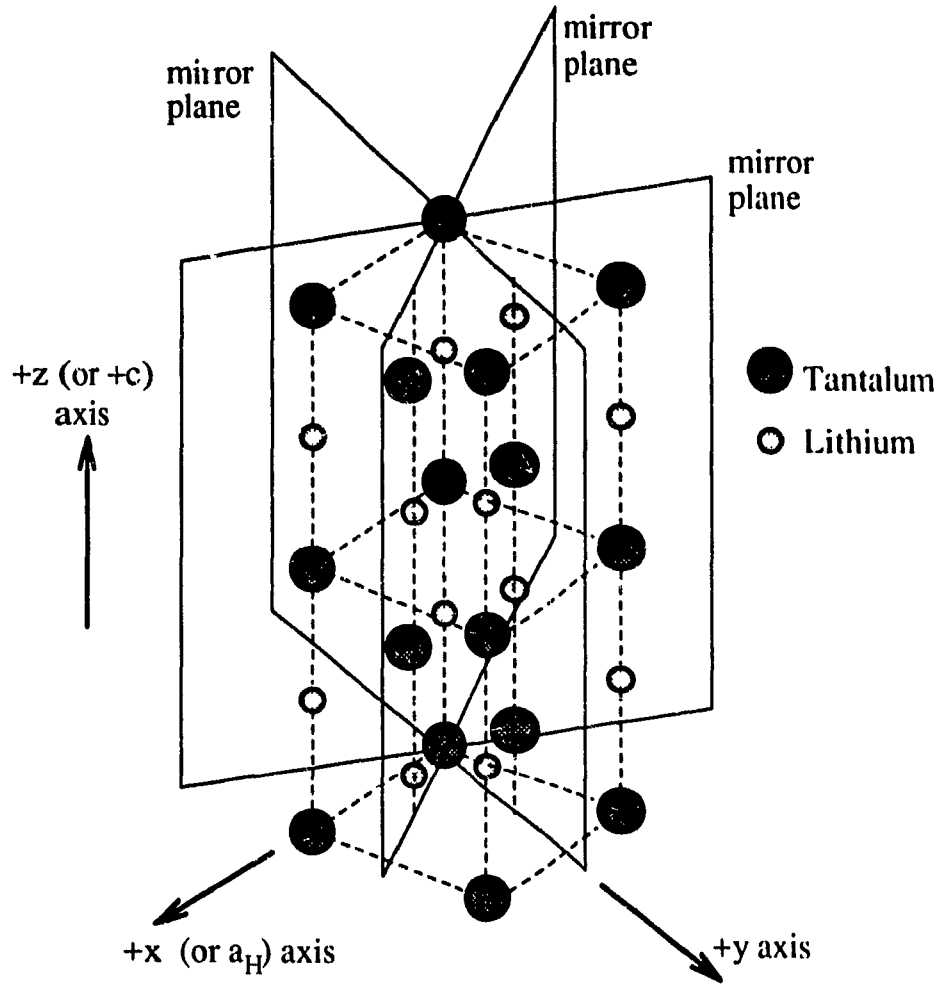

Figure 3.2: Crystal coordinate system

3.3 Survey of Waveguide Fabrication Processes

In general, all waveguide fabrication techniques have the following two steps in common: a mask defining the waveguide pattern is deposited on the substrate, and a dopant is then added to increase the refractive index in the desired regions. This selective increase in the refractive index permits waveguiding. As the field of integrated optics developed in the 1970's, different waveguide fabrication techniques for $LiTaO_3$ were attempted. These include high temperature in-diffusion of metals; out-diffusion of lithium; electro-diffusion;

ion-exchange; and proton-exchange. A brief description of each method follows.

High temperature in-diffusion of metals

High temperature in-diffusion involves the deposition of a metal such as niobium [16, 17], titanium [18, 19], or zinc [20] onto the substrate surface, followed by high temperature (> 1000°C) diffusion of the metal into the crystal. Both the extraordinary and ordinary index increase, so both TE and TM polarizations are supported. The in-diffusion process occurs above the lithium tantalate's Curie temperature of 610°C, so in order to recover the crystal's electro-optical properties, the dipole moment of the crystal must be re-aligned. This process is known as repoling the crystal. This was a relatively involved and complicated task, and as a result, few attempted to fabricate waveguides on $LiTaO_3$ with this method. By contrast, lithium niobate's Curie temperature (1200°C) is above that of the in-diffusion process, so repoling is not necessary. This technique is, therefore, suitable for $LiNbO_3$, and in fact titanium in-diffusion has become a standard method for fabricating devices in $LiNbO_3$.

Out-diffusion of lithium

This is again a high temperature process, in excess of 1000° and above the Curie temperature [21, 22]. At such a high temperature, lithium dioxide (LiO_2) diffuses out of the crystal resulting in a surface waveguiding layer. Lithium out-diffusion is a process that accompanies in-diffusion of metals and is usually perceived as a problem which needs to be suppressed. Once again, because of the need for repoling the crystal, little interest was expressed in this technique.

Electro-diffusion of copper

Diffusion of copper ions [23] in the presence of an electric field made it possible to make waveguides below the Curie temperature. The ardous task of repoling the crystal was avoided, but propagation losses were very high and rendered the waveguide useless. It strongly absorbed visible and near infrared light due to the presence of copper. This technique was not pursued.

Ion-exchange

Ion-exchange is a relatively simple and inexpensive process, which involves immersing the substrate in a molten bath of an appropriate salt. It operates below the Curie temperature, and produced waveguides with low loss and otherwise good characteristics. Initial experiments with silver [24] and thallium [25] seemed quite promising, but after repeated attempts it was found that the results were not consistently reproducible. The authors were at a loss to explain these findings, so the usefulness of ion-exchange was doubtful. Later, it was discovered that H_2O (water) impurities in the melt were the source of the index increase. Proton-exchange, rather than ion-exchange, was responsible for the initial results. Thereafter, extensive research into proton-exchange began.

Proton-exchange

Proton-exchange was first demonstrated for lithium niobate in 1982 [2] and for lithium tantalate in 1983 [3]. Since this time, the technique has gained wide acceptance. Hundreds of articles appear each year reporting on proton-exchanged devices. The discovery of this technique has stimulated a great interest in $LiTaO_3$ devices. The fabrication process is similar to that of ion-exchange: the substrate is simply immersed in an acid melt. Proton-exchange operates below the Curie temperature so repoling is not necessary.

The main advantages of proton-exchange are:

1. low cost and ease of fabrication
2. stability and repeatibility
3. resistance to optical damage (can handle high intensities): suitable for short wavelength applications
4. only one polarization mode supported
5. allows quasi-phase matching which enhances second harmonic generation (SHG)

In recent years, numerous high performance optical devices have been fabricated on $LiTaO_3$ by proton-exchange. These include low-loss optical waveguides [6, 7, 3, 26], Mach-Zehnder interferometers [27, 28, 29], a fiber-optic gyro device [30], a phase modulator [28], directional couplers [28, 26], an acoustic wave transducer [31], a waveguide laser [32], and a second harmonic generator [33].

Summary

Before proton-exchange, high temperature in-diffusion of titanium was the most popular way of making waveguides on $LiTaO_3$. However, there were very few attempts because devices were far easier to fabricate on $LiNbO_3$, whose optical properties are very similar to those of $LiTaO_3$. $LiNbO_3$ does not need to be repoled after in-diffusion. This difference contributed to popularity of $LiNbO_3$ and the relative neglect of $LiTaO_3$ in the last two decades. Thanks to proton-exchange, more and more devices are being fabricated on $LiTaO_3$. These new devices often take advantage of lithium tantalate's high resistance to optical damage, which is two orders of magnitude higher than lithium niobate's. This makes proton-exchange especially suitable because proton-exchange increases the material's resistance to optical damage. Proton-exchange in $LiTaO_3$ is still a young field, and

one can expect to see many more proton-exchanged $LiTaO_3$ devices in the future.

3.4 Proton-exchange: Fabrication Techniques

Proton-exchange is a simple technique: all that is needed is an oven or furnace capable of heating the acid up to 200°C-300°C. Depending on the device's tolerances, even a hot plate could be used. The acid is inexpensive. The surface index, index profile, and waveguide depth are all controllable by post-exchange annealing, or by using buffered acid melts. Index profiles may be tailored to give a specified electromagnetic field distribution.

Hydrogen ions from the acid is the dopant which causes the index increase, and the index profile after exchange is step-like. Both $LiTaO_3$ and $LiNbO_3$ are anisotropic materials, and the ordinary and extraordinary indices are affected differently by the presence of hydrogen. The extraordinary index n_e increases notably, and this increase is termed Δn_e ($\Delta n_e = n_s - n_b$). In $LiNbO_3$ the ordinary index n_o decreases. In $LiTaO_3$, n_o either decreases, or changes so little as to be not detectable. Since the index must increase for waveguiding to occur, proton-exchanged waveguides support only one light polarization. In z-cut substrates only the TM mode propagates; in x- and y-cut substrates only the TE mode propagates.

3.4.1 Different Acids and Substrate Cuts

For proton-exchange to proceed, the hydrogen must be in the form of protons, in a concentrated, dissociated ionic state. In this state, the hydrogen ions (protons) are highly mobile, able to penetrate the substrate. Many suitable protonic sources have been identified:

1. Benzoic acid ($C_6H_5CO_2H$) [2, 31, 35, 36]. It is the most commonly used protonic source. It is non-toxic and does not attack most metals, permitting a wide choice of

mask materials. The operating temperature is 150-250°C. The acid evaporates and introduces particulates into the air.

2. Pyrophosphoric acid ($H_4P_2O_7$) [37, 38, 39, 40, 41, 42, 43, 44]. This acid gives a higher Δn_e, slightly higher diffusion coefficient at the same temperature, and lower propagation losses in $LiNbO_3$ than benzoic acid. Whether the same results hold for $LiTaO_3$ is not clear, and one objective of this work is to find out. The operating temperature may be as high as 300°C. Pyrophosphoric acid will attack aluminum, so metals such as tantalum must be used instead for masking. The acid degrades during exchange.

3. Stearic acid [45, 46], cinnamic acid [17], toluic acid [48], salicylic [49] and palmitic acid [50]; sulfuric [51] and hydrochloric acids [52]; water [53], and hydrate melts [52].

Different acids produce slightly different results - there is no clear correlation between the acid's dissociation constant (a measure of the concentration of available, solvated protons) and the speed of proton-exchange or the resultant index increase Δn_e.

Proton-exchange proceeds at different rates, depending on the cut of the substrate. Long exchange times and high temperatures will cause damage to the crystal surface, because the presence of hydrogen induces high stresses in the crystal lattice. These stresses will eventually cause the surface to be etched and the substrate to crack. Y-cut substrates etch very quickly, so only very shallow waveguides can be made before surface damage renders the waveguide useless. The y-cut orientation is not often used in waveguide fabrication. X- and z-cut substrates are more resistant to surface damage, so they are the preferred orientations. Proton-exchange is faster in x-cut than in z-cut substrates, and the z-cut orientation is the least susceptible to etching and cracking.

Table 3.6 compares the fabrication parameters of different acids on various orientations of $LiNbO_3$ and $LiTaO_3$ substrates.

Acid	Substrate	Loss	D_0 ($\frac{\mu m}{hr}$)	E_a (eV)	Δn_e	Remarks
benzoic	x-cut $LiNbO_3$		1.523×10^9	0.95	0.126	[35]
"	"	1.4dB/cm	0.135×10^9	0.867	0.126	[54]]
"	y-cut		1.233×10^9	0.95	0.126	[35]
"	z-cut		0.868×10^9	0.95	0.126	[35]
"	"	2.4dB/cm	1.81×10^9	0.97	0.126	[34]
pyrophosphoric	"	$\leq$ 1 dB/cm	0.643×10^9	0.856	0.115	highest Δn_e [42]
sulfuric	"		1.42×10^6	0.91	0.12	suitable for clean room
stearic	"	1.5 dB/cm	5×10^6	0.712	0.118	non-toxic
toluic	"	1 dB/cm	7.02×10^7	0.78	0.121	non-toxic
benzoic	z-cut $LiTaO_3$	1.3 dB/cm	3.61×10^{17}	1.82	0.017	[7]
pyrophosphoric	"	0.3 dB/cm	3.91×10^6	0.74	0.01	[8]

Table 3.6: Comparison of different acids: measurment at 0.6328μm

3.4.2 Spin-coating, Surface-coating, and Immersion

Usually the masked substrate is completely immersed in the acid during exchange, but other techniques like spin-coating and surface-coating the acid onto the substrate surface have also been used with success. These two alternate processes require very little acid (~0.1ml) and give the same step-like index profiles and similar Δn_e values for exchanged waveguides. However, some penalties are incurred for using these perhaps simpler techniques [40]. Values for the effective indices of surface-coated waveguides varied depending on the location of the input prism. This variation was probably a consequence of the nonuniform coating of the surface, and hence, nonuniform exchange. Also, a melt

dilution/buffering effect may occur because the acid volume is so small. Lithium diffuses out into the acid, and reduces the proton in-diffusion rate. For both surface- and spin-coated waveguides, the diffusion coefficient was lower than for immersed waveguides [40].

In the case of pyrophosphoric acid, the acid degrades during exchange and forms polyphosphoric acids. This may lower the proton concentration and hence lower the diffusion rate. If either surface-coating or spin-coating must be used, long exchange times and high temperatures should be avoided in order to prevent melt-dilution and acid degradation effects. One must also make sure that the substrate surface remains evenly coated throughout the exchange process in order to ensure uniformity in the waveguide depth. The immersion technique is recommended since it produces more reliable and consistent waveguides for a wide range of exchange temperatures and times. To ensure consistency the acid bath should be replaced each time.

3.5 Proton-Exchange: Chemistry

The following description of proton-exchange is based mainly on research with lithium niobate substrates. $LiNbO_3$ was and still is a much more popular material than $LiTaO_3$. Nonetheless, due to the physical, chemical, and optical similarities between lithum tantalate and lithium niobate, one may cautiously assume that the results hold true for both materials. This may not be strictly true, but we shall take this as our working assumption and explicitly state any exceptions.

When $LiNbO_3$ or $LiTaO_3$ substrates are immersed in an acid, hydrogen ions (protons) from the acid diffuse into the substrate, and lithium atoms from the substrate diffuse out into the acid. The presence of hydrogen into the crystal has a number of effects [55]:

1. Resistance to optical damage (optically induced change in refractive index) increases.

2. n_o decreases (for $LiNbO_3$).

3. n_e increases.

4. Ionic conductivity of crystal increases.

5. Sound propagation characteristics (velocity, attenuation) are altered.

6. Phase matching temperatures are greatly diminished.

7. Optical holograms within a crystal are fixed.

3.5.1 Hydrogen-Lithium Exchange and Hydrogen In-diffusion

Hydrogen is incorporated into the lithium niobate crystal during proton-exchange in two ways. The first is via a one-for-one ion-exchange process: the lithium in $LiNbO_3$ is replaced with hydrogen from the acid. At the crystal surface, Li^+ ions leave their positions within the crystal and dissolve in the acid melt, while the H^+ ions enter the crystal and occupy positions in the crystal lattice. The H^+ ions then diffuse further into the crystal, and Li^+ ions from within the crystal diffuse towards the surface.

The exchange reaction may be represented by the chemical equations [53]

$$Li_2O + H^+ = LiOH + Li^+ \tag{3.1}$$

$$LiOH + H^+ = H\text{-}O\text{-}H + Li^+ \tag{3.2}$$

The concentrations of the lithium and hydrogen ions during the hydrogen-lithium exchange reaction seem to be governed by the ion-exchange diffusion equation [56]:

$$\frac{\partial C_H}{\partial t} = \frac{\partial}{\partial x}\left(\frac{D_H}{1-\alpha C'_H}\frac{\partial C'_H}{\partial x}\right) \tag{3.3}$$

$$= \frac{\alpha D_H}{(1-\alpha C'_H)^2}\left(\frac{\partial C'_H}{\partial x}\right)^2 + \frac{D_H}{1-\alpha C'_H}\left(\frac{\partial^2 C'_H}{\partial x^2}\right) \tag{3.4}$$

where C_H is the proton concentration (μm^{-3}), D_H the diffusivity of the protons ($\mu m^2/hr$), D_{Li} the diffusivity of lithium, and $\alpha = 1 - D_H/D_{Li}$.

The second way in which hydrogen is incorporated into a lithium niobate crystal is by diffusion of OH^- ions. These are created in a reaction between water, which is present in the melt as the acid degrades, and oxygen at the crystal surface. This chemical reaction is represented by [53, 57]

$$H_2O + O^{2-} = 2OH^- \tag{3.5}$$

$$OH^- + O^{2-} = O\text{-}H\text{-}O \tag{3.6}$$

Judging from the results of [53], this reaction occurs at a slower rate than the exchange reaction.

The Exchanged Layer

In the exchanged layer, a portion of the lithium has been replaced by hydrogen, and a small amount of hydrogen has diffused inward. The compound $Li_{1-x}H_xNbO_3$, where x is the fraction of lithium atoms replaced, denotes the composition of the material in the exchanged layer. The value x of course varies with depth, being largest at the surface and decreasing as the depth increases. This compound exists in different distinct phases, depending on the proportion of hydrogen [58]: the α phase for $x \leq 0.12$; the $\alpha + \beta$ phase for $0.12 \leq x \leq 0.56$; the β phase for $0.56 \leq x \leq 0.75$; the mixed β + $HNbO_3$ phase for $x \geq 0.75$. The presence of hydrogen alters the distance between atoms in the unit cell (i.e. lattice constants) and consequently strains the crystal lattice, so different phases have different physical properties. It is suspected that the existence of multiple phases augments the propagation loss, for light would be scattered at phase transition boundaries.

To measure the phase transitions and changes in the crystal lattice constants (lattice strains), x-ray diffraction methods are used. Regardless of the orientation, only the lattice constants in the direction perpendicular to the surface change [35, 49]; they do not occur in any other direction. The opposite effect was found in $LiNbO_3$ powders [58, 59]. For z-cut

Substrate	Acid	Strain	Ref.
x-cut $LiNbO_3$	benzoic	$\Delta a/a \approx 0.8\%$	[35]
y-cut "	"	$\Delta a/a \leq 1.6\%$	[35]
z-cut "	"	$\Delta c/c \leq 0.16\%$	[60]
z-cut "	sulfuric	$\Delta c/c \approx 0.3\%$	[51]
z-cut $LiTaO_3$	benzoic	$\Delta c/c = 0.52\%$	[7]
z-cut "	pyrophosphoric	$\Delta c/c = 0.56\%$	[8]

Table 3.7: Strain

substrates, the strain is denoted by $\Delta c/c$, and for x-cut substrates, by $\Delta a/a$, where c and a are the lattice constants along the z- and x- axis respectively (see Fig. 3.2). The strains are always positive, and its value appears to be independent of fabrication conditions [60]. The intensity of the diffracted x-rays increase linearly with the thickness of the exchanged layer. Table 3.7 presents the strain values in $LiNbO_3$ and $LiTaO_3$ substrates of different orientations.

Ganshin *et al.* [61, 62] have observed distinct phases in proton-exchanged x-cut $LiTaO_3$ waveguides. Initially, the exchanged layer is in only the α phase. The hydrogen concentration at the surface increases due to exchange, and once the threshold is reached the next phase forms at the surface. The α phase moves deeper into the substrate. This process continues as proton-exchange progresses. The concentration profile thus resembles a staircase function, with the highest concentration phase at the surface, descending to the α phase at the exchanged layer-substrate boundary. Three distinct phases have been observed. These results, however, have not been verified by other workers.

3.5.2 Low to Medium Hydrogen Concentration

Infra-red (IR) spectroscopy [35, 44, 46, 49, 51, 55, 63, 64, 65] can determine the amount and nature of oxygen-hydrogen (OH) bonding in the crystal by measuring the amount of infra-red light absorbed. A sharp absorption band at $3500cm^{-1}$, polarized

perpendicular to the z axis, indicates the presence of OH ions. These ions have their transitional momentum perpendicular to the optical c axis and thus vibrate solely in the plane perpendicular to the z axis. This indicates that the protons occupy sites within the oxygen planes (see Fig. 3.1) instead of the lithium sites between the oxygen planes.

3.5.3 High Hydrogen Concentration

For a total exchange (values of x close to 1), the original $LiNbO_3$ crystal changes from a hexagonal structure to the cubic perovskite structure of $HNbO_3$. This phase transformation induces enormous stress; the change in volume and the accompanying strain on the crystal lattice will cause the surface to crack and etch. It is not possible to fully exchange crystalline $LiNbO_3$ into $HNbO_3$ and still maintain a waveguiding layer.

IR spectroscopy measurements detect a second type of OH bonds which produce a broad, unpolarized absorption band centered around $3250cm^{-1}$ [35, 51, 58, 63, 64]. These are hydrogen bonded OH ions (H-OH ions) which are randomly oriented with regard to the c-axis. When the hydrogen concentration is low (i.e. for short exchange times and/or low temperatures and/or weak acid), H-OH ions do not form [46, 58]. Since the highest hydrogen concentration is at the crystal/acid interface, these ions form at the substrate surface. Hydrogen concentration profiling methods have found that for a very thin ($\approx$0.1-0.2μm) surface layer, the hydrogen concentration exceeded the nominal (bulk) lithium concentration of $\approx 1.9\times10^{10}$ atoms/μm^3 [51, 66, 67]. In addition, the lithium was not completely depleted: about 16% of the lithium was still present. This clearly indicates that proton-exchange is not a one-for-one exchange process.

H-OH ions have been observed for x-cut and y-cut substrates, but for z-cut substrates they are present in small proportions [35, 41, 63]. It is believed that H-OH ions are the cause of some of the following problems with proton-exchanged waveguides:

- index instability/fluctuation [68]

- dc extinction effect [69]
- reduced electro-optic coefficient r_{33} (by about 90%) [60, 69]
- reduced nonlinear optical coefficient d_{33} (by about 99%) [70]
- reduced acousto-optic figure of merit [69]

These ions may have high mobility which allows them to migrate throughout the waveguide, even at the room temperature. This would then cause the effective mode indices to fluctuate. H-OH ions also increase ionic conductivity, which would explain the dc extinction effect. H-OH ions are present only at high hydrogen concentrations, so if the concentration were to be lowered, index instabilities and dc extinction should not occur. The reduction in r_{33} and d_{33}, on the other hand, is probably caused by the deformation of the crystal lattice [60]. It is believed that high hydrogen concentrations cause the lattice to deform to the cubic perovskite structure of $HNbO_3$, whereas a low concentration would not deform the lattice. Thus, a low concentration should preserve the pre-exchange r_{33} and d_{33} values. The underlying cause for all these problems seems to be a high hydrogen concentration. The use of buffered melts and of annealing lowers the hydrogen concentration, and indeed, H-OH ions and the problems associated with high concentrations are not found in buffered and/or annealed waveguides. Buffered melts are discussed at the end of this chapter, and annealing is considered in the next chapter.

3.5.4 Shape and Depth of the Exchanged Layer

Nuclear imaging techniques such as Secondary Ion Mass Spectrometry (SIMS) [46, 51, 65], Nuclear Reaction Analysis (NRA) [35, 69, 71], and Elastic Recoils Detection Analysis (ERDA) [66, 72] are used to detect the hydrogen and lithium concentration profiles. The results have varied somewhat from one research group to another, but in general, they are consistent. The hydrogen concentration profile is step-like: it maintains

a constant value from the surface throughout the exchanged layer, and declines rapidly at the exchanged layer-substrate boundary.

Usually, for ion-exchange processes, the concentration profile is graded. The step profile is likely due to the double-alkali effect [73], in which the diffusion coefficients of the ion-exchange diffusion equation (see Equation 3.4) are not constant but are rather functions of the concentration of the counter-diffusing ion - that is, $D_H(C_{Li})$ and $D_{Li}(C_H)$. A simulation of the equation using such functions has been performed [74], with successful results. A simplified model of proton-exchange was used, one which did not take into account hydrogen in-diffusion nor the effect of phases. A complete model simulating all the process known to occur during proton-exchange would be rather difficult to implement. Fortunately, the simplified model has a close enough accuracy to suffice.

The lithium concentration profile was found to be graded. From a minimum at the substrate surface, it rises gradually, until it reaches the bulk concentration at a point past the depth of the hydrogen profile. If the ion-exchange diffusion equation were obeyed, the lithium profile should then be the complement of the hydrogen profile. The fact that the two profiles are not complementary is likely due to hydrogen in-diffusion (see Section 3.5.1), which introduces additional hydrogen ions into the crystal.

Rutherford Back Scattering (RBS) spectrometry can detect the lattice distortion in the crystal. A distortion boundary exists between the exchanged layer and the virgin substrate, so the depth of the exchanged layer may be determined with some precision [35, 51, 75, 76]. The exchanged layer depth matched the depth of the step-like hydrogen concentration profile. As well, the depth has been found to be linearly proportional the area of the IR absorption band at $3500cm^{-1}$ [63, 51]. With proper calibration, it is possible to determine the exchanged layer depth by the amount of IR absorbance.

3.6 Hydrogen Concentration and the Refractive Index

It is generally believed that the change in the crystal's spontaneous polarization arising from the presence of hydrogen and the loss of lithium [58] is responsible for the index change. However, the exact cause and the mechanism behind the change in the dipole moment and how this affects the index is not clear, partly because it is difficult to isolate the many effects arising in the proton-exchange process. As well, it is believed that regular OH ions contribute to the index increase, whereas H-OH ions do not [67]. Hou [77] has provided a simple model of refractive index dependence on hydrogen concentration, and supported it with a numerical calculation which agreed with experimental results.

Nonlinear Dependence on Hydrogen Concentration

As may be expected, the greater the amount of hydrogen in the $LiNbO_3$ crystal, the greater the index increase. However, the degree of index increase does not linearly depend on the hydrogen concentration [78]. When a proton-exchanged waveguide is annealed, the hydrogen diffuses deeper into the waveguide and the concentration of hydrogen decreases (for $LiNbO_3$). Likewise, the refractive index profile extends deeper into the waveguide and the surface index change decreases. However, the total area of the index profile increases. No new hydrogen is introduced into the crystal during annealing, so one would expect the area to remain constant. This increase in area leads one to suspect a nonlinear relationship between hydrogen concentration and refractive index change.

Howerton *et al.* [78] have found an approximate relationship between concentration and index change. For low hydrogen concentrations, the index increases slowly; at medium concentrations, the index increases linearly; for high concentrations, the index increase saturates. Other factors such as the effect of separate phases make it difficult to directly correlate the refractive index profile with the hydrogen concentration profile.

Refractive Index Profile

Effective indices measured by prism coupling make it possible to reconstruct the refractive index profile of the exchanged waveguide. The methods discussed in the previous section all focus on the chemistry and the diffusion kinetics of the proton-exchange. However, knowledge of the index profile - the shape, depth, and the surface index increase - is the most important and pertinent information for the proper design and fabrication of waveguides. The simplest and perhaps most accurate way to obtain this information is by effective index measurements. The experimental portion of this thesis, for example, is almost exclusively comprised of effective index measurements. Other methods of characterization were not readily available for this work.

Effective index measurements indicate that the index profile is step-like in shape, and its depth matches the depth of the exchanged layer as determined by RBS and nuclear techniques [35, 51, 52, 75]. By fabricating a number waveguides under different fabrication conditions, a relationship between the depth and the fabrication parameters was found:

$$d_{pe} = 2\sqrt{D_e(T_{pe}) \times t_{pe}} \tag{3.7}$$

where d_{pe} is the depth of the exchanged layer (μm), t_{pe} the exchange time (hours), T_{pe} the temperature (Kelvin), and $D_e(T_{pe})$ the effective diffusion coefficient (μm^2/hr). Its dependence on temperature is given by

$$D_e(T_{pe}) = D_0 exp(-\frac{E_a}{kT_{pe}}) \tag{3.8}$$

where D_0 is a diffusion constant (μm^2/hr), E_a the activation energy (eV), and k the Boltzmann constant (eV/K). With these relations, one may fabricate a waveguide of a desired depth with precision by properly selecting the exchange time and temperature.

Various workers [43, 79] have proposed different mathematical functions to describe the index profile, but the step function approximation is the simplest and, at the same

time, highly accurate. In general, the optical depth is greater than the exchanged depth - up to about 10% greater [35]. A summary of the diffusion constants and extraordinary index increases for different orientation $LiNbO_3$ and $LiTaO_3$ substrates proton-exchanged in various acids is presented in Table 3.6.

3.7 Buffered Melts

A small amount of lithium in the benzoic acid buffers the melt by reducing the out-diffusion rate of lithium. Since the in-diffusion rate of hydrogen is dependent on the lithium concentration ($D_H[C_{Li}]$), it should be reduced. Proton-exchange thus proceeds at a slower rate. Lithium benzoate ($LiC_6O_3H_6$) is dissolved in benzoic acid melts to increase the lithium concentration up to 5% molar (where %molar = moles of lithium benzoate/moles of benzoic acid). Surface damage on y-cut substrates is significantly reduced, making the fabrication of waveguides on y-cut material feasible. No report of buffering other acids has been available in the literature.

IR measurements show that with buffering, the area of the 3250cm^{-1} absorption band (H-OH ions) relative to the 3500cm^{-1} (OH ions) decreases quite drastically [41, 50, 63, 76]. For 1% buffering [63], H-OH ions are almost non-existent. The exchanged layer is most likely in or close to a single α phase. By reducing the rate of proton-exchange, buffered melts produce waveguides with lower hydrogen concentrations than those produced with pure melts. The experimentally observed benefits of a lower hydrogen concentration include:

1. Effective indices no longer fluctuate [52].

2. Lattice strain is reduced [60, 80].

3. r_{33} increases. A completely restored value of r_{33} has been observed for 1% molar lithium [52], though others [60, 80] report a still somewhat reduced r_{33} for buffering

up to 4% molar.

4. Propagation losses are lower [52].

A linear increase in the lithium concentration leads to an exponential decrease in the effective diffusion coefficient [52, 60, 63], and a linear decrease in Δn_e [50, 60, 63]. There is evidence which suggests that above 3% buffering, Δn_e drops drastically [81]. The index profile remains a step. Oddly enough, for $LiTaO_3$, Δn_e *increased* with buffering up to 2% molar, but decreased thereafter [67].

Chapter 4

Annealing

4.1 Introduction

This chapter describes the effects of annealing on proton-exchanged $LiNbO_3$ and $LiTaO_3$ waveguides.

4.2 Post-exchange Annealing

Post-exchange annealing reduces or eliminates most of the problems exhibited by proton-exchanged waveguides. Annealing achieves many of the same goals as the use of buffered melts, but with an additional advantage. With buffered melts the refractive index profile is a fixed step function, but with annealing, the profile can be tailored to a desired shape. During annealing, the depth increases, the surface index initially increases but later decreases, and the profile gets progressively smoother.

In the annealing process, a proton-exchanged waveguide is subjected to heat treatment for several minutes to several hours at 300°C - 400°C. This is performed in an open oven with a flowing gas. Researchers have used dry O_2, wet O_2 (i.e. with water vapour), dry or wet N_2, and some do not even maintain a controlled gas flow (i.e. oven is open to the atmosphere). Differences in the annealing environment seem to have no effect [82]. The important annealing conditions are the anneal temperature and time.

4.3 Annealing in $LiNbO_3$

Physical and Chemical Changes

Annealing causes the hydrogen in the exchanged layer to diffuse further into the waveguide. Thus, the index profile smears out [38, 42, 79, 83], and the surface hydrogen concentration decreases [78]. Meanwhile, lithium diffuses back up to the surface [51, 65]. The advantageous effects of lowering the hydrogen concentration and reducing the number of phases within the exchanged layer are numerous:

1. Index instabilities are eliminated [26].
2. Lattice strains are relieved [46, 51].
3. r_{33} is fully restored [81].
4. dc extinction effect is eliminated [81].
5. Propagation losses are lowered [63, 83].

Single α phase waveguides have been observed after annealing [61, 78]. Howerton [78] has proposed the following criteria for obtaining stable, single-phase waveguides: the waveguide depth after annealing d_a should be greater than the depth after proton-exchange d_{pe} by a factor of at least seven and a half ($d_a > 7.5\, d_{pe}$).

Infra-red studies [63] reveal a decrease in H-OH ion content with annealing, while the OH ion content remained the same. This suggests the removal of H-OH ions from the substrate, which may occur via the reversible reactions with water (see equations 3.5 and 3.6). In the same way that H-OH ions are introduced during proton-exchange, they are removed during annealing. The area of the 3250cm^{-1} absorption band decreases while the 3500cm^{-1} absorption band area stays constant. The validity of this dehydration reaction is further supported by TEM studies [84].

Work with the hydrogen isotope deuterium has shown that just-exchanged waveguides will react with water vapour at the room temperature [41, 85], while buffered or annealed waveguides do not. The surface layer of H-OH ions seems to act as a catalyst for the reaction with water vapour at the room temperature. At annealing temperatures, water vapour is taken up regardless of whether H-OH ions are present [63]. When buffered guides are annealed [40, 63], little change occured to the IR absorption bands. Since buffered guides contain very few H-OH ions, this finding is consistent with previous results.

For modelling the diffusion of hydrogen ions during annealing, the simple finite-source diffusion model has been used [65, 72, 86] with some success. The equation governing this process is Ficke's law [56]

$$\frac{\partial C_H}{\partial t} = \frac{\partial}{\partial z}\left(D_H \frac{\partial C_H}{\partial z}\right) \tag{4.1}$$

where C_H is the hydrogen concentration profile, and D_H the diffusion coefficient ($\mu m^2/hr$). Good agreement has been found between SIMS-measured hydrogen profiles and analytic solutions of Ficke's law [65]. Agreement has also been obtained between measured index profiles and simulated profiles using Ficke's law with a concentration-dependent D_H [87]. In both cases, the existence of distinct $H_x Li_{1-x} NbO_3$ phases was not accounted for, since the complications of different diffusion coefficients in each phase and the diffusion kinetics across phase boundaries leads to a very difficult problem to model.

Changes in the Refractive Index Profile

With annealing, the waveguide depth d increases, the surface index n_s decreases, and the index profile becomes increasingly graded. As one might expect, the higher the temperature or the longer the anneal time, the greater the change. The increase in the

waveguide depth has been found to obey the empirical equation [38, 39, 43]

$$\Delta d = d - d_{pe} = b t_a^c \tag{4.2}$$

where d is the current waveguide depth, d_{pe} the depth after proton-exchange, t_a the anneal time, and b, c are fitting parameters. Waveguides with a small d_{pe} will experience a smaller Δd than waveguides with a large d_{pe}. The surface index decrease was found to obey a similar relation [38, 39, 43]:

$$\Delta n_s = n_s - n_b = e t_a^f \tag{4.3}$$

where n_s is the surface index, n_b the substrate index, and e, f are fitting parameters. Here f is negative, so that Δn_s decreases for greater t_a. Waveguides with a small d_{pe} will experience a greater decline in n_s than those with a large d_{pe} [43].

4.4 Annealing in $LiTaO_3$

In $LiTaO_3$, the effects of annealing are similar to those for $LiNbO_3$: the hydrogen concentration decreases [88]; strain is relieved [80]; and the 3250cm^{-1} IR absorption band (H-OH ions) disappears. There is, however, one important difference - instead of decreasing, the surface index initially increases [8, 88]. The surface index then peaks, and eventually declines with prolonged annealing. In $LiNbO_3$, H-OH ions, which do not affect the crystal's refractive index, are removed from the crystal during annealing by means of a surface reaction. In $LiTaO_3$, however, they remain in the crystal and are converted into OH ions, which do affect the refractive index. The area of the 3500cm^{-1} absorption band increases, while the area of the 3250cm^{-1} band decreases [80]. The OH ion concentration increases and thus n_s increases. Even though the total hydrogen concentration decreases upon annealing, the change in bonding leads to an increase in n_s. Why H-OH ions in $LiTaO_3$ behave differently during annealing than those in $LiNbO_3$ is not known.

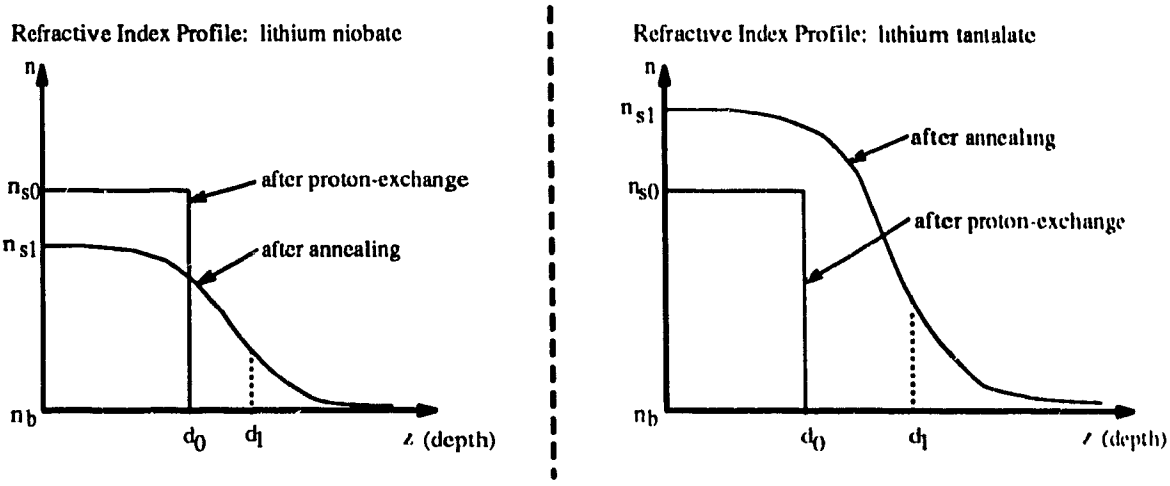

Figure 4.1: Comparing index profiles of annealed $LiNbO_3$ and $LiTaO_3$ waveguide

Anomalous Surface Index Increase

Little is known about this increase except that it occurs. Characterization of the change in n_s upon annealing is in fact one of the goals of this thesis. It is postulated that the change in n_s results from the interaction of the following concurrent processes:

1. Diffusion of OH ions, which lowers n_s by reducing the concentration.
2. Conversion of H-OH ions to OH ions, which raises n_s by increasing the concentration.
3. Diffusion of H-OH ions.
4. A nonlinear relationship between exchanged hydrogen concentration and index change.

In the hope of gaining a deeper understanding of how these processes interact to produce the change in n_s, a mathematical model was developed and a numerical simulation was attempted (see Appendix A). This effort represents only preliminary work on the problem, but the results are encouraging.

Chapter 5

Fabrication and Measurement Methods

5.1 Introduction

This chapter describes fabrication techniques for annealed proton-exchanged planar $LiTaO_3$ waveguides, and the methods used to measure the waveguides' effective indices and propagation losses.

5.2 Preparing the $LiTaO_3$ Substrate

The z-cut $LiTaO_3$ substrates used in this work were made to order from Deltronic Crystals Inc. [89]. The substrate orientation is shown in Figure 5.1. The wafers have the following properties:

- electro-optic grade $LiTaO_3$
- 20mm× 25mm× 2mm (x, y, z)
- $-z$ face polished to 20/10 scratch dig finish, 2 λ flat
- other surfaces unpolished

Each wafer was cut into four or five pieces measuring approximately 4mm × 25mm

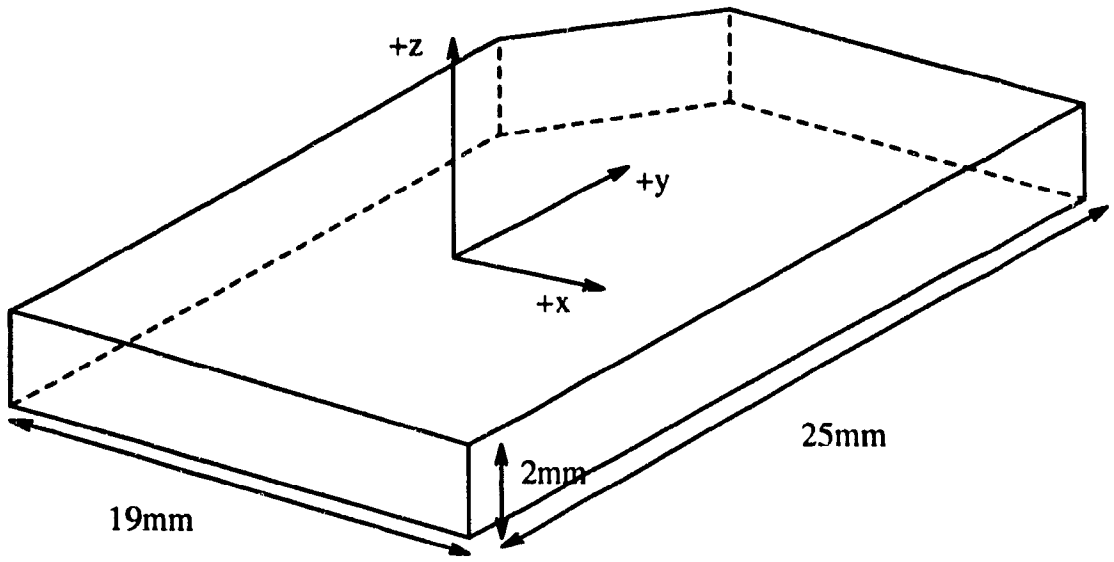

Figure 5.1: Lithium tantalate ($LiTaO_3$) wafer

× 2mm (x, y, z) in order to increase the number of usable substrates. This was done on a crystal cutter in the laboratory of Dr. I. Shih, (McConnell Engineering, room *MC*738) following the procedure described below:

1. Coat a 25cm^2 piece of hard plastic (or equivalent) with candle wax.
2. Place the $LiTaO_3$ wafer flat on the wax before it dries.
3. Coat the wafer with a second layer of wax. The function of the wax is to keep the wafer stationary and fixed on the plastic base while it is being cut and to prevent damage to the wafer surfaces.
4. Clamp the plastic base/wafer to the cutting stage, and slowly advance the stage through the cutting blade. Advancing the crystal too quickly will cause the crystal to crack. Maintain a constant water flow to cool the cutting blade.
5. Translate the cutting stage and repeat until the entire wafer has been cut.
6. Remove the substrates from the wax.

A waxy film now covers the substrate surface and this must be removed. The surface must be free of any films, spots, residues, and impurities. A close examination of the light reflecting off the surface should reveal any such impurities - an immaculately clean surface will reflect light perfectly without distortion. The water break method [1] may be used to assess surface cleaniness. To remove the waxy film and thoroughly clean the surface, the following procedure is used:

1. Immerse the substrates in boiling de-ionized water for about 1 minute.
2. Dip a cotton swab (Q-tip) in a soap solution (de-ionized water and Sparkleen, a non-abrasive detergent) and gently stroke the substrate surface to remove the film. Rinse with de-ionized water.
3. Immerse the substrates in boiling acetone for about 30 seconds.
4. Clean the surfaces again with a cotton swab. Rinse.
5. Dry the substrate with a N_2 gas gun. Inspect the surface. Repeat the above procedure until the surface is immaculately clean. This may require 2 - 3 repetitions.

The substrates must now be subjected to a heat treatment (annealing) in order to relieve the mechanical strains induced in the crystal during the polishing and cutting stages. Substrates are placed in a ceramic crucible and then positioned in the center of the horizontal Lindberg furnace. The furnace is heated to 450°C for approximately 6 hours. A flow of dry nitrogen at 0.5L/min through the furnace is maintained. After this treatment, the substrates are ready for proton-exchange.

5.3 Proton-Exchange

Immediately before proton-exchange, the substrate should be re-cleaned to ensure that no dust or other particles have contaminated the surface. A simple cleaning procedure

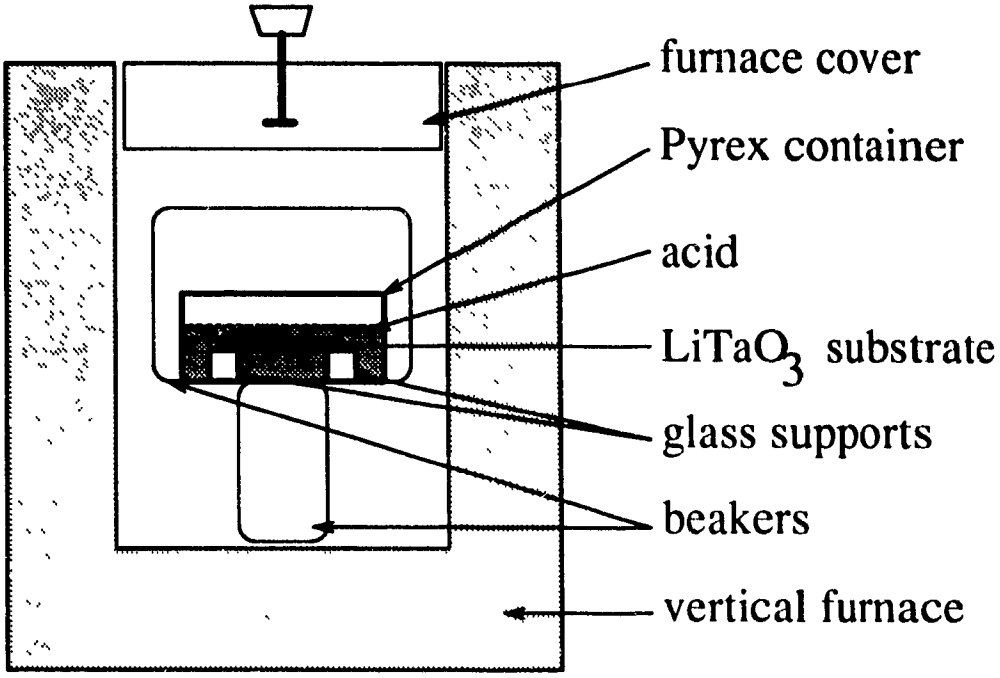

Figure 5.2: Proton-exchange: experimental set-up

will suffice: use the cotton swab and soap solution to gently clean the substrate surface. Rinse with de-ionized water, acetone, and de-ionized water once again. Dry with the N_2 gas gun and inspect the surface. It should be clean - if not, repeat the procedure.

The experimental set-up for proton-exchange is shown in Figure 5.2. Every container which comes into contact with either the substrate or the acid should be thoroughly cleaned beforehand with a cotton swab, de-ionized water, and acetone to prevent contamination. Make sure that the substrate is resting on the glass supports in the container with polished -*c* face down. A white deposit forms and accumulates on all upward-facing surfaces as proton-exchange progresses, due to the decomposition and polymerization of pyrophosphoric acid [41]. Proton-exchange activity may be reduced if this deposit were to form on the substrate surface. The wafer and the acid are put inside the vertical Lindberg furnace in separate containers and heated to the exchange temperature. Once the temperature has stabilized, the acid is poured into the wafer container through a funnel. Proton-exchange commences at this moment and stops when the container is taken out of the oven and

the acid poured out of the container. The substrate is then allowed to cool, and then the surface is once again cleaned so that it is ready for effective index measurements.

For proton-exchange with buffered melts, lithium phosphate (Li_3PO_4) is added to pyrophosphoric acid ($H_4P_2O_7$). The amount of dilution is defined as

$$\%dilution = 3\frac{\text{moles of } Li_3PO_4}{\text{moles of } H_4P_2O_7} \times 100\% \tag{5.1}$$

The factor of 3 is necessary because there are three lithium atoms per mole of lithium phosphate. The atomic weight of pyrophosphoric acid is (4×1)+(2×31)+(7×16) = 178 grams/mole, and the atomic weight of lithium phosphate is (3×7)+(31)+(4×16) = 116 grams/mole. Thus, if 30g of acid is used, then for 1% dilution 0.065g of lithium phosphate is added, for 2% dilution 0.130g of lithium phosphate is added, etc.

5.4 Annealing

Immediately before annealing, the substrate should be cleaned following the simple cleaning procedure described in proton-exchange section above. The horizontal Lindberg furnace is first heated to the anneal temperature. Dry nitrogen gas is pumped through the oven at a rate of 0.5L/min. The substrate is put in a hollow cylindrical ceramic crucible (to allow gas flow) and moved from the edge of the oven (at close to room temperature) to the center of the oven (at the anneal temperature) over a span of 2 minutes. This is done to prevent thermal shock. During these two minutes the substrate warms up to the anneal temperature, so this ramping time is not included in the anneal time. When the anneal period is over, the substrate is removed from the oven and left to cool to room temperature. This cooling period is also not included in the anneal time. The annealing experimental set-up is shown in Figure 5.3.

5.5 Effective Index Measurements - Prism Coupling

A waveguide's effective indices can be found with the prism coupling method [90].

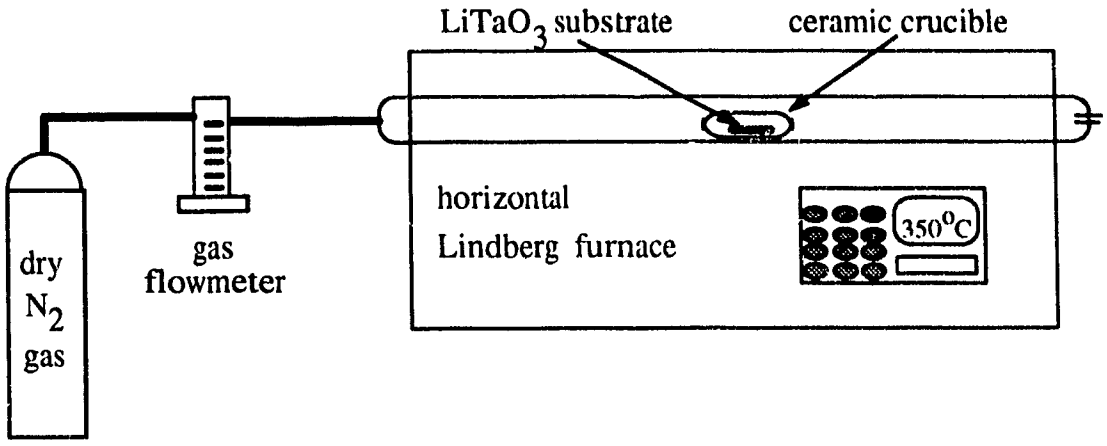

Figure 5.3: Annealing: experimental set-up

A high index prism is held in contact with the substrate surface to couple light into the waveguide. Specially designed clamps (see Figure 5.4) are used to hold the substrate and the prism together. The screws on the clamps are tightened until a whitish spot at the prism base (indicating good contact between the two surfaces) is observed. The screws should not be too tight - the pressure stresses both the prism and the substrate and may cause either or both to crack. For good coupling, the surfaces of both the prism base and the substrate must be free of any dust particles or contaminants. The simple cleaning procedure described in the proton-exchange fabrication section should be used to clean both surfaces before they are mounted on the holders. The following is a simple mathematical model for prism coupling. More detailed and complex models which take other factors into account are available, but a simple model suffices for this work.

A high-index prism of index n_p and base angle α_p is held in close proximity to the waveguide but is separated from it by a very small air gap (see Figure 5.5). The surface roughness of both the prism and the substrates prevents a perfect contact between the two surfaces. Light incident upon the prism's base at an angle θ greater than the critical angle will be total-internally reflected, so a standing wave field distribution will occur within the prism. In the air gap and waveguide, an evanescent field (exponentially decaying away from the prism) persists. The propagation constant β of the light along the waveguide

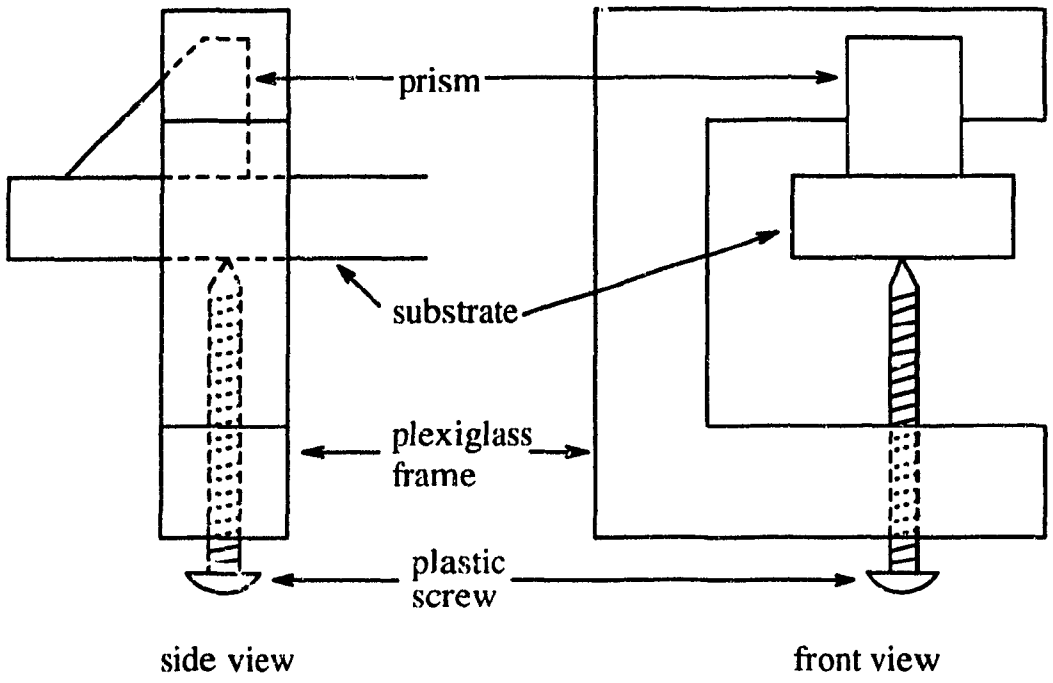

Figure 5.4: The prism/substrate clamp

plane (the z direction) is given by

$$\beta = kn_p sin\theta \tag{5.2}$$

where k is the wave number and $k = 2\pi/\lambda$. If this β is equal to the propagation constant of a guided mode, then by phase matching, the light will no longer reflected but will rather couple into the waveguide. The propagation constant of a guided mode is given by

$$\beta_m = kn_{eff}(m) \tag{5.3}$$

where n_{eff} is the effective index, m denotes the mode order (m = 0,1,2,...), and n_{eff}(m) = $n_s \sin\theta_m$ for a slab waveguide. The phase matching condition is found by simply equating the two previous equations:

$$n_p sin\theta = n_{eff} \tag{5.4}$$

Note, of course, that light may be coupled out of the waveguide in the same fashion. The angle θ can easily be related to the incident angle θ_i by Snell's law and trigonometry,

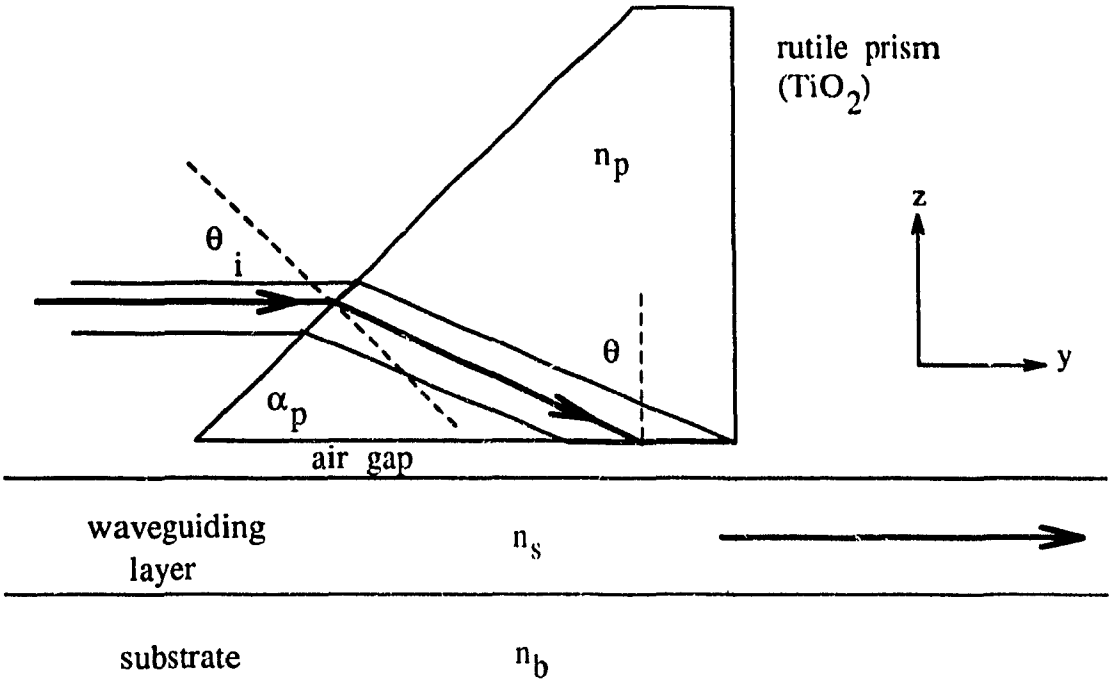

Figure 5.5: Prism coupling geometry

and in the process, the following formula which relates the effective index to measured parameters can be arrived at:

$$n_{eff} = n_p sin\left\{\alpha_p + sin^{-1}\left(\frac{sin\theta_i}{n_p}\right)\right\} \tag{5.5}$$

Each mode has a different effective index value and hence a different incident angle θ_i. In the measurement set-up (see Figure 5.6), the prism and waveguide were placed on a rotating stage. First the prism face is set perpendicular to the incident light ($\theta_i = 0$) so that the light was reflected back unto itself, and the angle on the rotating stage was recorded. This is the reference angle. The stage is then rotated until a guided mode is excited, which is evidenced by the sudden appearance of m-line(s) on the output screen. M-lines are vertical lines with a bright spot at the center. In-plane scattering during propagation causes these lines to form. Good, sharp m-lines usually appear and fade (full width half maximum - FWHM) in the span of three minutes of arc. M-lines which are weak or are not sharp ususally indicate poor contact between the waveguide surface and

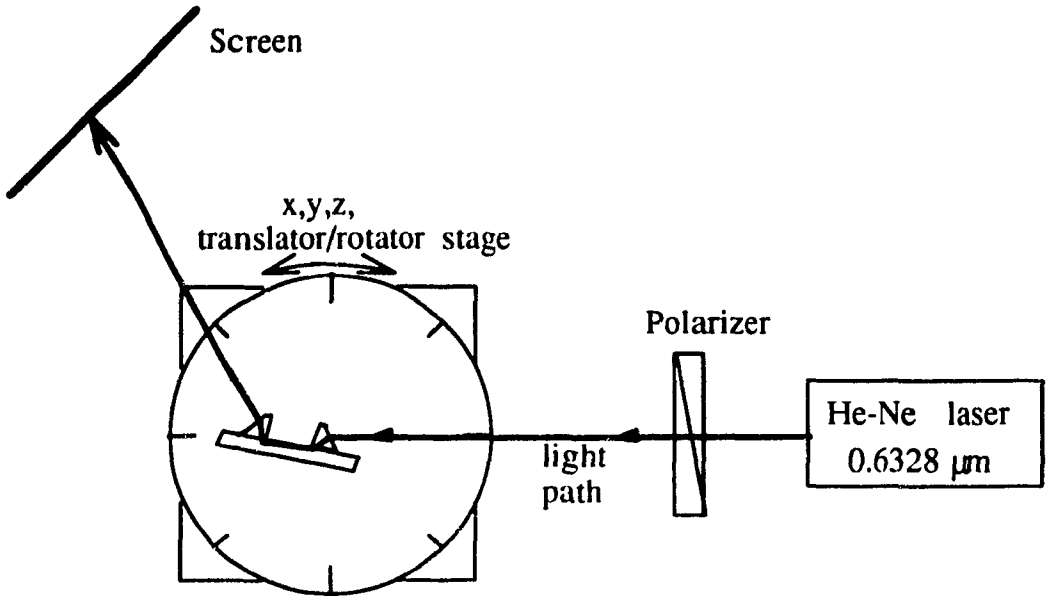

Figure 5.6: Prism coupling: measurement set-up

the prism, or ineffective coupling. In such these cases it is prudent to clean the surfaces and recouple.

The angle which gives the maximum m-line intensity is recorded. The difference between this angle and the reference angle is θ_i. Care must be taken *not* to rotate the stage back if one missed the maximum m-line intensity. The stage should be rotated in one direction only, in order to avoid gear lag. The angle is incremented until all the guided modes have appeared and the angles recorded. Then the stage is rotated backwards, and the angles are once again measured, including the reference angle. Recording the angles in both directions should average out any biases in the rotating stage. A minimum of four measurements for each mode was made, and the average was then used to find the effective index, using Equation 5.5. A helium-neon laser ($\lambda = 0.6328\mu$m) was used for all measurements.

Calibration and Measurement Error

Since all the effective index measurements are made with the rotational stage, which is a mechanical device and subject to deterioration, it is important that the stage be calibrated to ensure accurate results. This can be done by measuring a refractive index which is already known to a high degree of accuracy and precision. By calculating the angle that one should obtain in order to arrive at the known index, and comparing this with the measured angle, the rotational stage can be calibrated. For this purpose the extraordinary index of bulk $LiTaO_3$ (n_b=2.1820) and the index of the rutile prism (2.5837) were used as standards. The indices of these materials are constant and are deemed to be trustworthy. The prism index was measured with the Brewster angle reflection method and the minimum deviation angle method [91]. The $LiTaO_3$ substrate index was measured with the Brewster angle method, and was also inferred from effective index measurements. Over 500 effective indices were measured for proton-exchanged and annealed waveguides, and effective index values span the range of $n_b < n_{eff} < n_s$, where n_s has a maximum of about 2.21. Because of the large number of measurements made, the lowest effective indices will be at or just above n_b. By correlating the measured angles with the expected angles in the four measurement methods outlined above, a correction factor for the rotational stage was arrived at (see Table 5.1).

index measured	method	standard value	calculated angle for standard value	measured angle	correction
n_b	Brewster Angle	2.1820	65.38°	65.55°	-0.17°
n_b	effective indices	2.1820	33.7°	33.9°	-0.20°
n_p	Brewster Angle	2.5837	68.84°	69.15°	-0.31°
n_p	Min. angle of deviation	2.5837	81.56°	81.68°	-0.12°

Table 5.1: Calibrating the rotational stage: average correction = -0.20 °

The rotational stage has an estimated uncertainty of about one minute of arc, or ±0.01667°, when measuring the apex angle and the angle θ_i. The prism index is estimated

variable	value	uncertainty
n_{eff}	-	± 0.0005
n_p	2.5837	± 0.0002
θ_i	-	$\pm 0.01667°$
α_p (prism 'C')	45.253°	$\pm 0.01667°$
α_p (prism 'B')	45.056°	$\pm 0.01667°$
λ	$0.6328\mu m$	-

Table 5.2: Measurement: angles, indices, and their uncertainties

to have an uncertainty of ± 0.0002. The total error in the calculated effective index can be found by summing the percentage error of n_p, α_p, and θ_i. This works out to approximately 0.025% of n_{eff}, or ± 0.0005. Table 5.2 summarizes these values and their uncertainties.

5.6 Loss Measurements

Different loss mechanisms contribute to the total propagation loss of a planar optical waveguide. These include [11]

1. Absorption loss of the substrate.
2. Scattering loss by boundaries and/or material defects (i.e. light is coupled from guided modes to radiation modes and lost from the waveguide).
3. Mode conversion loss (or intermodal scattering: light is coupled from one guided mode to another, usually by scattering).

As the light propagates, its intensity and power decreases exponentially with distance:

$$P_o = P_i e^{-\alpha L} \tag{5.6}$$

where P_o is the output power, P_i the input power, L the propagation length, and α the loss coefficient. By rearranging the equation above, the formula for α is found to be

$$\alpha = \frac{10log(\frac{P_o}{P_i})}{L} \qquad (dB/cm) \tag{5.7}$$

Loss measurement methods include the cut-back method [92], the two-prism sliding method [93], the three-prism method [94], and the scattering detection method [95]. For this work the two-prism sliding method was used. The input coupling prism is clamped to the substrate and does not move throughout the measurement procedure, thus maintaining constant input coupling efficiency. A drop or two of index matching fluid (glycerine, n=1.5) is added to the output coupling prism's base. This allows the prism to slide smoothly across the substrate surface, and increases both the coupling efficiency and consistency. The output prism is moved to different positions along the substrate, varying the distance l between the input and output prisms. At each point, the output prism must be clamped to the substrate, the settings on the translating/rotating stage adjusted to give the maximum output light intensity for the excited mode.

The same measurement set-up used for effective index measurements is used here also (see Fig. 5.6), with the addition of a video camera focused on the modal lines that reflect off the screen. An oscilloscope is connected to the camera output to display the output light intensity. The distance L and peak voltage V is recorded. Note that the output *power* from the camera is proportional to the light intensity (after calibration), and the oscilloscope displays only the *voltage*. Thus the oscilloscope reading V should be squared ($P = VI = V^2/R$) in order to reflect the light intensity. Ten or more such measurements should be made. The coupling efficiency will not be the same at each point (no matter how careful one is), so a large number of measurements should be made in order to average out fluctuations. A least-squares fit is then applied to the $\log(V^2)$ vs. L graph, and the slope of the line of best fit is the value of the loss coefficient α.

Chapter 6

Data Analysis Methods

6.1 Introduction

This chapter explains the methods used to reconstruct an index profile given a set of measured modal indices. The step function, Fermi function, and generalized Gaussian function are introduced as possible models for the refractive index profile. The numerical techniques and algorithms used for analyzing proton-exchanged waveguide data are developed. The Inverse WKB (IWKB) method, used for annealed waveguide data, is implemented and tested.

6.2 Refractive Index Profile Models

Using a mathematical function to model the refractive index profile gives us a basis of comparison between different waveguides. We can quantitatively compare the function parameters found for different index profiles, and hence determine how the fabrication conditions affect the profile. The following three functions have been found to approximate a wide variety of index profiles quite well: the step, the Fermi, and the generalized Gaussian functions. The index profile is expressed in the form

$$n(z) = n_b + \Delta n_s f(z) \tag{6.1}$$

where n_b is the substrate index (for $LiTaO_3$, $n_b = 2.182$ at $\lambda = 0.6328\mu m$), n_s is the index at the waveguide surface, $\Delta n_s = n_s - n_b$, and the profile shape $f(z)$ is given by

$$f(z) = \begin{cases} 1 \ (\ 0 < z < \mathrm{d}) \\ 0 \ (\ z \geq d) & \text{step function} \\ [1 - exp^{-\frac{d}{a}} + exp^{\frac{z-d}{a}}]^{-1} & \text{Fermi function} \\ exp^{-[\frac{z}{d}]^a} & \text{generalized Gaussian function} \end{cases} \tag{6.2}$$

$$\text{at } z = d, f(z) = \begin{cases} 0 & \text{step function} \\ [2 - exp^{-\frac{d}{a}}]^{-1} & \text{Fermi function} \\ 1/e & \text{generalized Gaussian function} \end{cases} \tag{6.3}$$

where d is the waveguide depth, and a controls the degree of curvature of the profile. For the Fermi approximation, a small a ($a < 0.2$) gives a sharp, step-like shape while a large a gives a smooth, gently sloping shape. For the generalized Gaussian, the reverse is true: a large a ($a > 10$) gives a step-like shape while a small a gives a smooth curve. Figure 6.1 shows the shape of each function with different a values.

The step-approximation is the simplest model, having only two parameters (Δn_s and d) while the Fermi and the generalized Gaussian both have three parameters each (Δn_s, d, and a). After proton-exchange, the index profile is known to resemble a step function, so all three functions can adequately model it. After annealing, the profile becomes graded and smooth, so the step function model is no longer adequate.

There are two different approaches for relating effective indices to the index profile. One approach finds the optimum index profile parameters by minimizing the error between measured effective index values and values calculated with the dispersion relation. This is called the forward approach and proton-exchanged waveguides were analysed in this way. There is also an inverse approach, in which the profile is recovered using a recursive formula derived by inverting the WKB dispersion relation. This method was used for annealed waveguides.

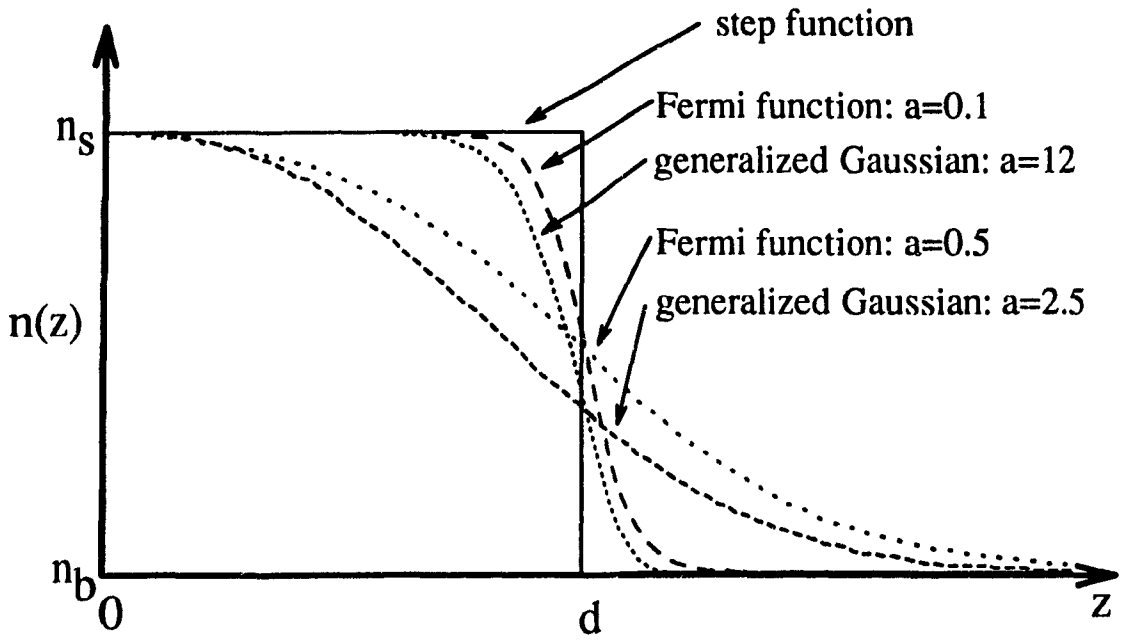

Figure 6.1: The step, Fermi, and generalized Gaussian profiles

6.3 Proton-Exchange Waveguides: The Forward Approach

In Chapter 2, it was shown that the dispersion relation is used to calculate effective indices when the index profile is known. The situation is now reversed: the effective indices are known but the index profile is not. To recover the parameters of the index profile, we simply assume values for the parameters and calculate the effective indices. The parameters are adjusted until the error between the calculated indices and measured indices (i.e. $|\, n_{eff}[\text{calc}] - n_{eff}[\text{meas}]|$) is at a minimum. The step function approximation was used because only two parameters, Δn_e (note that for proton-exchange, $\Delta n_e = \Delta n_s$) and d_{pe}, need to be found. From linear algebra, we know that the number of unknowns must be equal to or less than the number of independent equations for a unique solution. In this case, the parameters are unknown and the effective indices represent equations. Thus, if a three parameter model is used, the measured waveguides should support at least three modes or more. In fact, most of the waveguides support two modes, due to

fabrication constraints. Therefore, using a three parameter model requires that one of the parameters (the shape parameter a) be assumed.

Table 6.1 is a numerical example showing how the analysis is performed. For each waveguide, we assume a value for Δn_e, and use a root search technique (the secant method [96]) to find the depth d which gives the minimum error between measured and calculated effective indices. This procedure is repeated for a range of Δn_e values. It was then assumed that waveguides fabricated at one temperature all have the same Δn_e. This may not be entirely valid due to some annealing effects (see Section 7.4.2), but annealing effects are likely to be small. With a group Δn_e value, one can observe whether the dependence of Δn_e on the exchange temperature exists. Its value is found by summing the errors of all the waveguides exchanged at the same temperature (see the "sum error" column in Table 6.1), for each Δn_e value. The Δn_e with the lowest sum error is taken as the group Δn_e value (in Table 6.1, it is $\Delta n_e = 0.014$). The depth associated with this Δn_e is taken as the waveguide depth (in Table 6.1, $d = 2.40$ for waveguide 1, $d = 1.15$ for waveguide 2, $d = 2.85$ for waveguide 3). For three parameter models, this entire process is repeated for several values of a, and the value of a associated with the lowest sum error determines the group Δn_e value.

Δn_e	waveguide 1		waveguide 2		waveguide 3		**sum error** $\times 10^{-4}$
	d μm	error δ $\times 10^{-4}$	d μm	error δ $\times 10^{-4}$	d μm	error δ $\times 10^{-4}$	
0.010	2.60	3.0	1.35	2.0	3.1	2.5	7.5
0.011	2.55	2.6	1.30	1.7	3.0	2.2	6.5
0.012	2.50	2.1	1.25	1.3	2.95	1.9	5.3
0.013	2.45	1.8	1.20	1.0	2.9	1.7	4.5
0.014	2.40	1.8	1.15	1.2	2.85	1.4	**4.4**
0.015	2.35	2.2	1.10	1.5	2.8	1.2	4.9
0.016	2.30	2.5	1.05	2.2	2.7	1.2	5.9

Table 6.1: Finding the **group Δn_e value** for step-index waveguides. $\delta = | n_{eff}(\text{calc}) - n_{eff}(\text{meas}) |$.

6.4 Annealed Waveguides: The Inverse WKB (IWKB) Method

The IWKB method [98, 99] reconstructs index profiles by providing a recursive formula, obtained by inverting the WKB dispersion relation, which can progressively plot out the index profile. The derivation of this recursive relation begins with the WKB dispersion relation (see Section 2.6):

$$2\int_0^{z_t}\sqrt{k^2n^2(z)-\beta^2}dz+\phi_c+\phi_b=2m\pi \tag{6.4}$$

where the *integral* is the phase delay of the travelling wave, ϕ_c the phase shift at the air-waveguide boundary, and ϕ_b the phase shift at the turning point z_t in the substrate (see Figure 6.2). For TM waves, these phase shifts are given by

$$\phi_c = -2tan^{-1}\frac{n_s^2\sqrt{n_{eff}^2-n_c^2}}{n_c^2\sqrt{n_s^2-n_{eff}^2}} \tag{6.5}$$

$$\phi_b = -\frac{\pi}{2} \qquad \text{see Section 2.6} \tag{6.6}$$

where n_s is the surface index of waveguide, n_c the refractive index of air, and n_{eff} the effective index ($n_{eff}=\beta/k$).

Only integer values of m (i.e. modes m = 0,1,2,...) represent physical, guided modes. Hence, the propagation constant β and the effective index n_{eff} are both discrete functions of the mode order m, i.e. $\beta(m)$ and $n_{eff}(m)$. The turning point z_t is also a function of mode order since a different turning point corresponds to a different effective index. Given the refractive index profile $n(z)$, the WKB dispersion relation can be used to calculate the discrete effective indices.

The key to the IWKB method lies in the fact that at the turning point, the effective index is equal to the refractive index. From Figure 6.2 we see that at the turning point z_t, θ=0 so $n(z)=n_{eff}$, i.e. $n[z_t(m)]=n_{eff}(m)$. If the effective index is made to be a

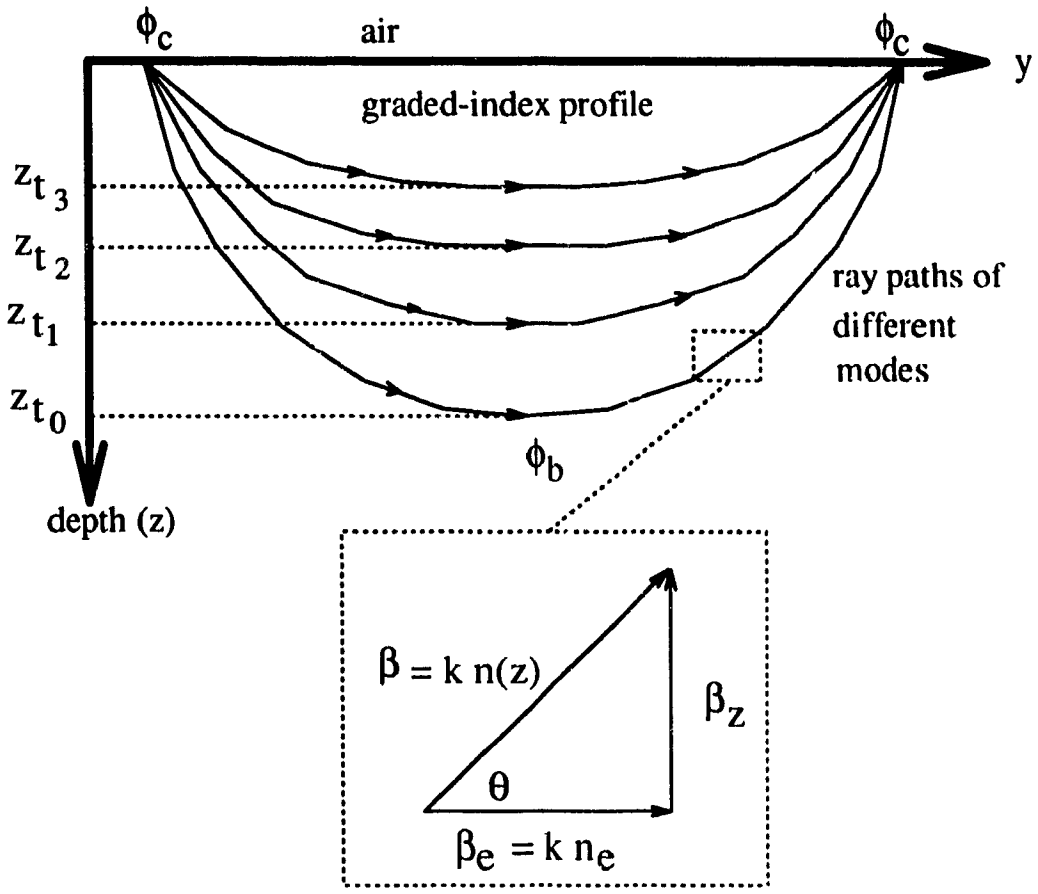

Figure 6.2: Light propagation in a graded-index waveguide

continuous function of m instead of a discrete function, then the turning points z_t also become a continuous function of m. By inverting the WKB equation, the function $z_t(m)$ may be obtained. The continuous function $n_{eff}(m)$ may be interpolated from the discrete measured effective indices. Since the effective index is equal to the refractive index at turning points, the index profile $n(z)$ can be found. Though non-integer values of m have no physical significance, they can be used to recover the index profile.

The WKB dispersion relation may be inverted by replacing the integral with a summation:

$$\alpha_z = \int_0^{z_t} \sqrt{k^2 n^2(z) - \beta^2}\, dz$$

$$= k\sum_{j=1}^{i}\left\{\sqrt{n^2(z_{j-\frac{1}{2}}) - n_{eff}^2(m_i)} \times (z_j - z_{j-1})\right\}$$

$$= k\left[(z_1 - z_0)\sqrt{n^2(z_{\frac{1}{2}}) - n_{eff}^2(m_i)} + (z_2 - z_1)\sqrt{n^2(z_{1\frac{1}{2}}) - n_{eff}^2(m_i)} + \ldots\right] \quad (6.7)$$

where $z_j - z_{j-1}$ approximates the increment dz, $n(z_{j-\frac{1}{2}})$ is the average value of $n(z)$ over the interval $z_j - z_{j-1}$, and i an integer denoting the i^{th} interval in the interpolated effective index function $n_{eff}(m_i)$. The greater the number of intervals Δ (see Figure 6.3), the better the resolution of the recovered profile. Note that $z_i = z_i(m_i)$, so $n[z_i(m_i)] = n[z_i] = n_{eff}(m_i)$. Referring to Figure 6.3, we define

$$N(m_j) = n(z_{j-\frac{1}{2}}) = [n_{eff}(m_{j-1}) + n_{eff}(m_j)]/2 \quad (6.8)$$

so that the summation may be rewritten as

$$\alpha_i = k\left[(z_1 - z_0)\sqrt{N^2(m_1) - n_{eff}^2(m_i)} + (z_2 - z_1)\sqrt{N^2(m_2) - n_{eff}^2(m_i)} + \ldots + (z_i - z_{i-1})\sqrt{N^2(m_i) - n_{eff}^2(m_i)}\right] \quad (6.9)$$

$$= k\left[z_i\sqrt{N^2(m_i) - n_{eff}^2(m_i)} + \sum_{j=1}^{i-1} z_j\left(\sqrt{N^2(m_j) - n_{eff}^2(m_i)} - \sqrt{N^2(m_{j+1}) - n_{eff}^2(m_i)}\right)\right]$$

By rearranging this equation to isolate z_i, we arrive at a recursive equation which allows us to solve for z_i in terms of the previous z_j's:

$$z_i = \frac{\alpha_i - k\sum_{j=1}^{i-1} z_j\left(\sqrt{N^2(m_j) - n_{eff}^2(m_i)} - \sqrt{N^2(m_{j+1}) - n_{eff}^2(m_i)}\right)}{k\sqrt{N^2(m_i) - n_{eff}^2(m_i)}} \quad \text{(for } i \geq 2\text{)} \quad (6.10)$$

$$z_1 = \frac{\alpha_1}{k\sqrt{n^2(m_1) - n_{eff}^2(m_1)}} \quad (6.11)$$

and $$\alpha_i = \int_0^{z_i} \sqrt{k^2n^2(z) - \beta^2}\, dz = m_i\pi + \phi_c(m_i) + \frac{\pi}{4} \quad (6.12)$$

The recovered profile is the set of points $[z_i, n_{eff}(m_i)]$. With equation 6.10, we can progressively calculate z_i. The only unknown left is the surface index n_s used to calculate

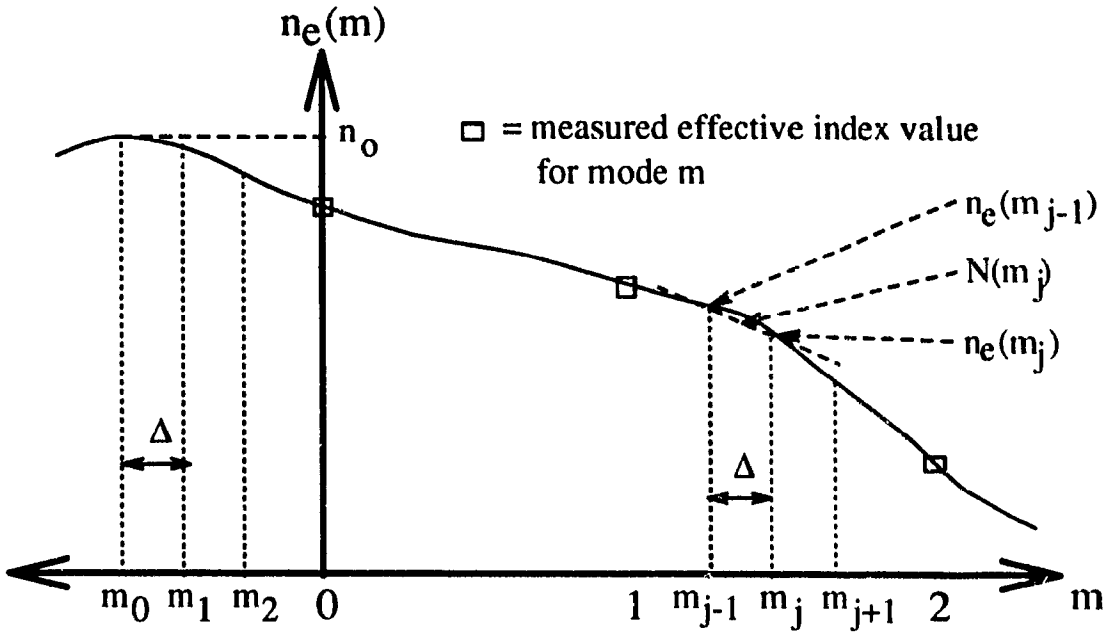

Figure 6.3: The effective index function

the phase shift ϕ_c. This can be obtained by setting $i = 0$, or equivalently $z_t = 0$. We have then $n_{eff}(m_0) = n_s$ since

$$n_{eff}(m_0) = n[z_t(m_0)] = n(0) = n_s$$

Substituting this into equation 6.5, we find $\phi_n = \pi$. Turning to equation 6.4, we see that the integral is equal to zero since $z_t = 0$. The values of ϕ_c and ϕ_b are $-\pi$ and $-\pi/2$, respectively. Solving for m_0, we find $m_0 = -0.75$. Therefore $n_s = n_{eff}(-0.75)$, and this value may be extrapolated from the effective index function (see Figure 6.3).

One limiting condition on the applicability of this method is that the refractive index profile must be monotonically decreasing (i.e. decreasing from n_s to n_b without maxima or minima). One can see that we must have $n(m_j) > n_{eff}(m_j)$ for equation 6.10 to work, and from Figure 6.3 we see this corresponds to a monotonically decreasing index profile. The effective index function must then be monotonically decreasing also. For annealed proton-exchanged waveguides in $LiTaO_3$, the index profile is always monotonically

decreasing so this condition does not pose any problems. However, the IWKB method cannot reconstruct index profiles that are buried, for example.

The Effective Index Function

The effective index function $n_{eff}(m_i)$ is generated from a small number of data points. Inside the range of the data points ($0 < m < m_{max}$), the function is interpolated and the accuracy is usually good. Outside this range, ($-0.75 < m < 0$ and $m > m_{max}$), the effective index function must be extrapolated. The surface index (at $m_0 = -0.75$) and the substrate index (at $m = \infty$) are extrapolated since they lie outside the range of data points. It was found that a polynomial curve fit was the most versatile interpolation/extrapolation scheme. Most other schemes (linear, cubic spline, etc.) do not extrapolate well. The polynomial

$$p(z) = a_n z^n + a_{n-1} z^{n-1} + \ldots + a_1 z + a_0 \tag{6.13}$$

is used to fit the effective indices of a waveguide which supports $n - 1$ modes. Thus a straight line (i.e. order 1) fits a two moded waveguide, and a fourth-order polynomial (i.e. z^4) fits a five moded waveguide. Each guided mode $[m, n_{eff}(m)]$ yields a data point in the form of $[z, p(z)]$ for the curve fitting. Solving for the polynomial's coefficients can be done using matrix techniques (since each guided mode is the solution to an independent WKB dipersion equation) or by using a linear regression algorithm [96].

Evaluating the IWKB Method

This method was tested on a variety of data to evaluate its accuracy and to identify its strength and its flaws. Firstly, the accuracy of the method was tested by calculating mode indices from the WKB dispersion relation, and then applying the inverse method to recover the index profile. Waveguides supporting two to five modes with the step and

the Gaussian index profiles were used to generate the indices. Their index profiles are typical for annealed proton-exchanged $LiTaO_3$ waveguides. Judging from Figures 6.4 and 6.5, the method does not recover the original profile well for two moded waveguides, but is increasing accurate for three or more moded waveguides. This holds true for both the step and the graded Gaussian profiles. Three modes are thus the minimum required for an accurate profile, and the more the better. Since most proton-exchange waveguides were two-moded, the IWKB method could not recover their profiles. Graded profiles are reconstructed more accurately than step profiles. This is to be expected since the WKB dispersion relation assumes a graded-index profile in its derivation. Annealed guides typically support three to ten modes and have graded profiles, so one can expect accurate results from the IWKB method.

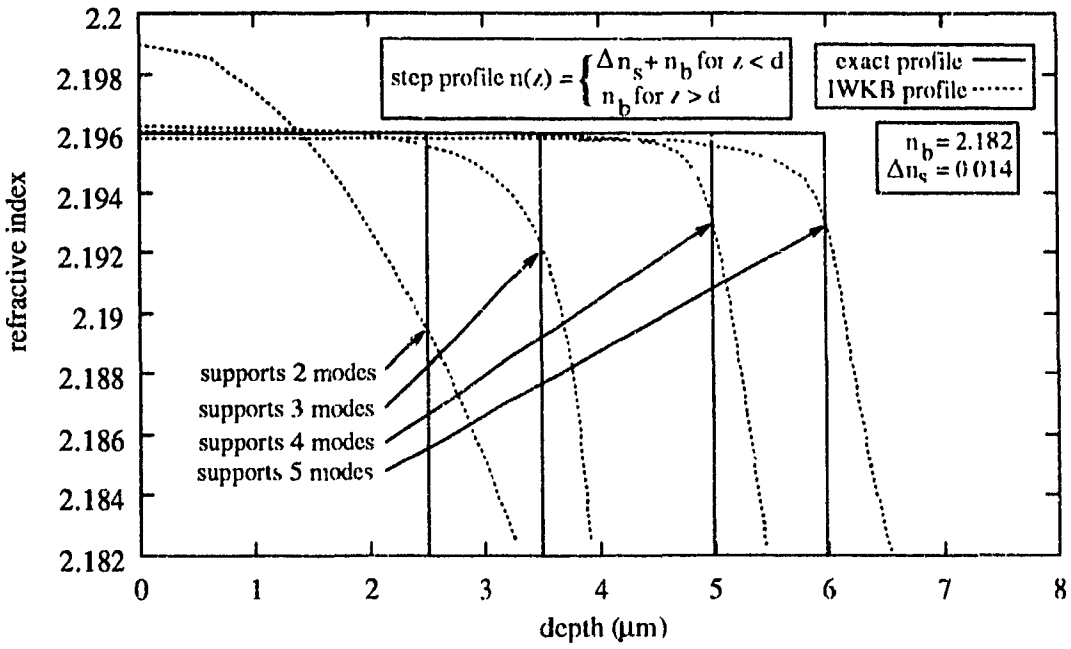

Figure 6.4: Reconstructing step profiles

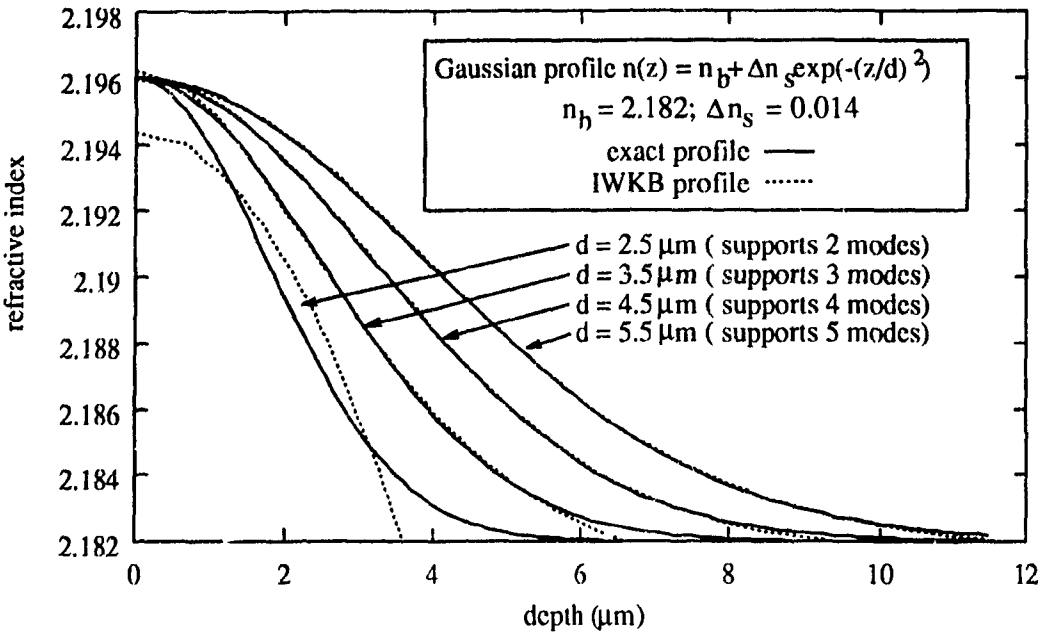

Figure 6.5: Reconstructing graded profiles

Secondly, sensitivity of the method to the measurement error was tested. The exact data was generated with the WKB dispersion relation assuming a generalized Gaussian profile, with various degrees of curvature a. Alternating errors of +0.0005, -0.0005, +0.0005, ... or -0.0005, +0.0005, ... (± 0.0005 = measurement error) were then added to the exact mode indices. These alternating errors created the most distortion in the data, and was deemed the worst case scenario. Clearly, if all the errors were of one sign then the reconstructed profile would merely be shifted up or down.

Upon initial testing, the method was found to be highly sensitive to errors. The recovered index profiles were severely distorted and did not even remotely match the original profiles. The following problems were encountered:

1. The reconstructed profile was not smooth or was physically implausible.

2. The surface index n_s was grossly overestimated.

3. The method does not work because the effective index function is not monotonically decreasing (usually with a maximum between $m = 0$ and $m = -0.75$).

4. The reconstructed profile did not tend to the substrate index n_b

Fortunately, it was found that these problems could mostly be alleviated by using a lower-than-maximum order polynomial for the effective index function [98]. Fitting a third-order polynomial to seven modes, for example, produced an excellent reconstructed profile. The justification for doing this is that the measurement error causes fluctuations in the data, and such fluctuations are incorporated into a maximum-order effective index function. A lower-order polynomial does not necessarily pass through all the data points, so the effect of the error fluctuations is diminished. In fact, the lower order fit may even correct for the measurement error. An effective index function generated from calculated mode index data is smooth. The low order $n_{eff}(m)$ is smoother and more closely resembles a $n_{eff}(m)$ generated from calculated mode indices than a high order one. Usually, a polynomial of order two to four produces the best (i.e. physically plausible, most likely, and smooth) profiles. This is true even if the measured modes number over ten.

Comparing the recovered profiles to the original profiles (see Figures 6.6 and 6.7), one sees that the IWKB method performs well in spite of the errors. The recovered and exact depths match consistently and with very good precision. The shape matches that of the exact profile, though not perfectly. The recovered profile diverges from the exact profile particularly at the tail. The surface index n_s does not match quite as well, with the largest difference between the exact and IWKB value being 0.001. Though one might wish the accuracy to be better, it is adequate for the purposes of this work. In general, the match is good, and the reconstructed profile are reliable and representative of the actual index profile

The lower order fit works well for most cases, some instances of problems 2, 3, and 4 remained. The underlying cause for these problems is that the effective index

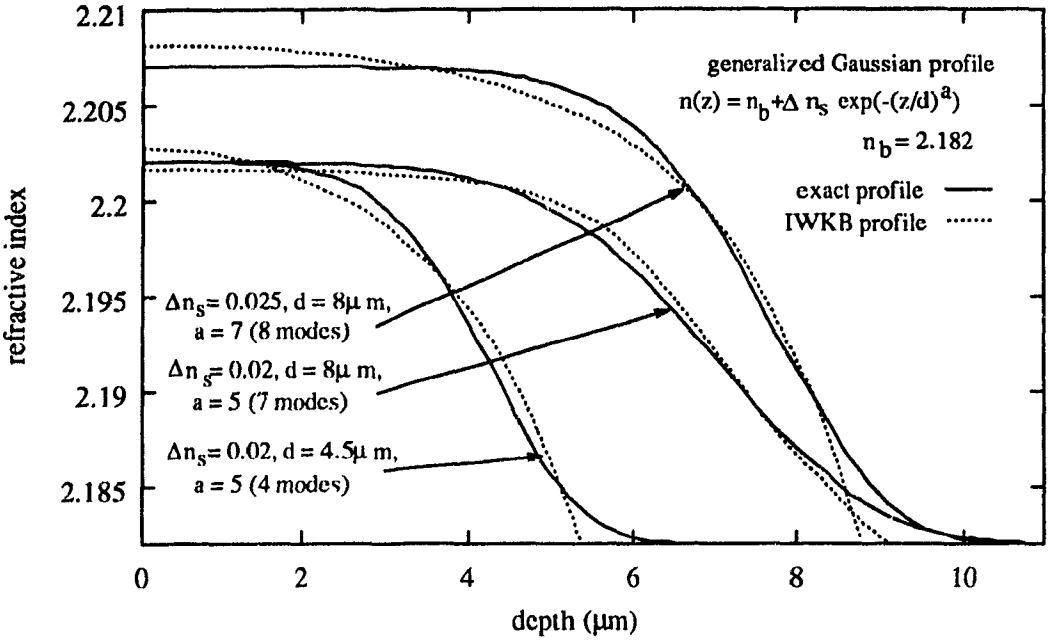

Figure 6.6: Sensitivity to measurement errors

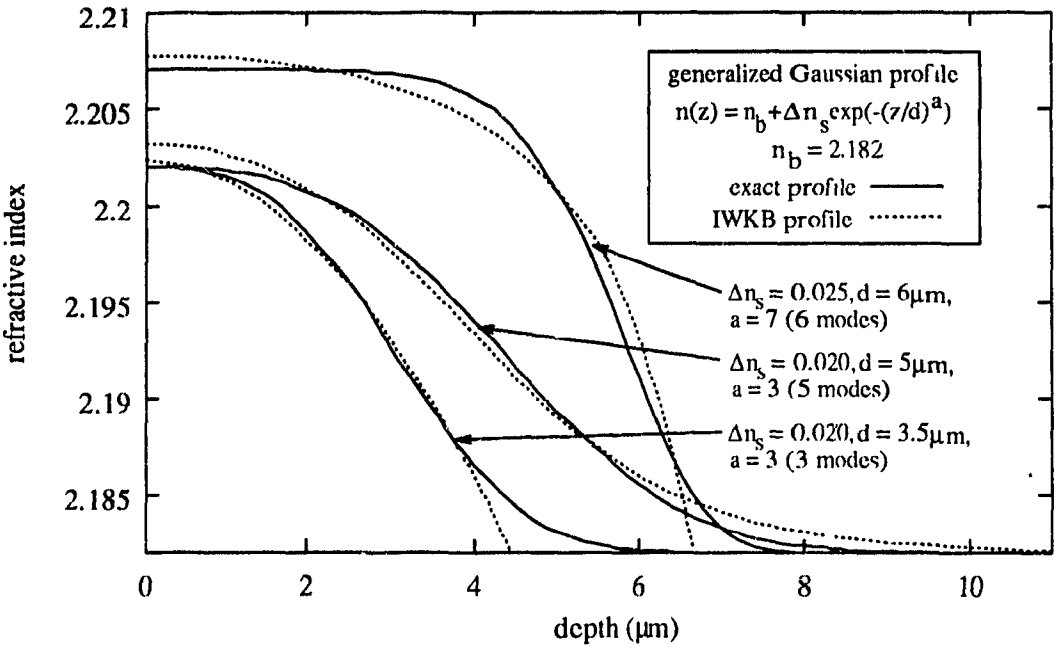

Figure 6.7: Sensitivity to measurement errors

function simply does not extrapolate well. It is possible to force the effective index function to extrapolate more reasonably by introducing an extraneous mode index data point, thus transforming the formerly extrapolated region into an interpolated region. Inside an interpolated region, behaviour of the effective index function is controllable. For problems 2 and 3, the extraneous point can be the surface index at $m = -0.75$. Its value should be one which will result in a monotonically decreasing effective index function and which will produce a reasonable index profile. For problem 4, the extraneous data point should be introduced at $m > m_{max}$. Its value should be at or slightly above the substrate index. The interpolated function will be forced to diminish to a value close to n_b. With these additional corrections, just about any set of data can be made to yield a reasonable refractive index profile.

Summary

The IWKB method numerically generates a refractive index profile given a set of measured effective indices. For annealed waveguides with graded profiles, the reconstructed profiles are expected to be accurate even taking into account the measurement error in the data.

The IWKB method is not an exact method because a continuous effective index function $n_{eff}(m)$ must be generated from discrete data. Depending on which interpolation/extrapolation algorithm is used, a different refractive index profile will be reconstructed. Choosing the appropriate scheme is somewhat arbitrary: any scheme which gives a reasonable and likely profile is acceptable. Thus, index profiles obtained by the IWKB method cannot be regarded as "the true profile". Nonetheless, under most conditions, the method produces fairly accurate, reliable, and trustworthy results, with the advantage that no index profile function $n(z)$ is assumed.

Chapter 7

Results & Discussion

7.1 Introduction

The main objective of this research is to obtain accurate and extensive waveguide characterization data, which will be useful in the fabrication of pyrophosphoric acid exchanged $LiTaO_3$ devices. This chapter is the heart of the thesis: it contains the data and the analysis of proton-exchanged, buffered proton-exchanged, and annealed waveguides in z-cut $LiTaO_3$. The proton-exchange parameters Δn_e, d_{pe}, D_e, D_0, E_a, and propagation losses were found for a range of fabrication conditions and presented in both tabular and graphical format. This data is compared against other results in the literature. New insights into the proton-exchange process on $LiTaO_3$ are discussed. The annealing parameters $\Delta d(t_a)$, $\Delta n_s(t_a)$, and propagation losses were also found for a range of fabrication conditions and again presented in both tabular and graphical format. The observed behaviour of the refractive index profile is explained, and new insights into the effects of annealing are discussed. Finally, a waveguide design procedure, based on the characterization data, is presented. The selection of fabrication conditions for certain sample designs is illustrated.

7.2 Proton-exchanged Waveguides

The aim of this portion of the research is to obtain accurate characterization data for $LiTaO_3$ waveguides proton-exchanged in pyrophosphoric acid. This data could then provide the answers to the following questions:

1. Whether pyrophosphoric acid produces waveguides with better properties than benzoic acid.

2. Whether a Fermi or a generalized Gaussian index profile model is more accurate than the conventional step-index approximation

7.2.1 Step-index, Fermi, generalized Gaussian models

Four substrates were proton-exchanged at each of the four different fabrication temperatures (230°C, 240°C, 260°C, 280°C). Their modal indices were measured and analyzed (following the methods described in Chapter 6) to determine the waveguide depth d_{pe} and the extraordinary index increase Δn_e of each waveguide. Figure 7.1 plots the theoretical dispersion curve of a step-index profile waveguide with the measured modal indices for 240°C. Plots for the other exchange temperatures are very similar. Excellent agreement was obtained between the theoretical and experimental data.

Other researchers have used the more complicated polynomial [12], truncated [43], and modified Fermi [10] functions to more accurately describe the refractive index profile of waveguides proton-exchanged in pyrophosphoric acid. Our data was analyzed using the modified Fermi and the generalized Gaussian models in addition to the step-index model. Table 7.1 shows the error between the calculated and the measured mode index values for each model. The sum error, i.e. the sum of $|\, n_{eff}(\text{calc}) - n_{eff}(\text{meas})|$ for all 30 modes from a total of 16 waveguides, is an indication of the accuracy of each model. The Fermi and generalized Gaussian models do indeed have lower sum errors, but the improvement

is only marginal, and within the range of experimental error. The theoretical mode index values are calculated with an exact dispersion relation for the step model. For the Fermi and generalized Gaussian model, however, the calculation is approximate because the ray-optics approximation is used. Since these models yield only a slight increase in accuracy, but require an additional fitting parameter a and an approximate calculation method, the step-index model is used in the following analysis.

Temp.	all errors are in $\times 10^{-4}$ 230°C	240°C	260°C	280°C	Sum Error $\Sigma \mid n_{eff}(\text{meas}) - n_{eff}(\text{calc})\mid$
Step-index	5.7	4.7	6.5	17.1	**34.0**
Fermi	5.1	4.3	6.5	15	**30.9**
Gen. Gaussian	5.0	4.5	6.1	14.8	**30.7**

Table 7.1: Accuracy of the step-index, Fermi, and generalized Gaussian models

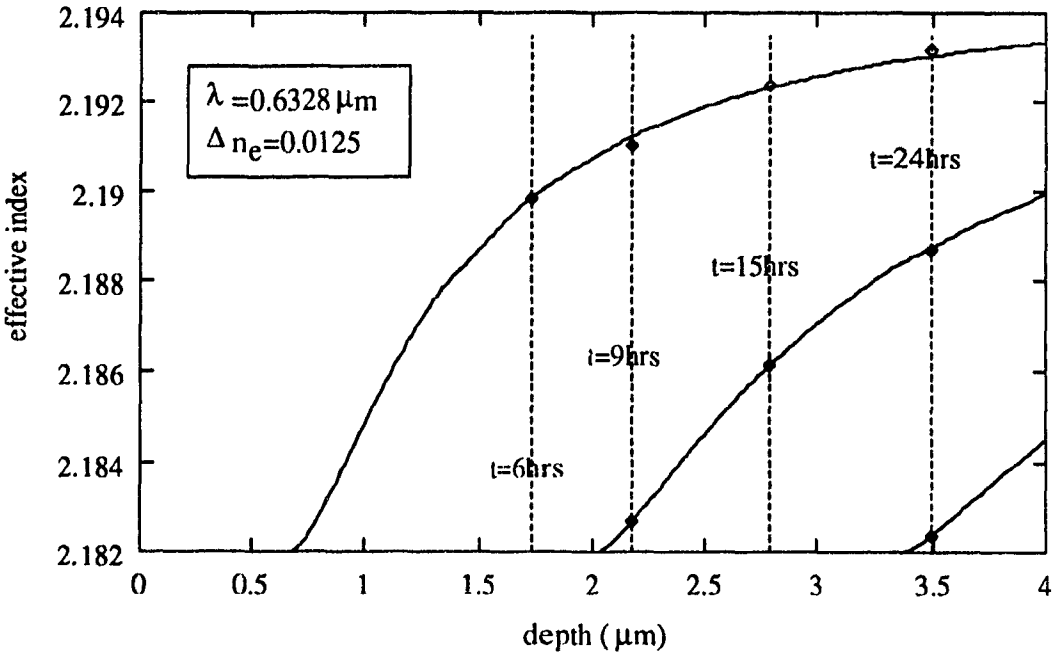

Figure 7.1: Step dispersion curves with measured data: $T_{pe} = 240°C$

7.2.2 Δn_e, d, and D_e

Figure 7.2 plots the depth d_{pe} versus the square root of the exchange time and shows that, as expected, proton-exchange in $LiTaO_3$ is a diffusion-limited process governed by the equation

$$d_{pe} = 2\sqrt{t_{pe} \times D_e(T)} \tag{7.1}$$

where $D_e(T)$ is the effective diffusion coefficient (in $\mu m^2/hr$) and varies with the exchange temperature T_{pe}. Table 7.2 presents the values of Δn_e and $D_e(T)$ found for all four exchange temperatures. It was found that Δn_e was larger for higher exchange temperatures. The dependence of D_e on temperature is given by the Arrhenius law:

$$D_e(T) = D_0 exp\left(-\frac{E_a}{kT_{pe}}\right) \tag{7.2}$$

where D_0 is a constant for diffusion ($\mu m^2/hr$), E_a is the activation energy (eV), k is Boltzmann's constant (eV/K), and T_{pe} is the exchange temperature (Kelvins). This equation is graphically illustrated in Figure 7.3, which plots the natural logarithm of D_e against the inverse of temperature. The values obtained for D_0 and E_a are given in Table 7.2. The exchange parameters for each individual waveguide is recorded in Table 7.3. Figure 7.4 plots the waveguide depth versus the exchange temperature for different fabrication times, with experimental data and some data interpolated from Figure 7.2. The close convergence of the three lines at 198.5 ± 1 °C indicates that this is the minimum temperature for proton-exchange with pyrophosphoric acid in $LiTaO_3$.

Temp.	230°C	240°C	260°C	280°C
Δn_e	0.0122	0.0125	0.0128	0.0140
D_e ($\frac{\mu m^2}{hr}$)	0.0823	0.1289	0.2823	0.5544
$D_0 = 1.1947 \times 10^8\ \mu m^2/hr$, $E_a = 0.9101$ eV				

Table 7.2: Dependence of D and Δn_e on temperature

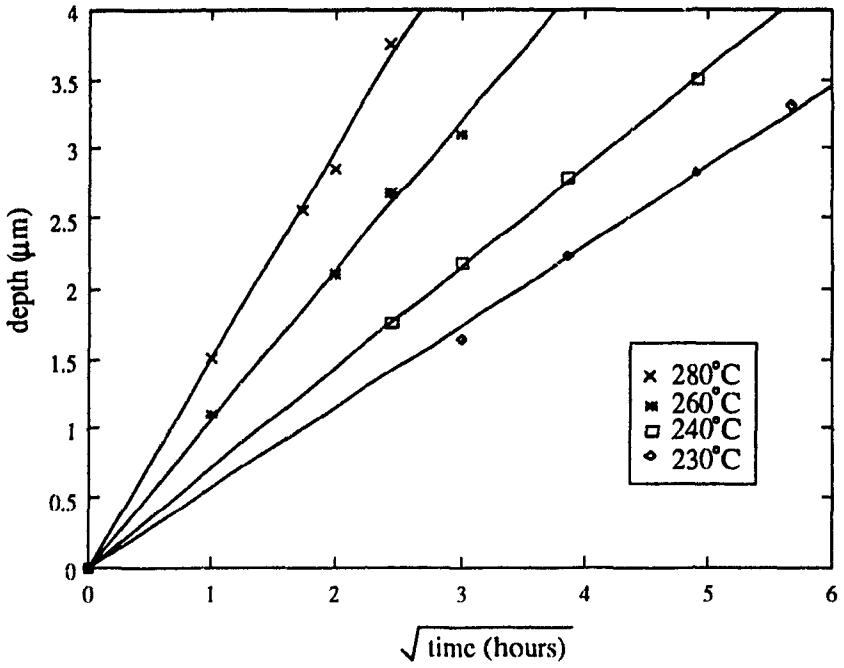

Figure 7.2: Waveguide depth d versus exchange time t

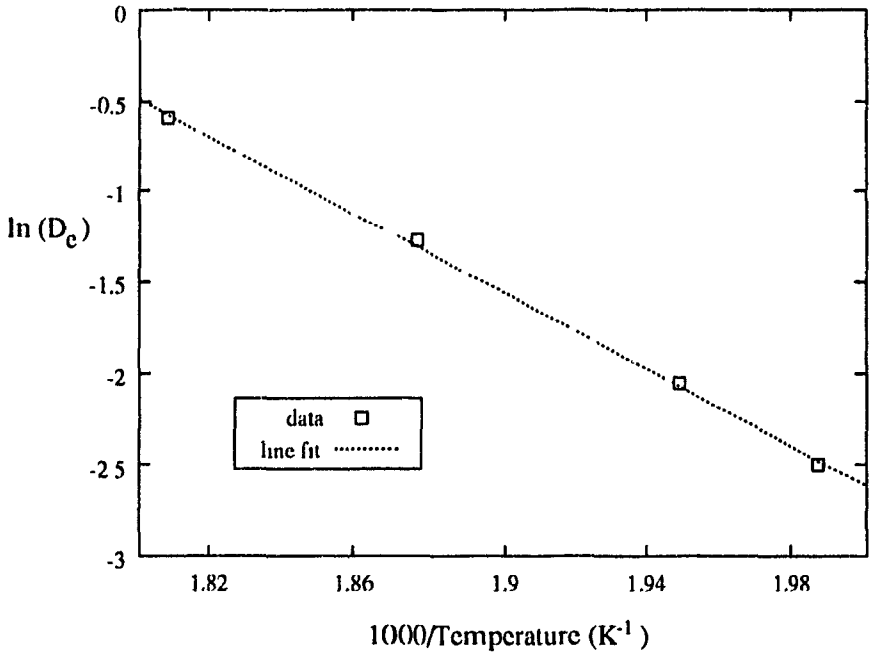

Figure 7.3: Effective diffusion coefficient D_e versus temperature $1000/T$

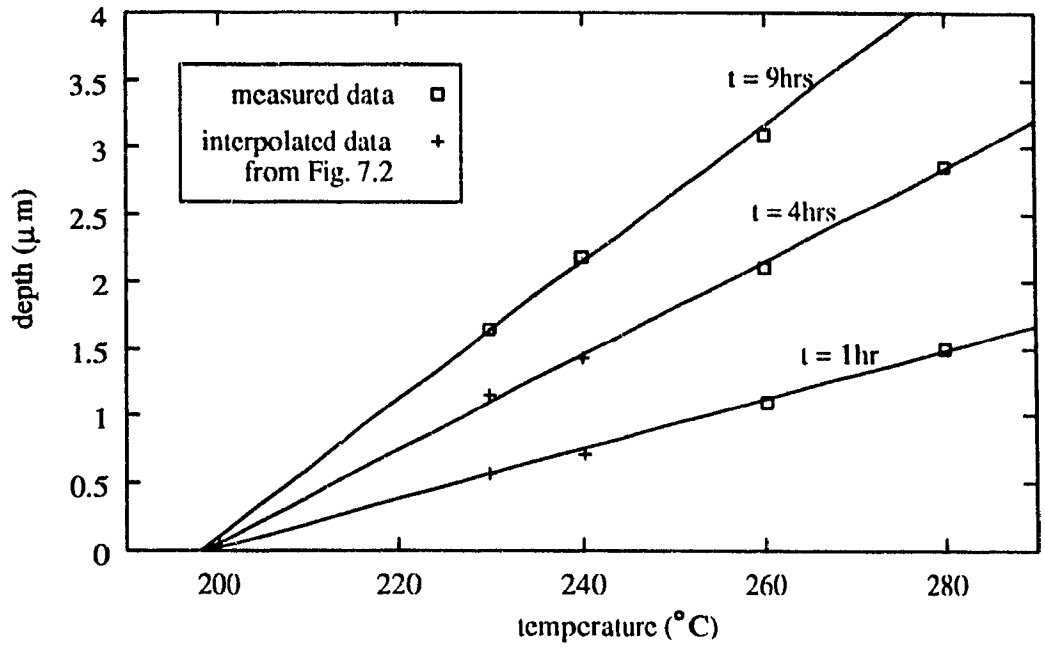

Figure 7.4: The minimum temperature for proton-exchange

Sample	modes	T_{pe} °C	t_{pe} hrs	Δn_s	d_{pe} μm	Loss (α) dB/cm
84	1	280	1	0.0140	1.51	0.7
101	2	"	3	"	2.57	*
102	2	"	1	"	2.86	*
85	3	"	6	"	3.76	1.6
73	*	"	7.5	substrate cracked		
72	*	"	9	substrate cracked		
62	1	260	1	0.0128	1.1	*
65	2	"	1	"	2.11	1.1
81	2	"	6	"	2.68	1.1
64	3	"	9	"	3.1	*
93	1	240	6	0.0125	1.74	*
63	2	"	9	"	2.18	1.0
92	2	"	15	"	2.79	1.3
83	3	"	21	"	3.5	*
61	1	230	9	0.0122	1.64	0.7
103	2	"	15	"	2.23	*
82	2	"	21	"	2.83	1.0
74	3	"	32	"	3.30	*

Table 7.3: Proton-exchange data. * indicates value not measured.

7.2.3 Propagation Loss

The propagation loss of the fundamental mode was in the range $\alpha = 0.7$ - 1.6 dB/cm, as can be seen in Table 7.3. The two lowest-loss waveguides (samples 81 and 61, both 0.7 dB/cm) were both single-moded, while the waveguide with the highest loss (sample 85, 1.6 dB/cm) supported three modes, the most of any waveguide. Most of the waveguides measured were dual-moded, and the average loss of these five waveguides (samples 65, 81, 63, 92, 82) is 1.1 dB/cm. Though this data is not extensive, it does imply that power from the fundamental mode is coupled into higher order modes (i.e. mode conversion loss). This was in fact experimentally observed - the m-lines of higher order modes could be seen even when only the fundamental mode was excited. Thus, intermodal scattering likely caused the loss of the fundamental mode to appear higher. For single mode waveguides, intermodal scattering is not a problem, so the losses are lower.

On $LiNbO_3$, the loss for single-mode pyrophosphoric acid exchanged waveguides is about 1 dB/cm lower than that of benzoic acid exchanged waveguides [42]. Our loss values (0.7 dB/cm) are on average lower than that of benzoic acid exchanged waveguides (0.7 - 1.8 dB/cm [6]), but more data is necessary to substantiate this claim.

7.2.4 Index Instability

Some waveguides were kept in storage (ambient atmosphere) after exchange and were not annealed until several months later. Their effective indices were remeasured prior to annealing, and it was observed that they had changed (see Table 7.4). The changes can be significant, even for relatively short storage durations. In general, the decrease is most pronounced for the fundamental mode, while higher order modes do not change as much (except sample 65). The longer the storage time, the greater the decrease. These results are similar to those of benzoic acid exchanged $LiNbO_3$ waveguides [68].

sample	weeks in storage	mode	n_{eff} after exchange	n_{eff} after storage	change
81	7.5	0	2.1921	2.1908	-0.0013
		1	2.1858	2.1855	-0.0003
82	8	0	2.1916	2.1905	-0.0011
		1	2.1860	2.1860	none
85	14	0	2.1917	2.1931	-0.0013
		1	2.1895	2.1893	-0.0002
		2	2.1817	2.1836	-0.0011
61	14	0	2.1891	2.1879	-0.0012
74	34	0	2.1926	2.1895	-0.0031
		1	2.1879	2.1875	-0.0001
84	38	0	2.1901	2.1868	-0.0033
65	39	0	2.1911	2.1901	-0.0010
		1	2.1821	2.1879	+0.0055
64	56	0	2.1930	2.1896	-0.0031
		1	2.1877	2.1877	none

Table 7.4: Index instabilities: fluctuation of effective indices

7.2.5 Discussion

The main advantages of pyrophosphoric acid over benzoic acid for $LiNbO_3$ waveguides is a higher Δn_e and lower propagation losses, but these effects did not seem to extend to $LiTaO_3$. Compared to z-cut, benzoic acid exchanged $LiTaO_3$ waveguides [7], our waveguides exhibit a similar D_t and a slightly lower Δn_e ($\approx$0.013 versus $\approx$0.017) at the same temperatures. Losses are lower, but there is insufficient data to claim this conclusively. Table 7.5 compares the proton-exchange waveguide studies of various workers. The results differ significantly from one worker to the next, and variations in the experimental procedure makes it difficult to compare them directly. For example, all other z-cut $LiTaO_3$ studies used surface acoustic wave (SAW) quality $LiTaO_3$, while we used a higher photonic grade. Li [7] used sealed glass tubes for the exchange, while we used unsealed glass container. The only comparable study is Li [8], who also used pyrophosphoric acid. However, their data is not as extensive, and we use the $-z$ face for exchange, while Li [8]

uses the $+z$ face. The crystal orientation crucially affects the exchange parameters.

Though our results do not point to any major advantages of pyrophosphoric acid over benzoic acid, it should be noted that waveguides may be fabricated up to five times faster in pyrophosphoric acid. This is due to the fact that the boiling point of pyrophosphoric acid is 300°C versus 250°C for benzoic acid, and the effective diffusion coefficient D_e is five times higher at 300°C than at 250°C (refer to equation 7.2). It is also possible that D_e would be higher if the waveguides were fabricated in sealed containers (acid degradation is reduced). A full explanation for the temperature dependence of Δn_e is delayed until section 7.4.2, where it will be shown that annealing effects *during* proton-exchange causes the index to increase, and the higher the temperature, the greater the index increase will be.

	z-cut $LiNbO_3$		z-cut $LiTaO_3$			
Acid	benzoic	pyro	benzoic	benzoic	pyro	**pyro**
Δn_e	0.126	0.115	0.017	0.017	0.009	**0.013**
D_e(200°C) μm^2/hr	0.078	0.113	-	0.012	0.017	**0.022**
D_e(249°C) μm^2/hr	0.763	0.845	0.184	0.823	0.262	**0.188**
D_o $\times 10^8 \mu^2$m/hr	18.4	6.43	-	36.1	0.0391	**1.195**
E_a (eV)	0.97	0.855	-	1.82	0.71	**0.91**
Loss dB/cm	2.4	≤ 1	1	0.7-1.8	0.1-0.3	**0.7**
Ref.	Clark [34]	Pun [42]	Tada [6]	Li [7]	Li [8]	**this work**

Table 7.5: Comparison of proton-exchange results

7.3 Proton-Exchange with Buffered Melts

This second study is essentially the same as the previous study on proton-exchange, but with buffered melts replacing concentrated melts. The aim is to obtain accurate characterization data. Eleven buffered waveguides were fabricated, and they were analyzed in the same way as non-buffered waveguides, except that a group Δn_e value for all waveguides fabricated at one temperature was not assumed (refer to Section 6.3). Each waveguide was individually analyzed, in order to reveal the effects of different degrees of buffering at the same exchange temperature. The data is presented in Table 7.6. Since dispersion curves are not plotted for each individual waveguide, the last column in Table 7.6 shows the error between the measured and theoretical effective index values. The Δn_e, D_e, propagation losses, and index instabilities of buffered $LiNbO_3$ waveguides depend on the amount of buffering [52], so it was assumed that the same would hold true for buffered $LiTaO_3$ waveguides.

Sample	T_{pe} °C	t_{pe} hrs	Buffering	Δn_e	d_{pe} μm	Loss (α) dB/cm	$\lvert n_{eff}(\text{meas}) \quad n_{eff}(\text{calc})\rvert$ $\times 10^{-4}$
122	280	3	1%	0.0137	2.49	1.3	2.0
121	"	"	2%	0.0136	2.51	*	0.1
123	"	"	20%	0.0136	2.52	*	1.3
75	"	6	2%	0.0137	3.7	*	1.5
53	260	8	4%	0.0122	3.07	*	0.08
112	240	13	2%	0.0117	2.72	1.0	1.8
54	"	"	4%	0.0115	2.63	*	0.37
111	"	"	6%	0.0113	2.70	*	0.31
113	230	24	2%	0.0114	3.04	*	3.0
55	"	"	4%	0.0113	2.92	1.0	1.2
114	"	"	6%	0.0112	3.03	*	0.62

Table 7.6: Buffered proton-exchange data. * indicates value not measured.

The data in Table 7.6 shows that this hypothesis was only partially correct. The use of buffered melts reduces Δn_e, but does not affect the waveguide depth d, the effective diffusion coefficient D_e, or the propagation loss α. At 230°C, the reduction in Δn_e from

its value for unbuffered waveguides is ≈0.0009; at 240°C, ≈0.0010; at 260°C, ≈0.0006; at 280°C, ≈0.0003. Figure 7.5 plots Δn_e versus exchange temperature T_{pe}, comparing pure melt against buffered melt results. The empirical curve fit gives the relations

$$\Delta n_e = 6.59 \times 10^{-7}\, T_{pe}^2 - 3.03 \times 10^{-4}\, T_{pe} + 4.7 \times 10^{-2} \qquad \text{for pure melts} \qquad (7.3)$$

$$\Delta n_e = 7.68 \times 10^{-7}\, T_{pe}^2 - 3.46 \times 10^{-4}\, T_{pe} + 5.03 \times 10^{-2} \qquad \text{for 1\% buffering} \qquad (7.4)$$

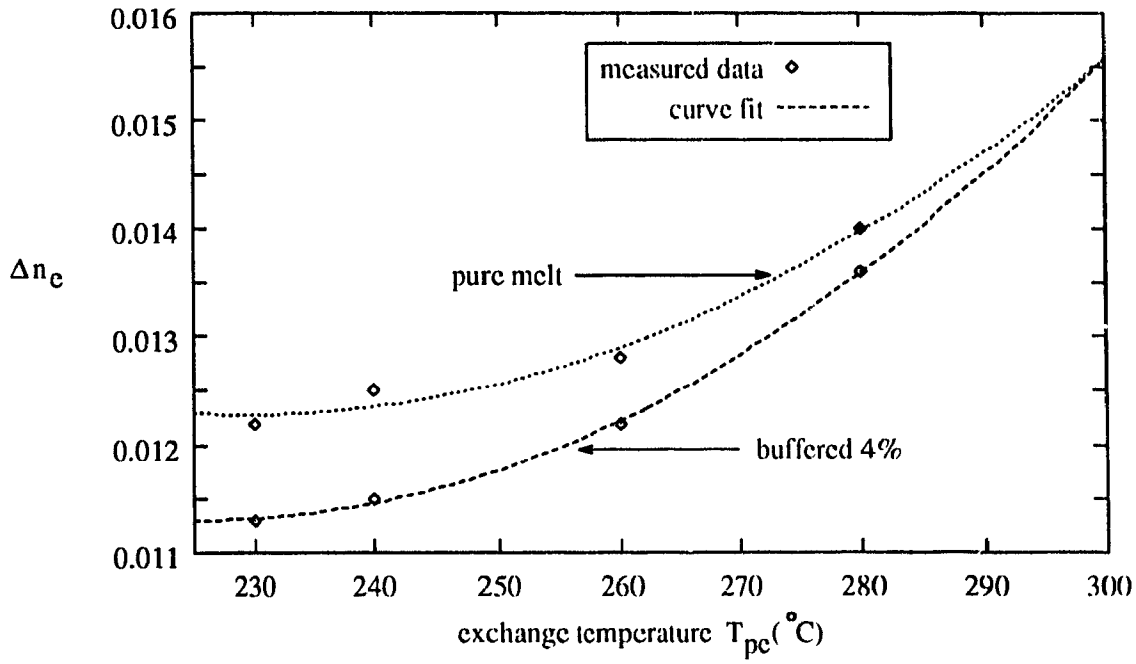

Figure 7.5: Comparing Δn_e for buffered (4%) and unbuffered melts

The reduction in Δn_e was temperature dependent, being greater at lower exchange temperatures. An explanation for this dependence will be given in section 7.4.2, where it will be shown that annealing effects *during* proton-exchange are greater at higher temperatures, thus nullifying buffering effects. Not only is the Δn_e reduction greater at a lower T_{pe}, it is also more sensitive to the amount of buffering. As the amount of lithium phosphate increases, Δn_e decreases. This trend can be clearly observed for temperatures of 230°C and 240°C (see Table 7.6). At 280°C, however, buffering up to 20% does not further reduce Δn_e from its value at 2% buffering. The buffering effect saturates quickly

at high temperatures.

7.3.1 Index Instability

It was hoped that the index instabilities could be eliminated in buffered $LiTaO_3$ waveguides. Unfortunately, buffered waveguides are still plagued by instabilities, even up to 6% dilution. The changes in the effective indices are similar to those observed in non-buffered waveguides of the previous section. With increased storage time, the changes are greater. Table 7.7 shows these instabilities.

sample	buffering	weeks in storage	mode	n_{eff} after exchange	n_{eff} after storage	change
111	6%	7	0	2.1910	2.1901	-0.0006
			1	2.1847	2.1849	+0.0002
114	6%	7	0	2.1914	2.1905	-0.0009
			1	2.1860	2.1857	-0.0003
112	2%	7.5	0	2.1913	2.1905	-0.0008
			1	2.1851	2.1847	-0.0004
113	2%	7.5	0	2.1913	2.1903	-0.0010
			1	2.1862	2.1858	-0.0004
53	4%	9.5	0	2.1924	2.1910	-0.0014
			1	2.1871	2.1867	-0.0004
54	4%	9.5	0	2.1911	2.1899	-0.0012
			1	2.1845	2.1842	-0.0003
55	4%	9.5	0	2.1914	2.1901	-0.0013
			1	2.1857	2.1858	+0.0001

Table 7.7: Index instability of buffered waveguides: change of effective indices

7.3.2 Discussion

The effects of buffering the pyrophosphoric acid with lithium phosphate were limited. Only Δn_e was reduced, while index instabilities, propagation losses, d, and D_e all remained unaffected. The chief benefits of buffered melts - elimination of index instabilities and reduction of propagation losses - were not observed. However, one major benefit of buffering is revealed by these results. With unbuffered waveguides, the only way to con-

trol Δn_e is through the exchange temperature. If a low Δn_e is desired, one must choose a low T_{pe}, for which D_e is very small and therefore all but the shallowest waveguides will require days to exchange. With buffering, one can obtain low Δn_e values (even lower than unbuffered waveguides) but still work at a high T_{pe}, for which diffusion will be much faster. Buffering is a tool for tailoring the index change Δn_e according to design requirements, and thus provides enhanced flexibility in choosing the fabrication conditions.

The only published work on buffered z-cut $LiTaO_3$ waveguides that cites values for Δn_e and D_e was made by Yuhara and Tada [80]. They reported an increase in Δn_e for buffering up to 2%, after which it decreased. As well, D_e was reduced. Our data differs markedly from theirs, though different experimental conditions may account for these discrepancies. They used buffered benzoic acid melts, the +z surface, and very long diffusion times (48 hours and 121 hours). The effects of buffering may be entirely different in pyrophosphoric acid from those in benzoic acid.

Surprisingly, d and D_e were not affected while Δn_e was. This suggests that proton-exchange mechanisms are different in $LiTaO_3$ from $LiNbO_3$. Hydrogen diffuses into the $LiTaO_3$ crystal via two different processes: the first is an exchange reaction with lithium; the second is a surface reaction with water (see Section 3.5.1). The latter is not lithium concentration dependent. Perhaps, this is the dominant reaction for proton-exchange in $LiTaO_3$, while the exchange reaction is the dominant reaction for $LiNbO_3$. This would explain why buffering seems to have a limited effect, and would also explain the difference in diffusion speeds. An alternative explanation is that lithium precipitates out of solution as the acid degrades during proton-exchange. The solubility of lithium phosphate in pyrophosphoric acid saturates at low concentrations, so even high levels of buffering would have little effect on the waveguide. These explanations are speculative in nature, and further work would be required to provide a greater understanding of this result.

7.4 Annealed Waveguides

The effects of annealing on the refractive index profile of proton-exchanged waveguides was studied and carefully characterized. Upon annealing, the protons diffuse further into the substrate, causing the step-index profile to increase in depth and to gradually smooth out into a graded-index profile. The change in the surface index Δn_s ($\Delta n_s = n_s - n_b$) and the change in the waveguide depth Δd ($\Delta d = d - d_{pe}$) were monitored throughout annealing. The evolution of the index profile with anneal time t_a for four waveguides is shown in Figures 7.6 - 7.9. Of the sixteen annealed waveguides, the profiles of only four representative waveguides are shown. Each waveguide was annealed at a different temperature. All the annealing data presented here is from waveguides proton-exchanged in concentrated melts. Section 7.4.5 contains the annealing data for waveguides exchanged in buffered melts.

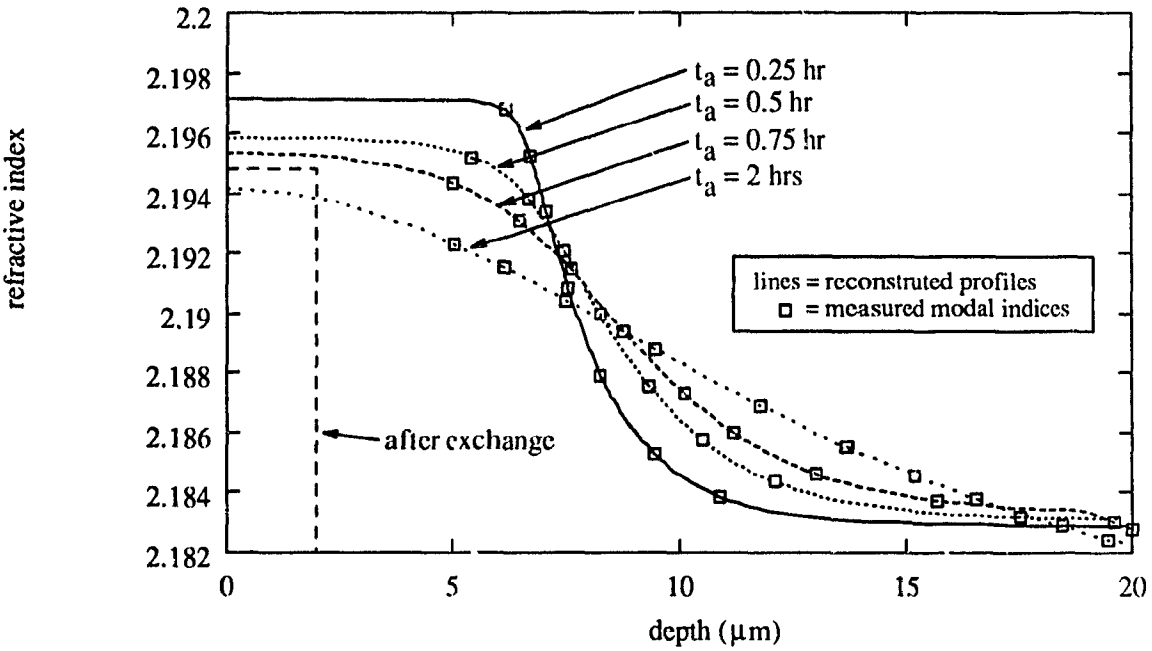

Figure 7.6: Index profiles of annealed waveguide (T_a = 500°C): sample 63

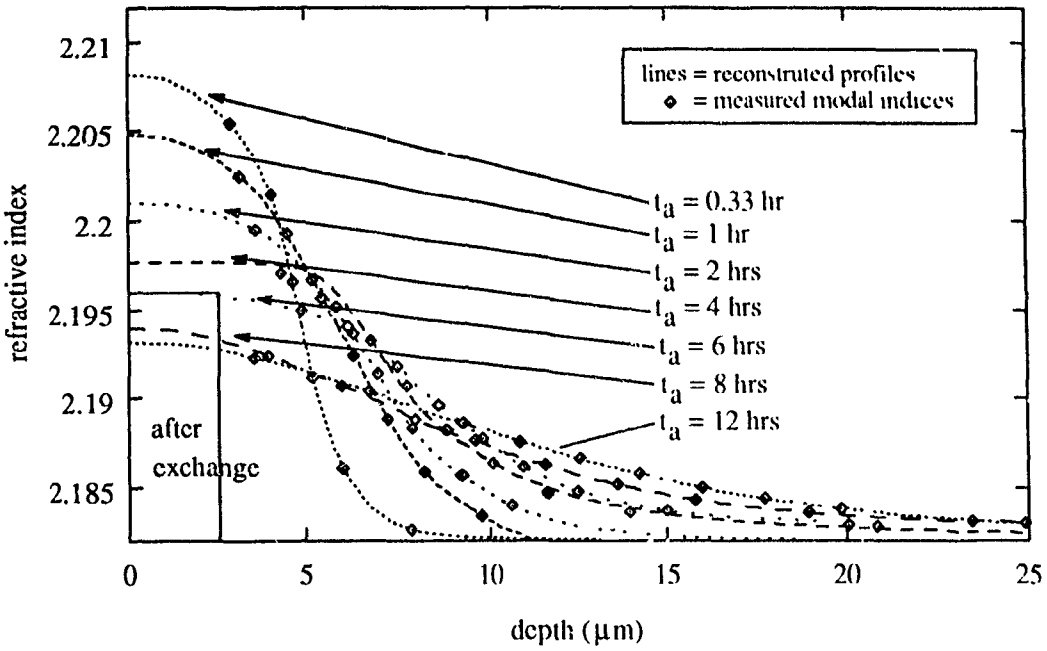

Figure 7.7: Index profiles of annealed waveguide (T_a = 400°C): sample 101

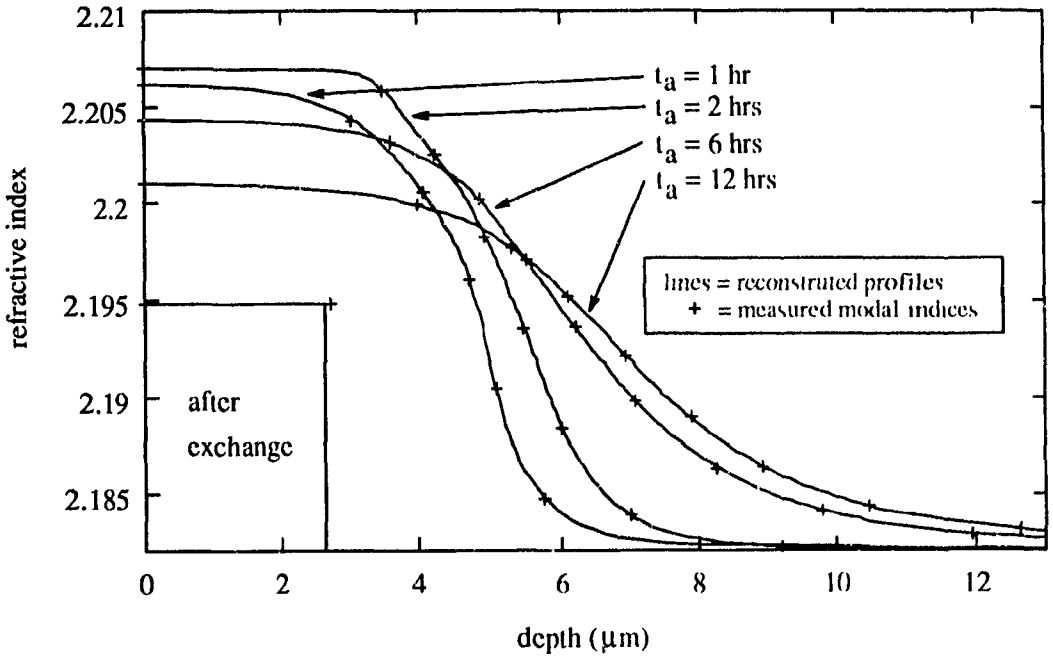

Figure 7.8: Index profiles of annealed waveguide (T_a = 350°C): sample 81

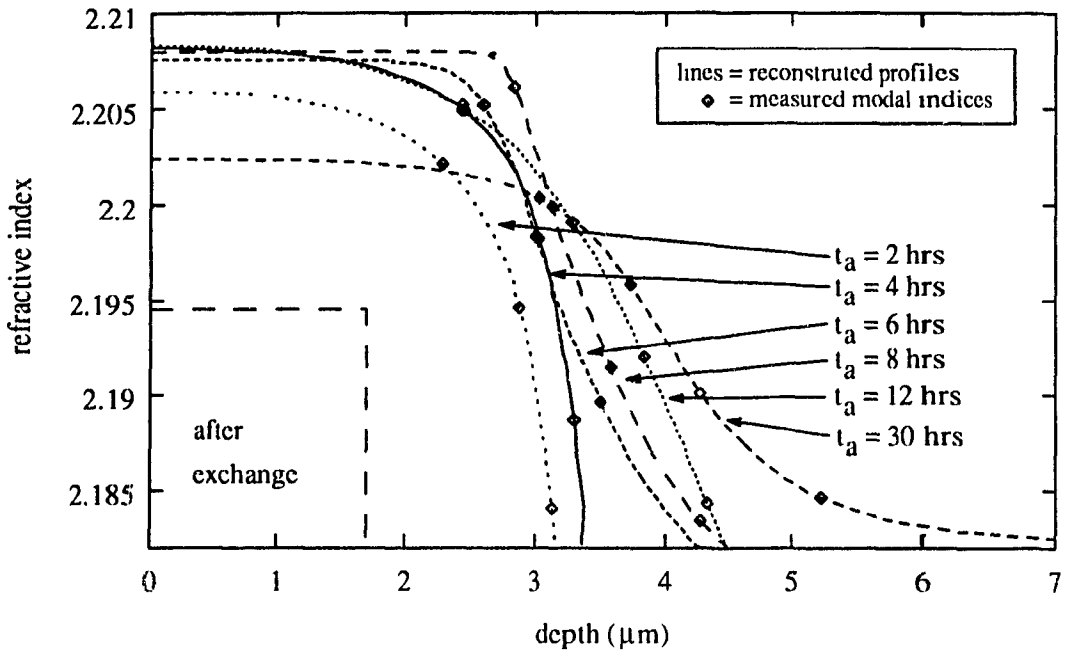

Figure 7.9: Index profiles of annealed waveguide (T_a = 300°C): sample 93

7.4.1 Change in Depth Δd

The change in the waveguide depth Δd as a function of anneal time is plotted in Figures 7.10-7.12. The shape of the Δd curve is most strongly affected by the anneal temperature T_a: after 2 hours of annealing, Δd is approximately 1.1μm for T_a = 300°C (Fig. 7.10) and 10.1μm for T_a = 500°C (Fig. 7.12). The higher the temperature, the faster and greater the depth increase will be. For a fixed T_a, the initial proton-exchange conditions determine the shape of the curve: after 4 hours of annealing at T_a = 400°C (Fig. 7.12), Δd = 5.9μm for sample 84 (d_{pe} = 1.5μm) and 7.5μm for sample 74 (d_{pe} = 3.3μm). For pure melts, the greater the proton-exchanged depth, the greater the depth increase Δd will be during annealing.

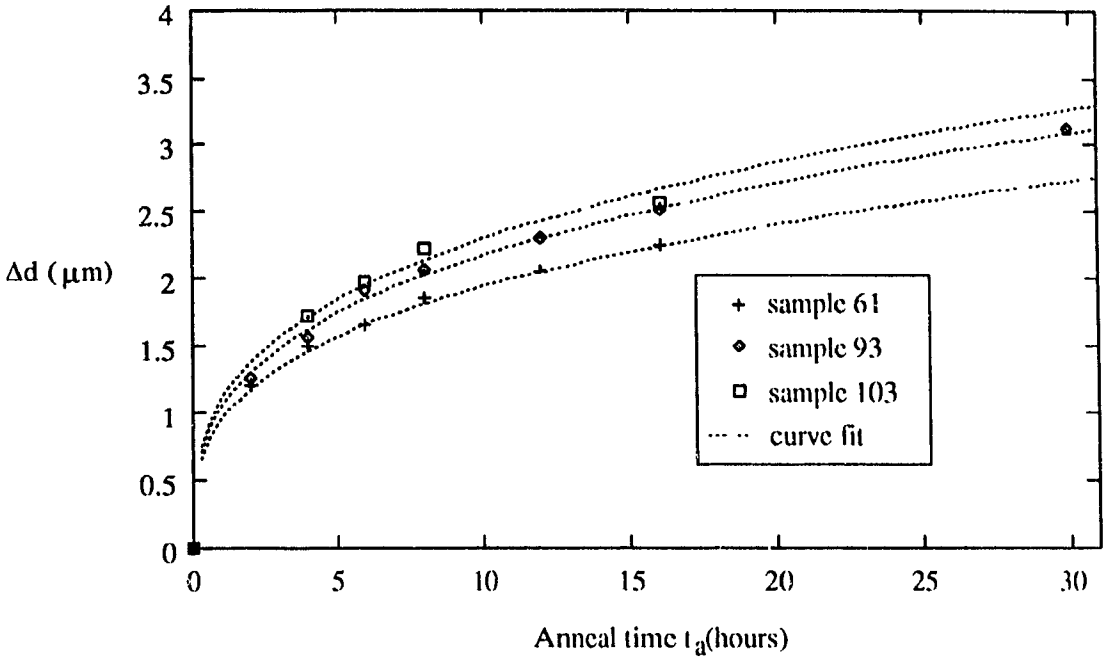

Figure 7.10: Change in anneal depth Δd versus anneal time: $T_a = 300°C$

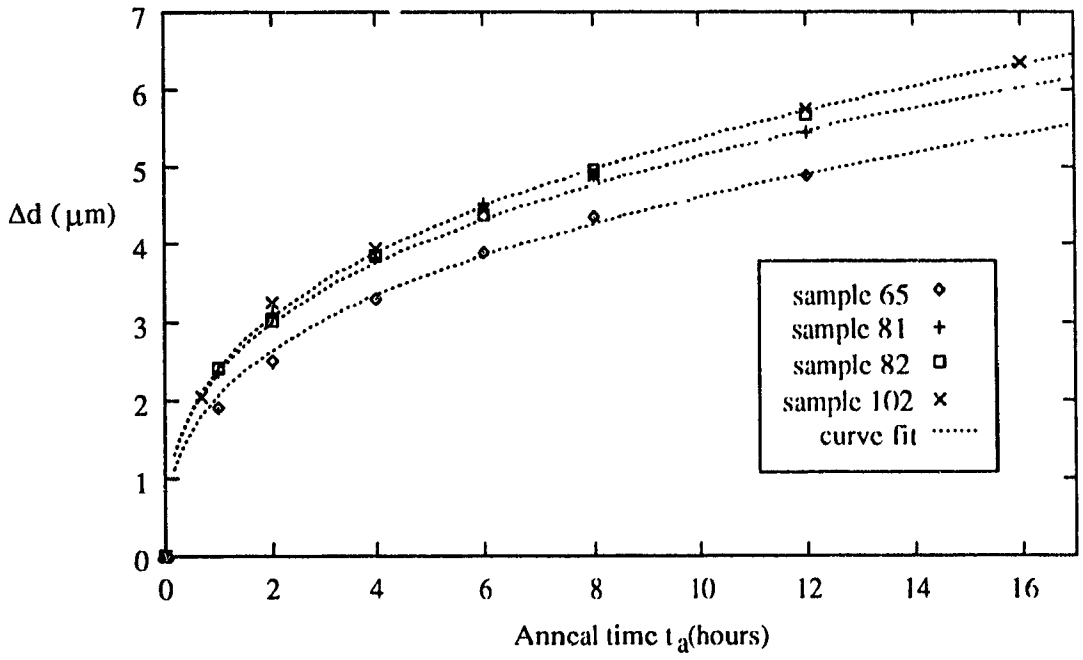

Figure 7.11: Change in anneal depth Δd versus anneal time: $T_a = 350°C$

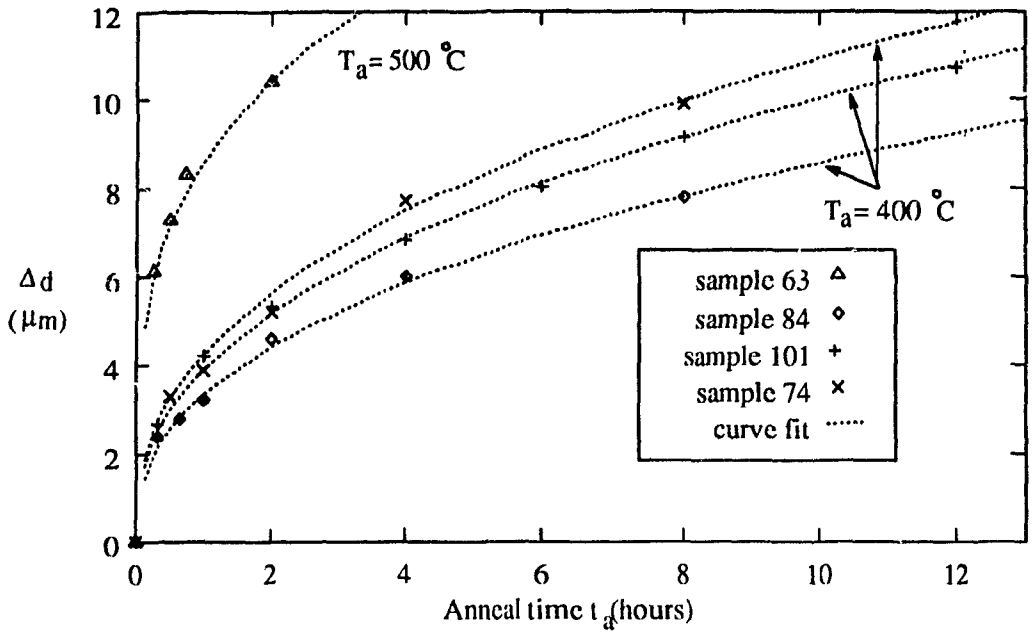

Figure 7.12: Change in anneal depth Δd versus anneal time: T_a = 400°C, 500°C

Empirical Relations

The waveguide depth has a simple power law dependence on the anneal time:

$$\Delta d = d - d_{pe} = b\, t_a^c \tag{7.5}$$

where d is the waveguide depth (for a generalized Gaussian profile, as defined in equation 6.3), d_{pe} the depth after proton-exchange, t_a the anneal time, and b, c are curve-fitting parameters which depend on the anneal temperature and the initial exchange conditions. This equation has previously been used [38, 42] to describe the depth in annealed $LiNbO_3$ waveguides. The values of b and c are given in Table 7.8.

The parameters b and c are well correlated with the anneal temperature T_a and the proton-exchanged depth d_{pe}. Figure 7.13 plots b against d_{pe} for three anneal temperatures, and the dependence is shown to be quite linear. The relation is given by

$$b = \quad 0.17 d_{pe} + 2.7 \quad \text{for } T_a = 400°C \tag{7.6}$$

$$b = 0.47 d_{pe} + 1.075 \quad \text{for } T_a = 350°C \tag{7.7}$$

$$b = 0.47 d_{pe} + 0.16 \quad \text{for } T_a = 300°C \tag{7.8}$$

The parameter c is seen in Table 7.8 to be constant for all waveguides annealed at the same temperature. For different anneal temperatures, its value varies. Figure 7.11 plots the value of c against T_a. The data at 500°C consists of only one point and seems to be an aberration, so it is not included. Otherwise, the dependence of c on T_a is a polynomial expression given by

$$c = 4 \times 10^{-6} T_a^2 - 2 \times 10^{-3} T_a + 0.56 \tag{7.9}$$

The annealed waveguide depth d has been carefully characterized and related to the annealing conditions. With the empirically derived equations of 7.5 to 7.9, the waveguide designer will be able to select the anneal temperature T_a, anneal time t_a, and proton-exchanged depth d_{pe} required to fabricate a waveguide of a desired depth d. Examples of how this is done will be presented in Section 7.5.

Sample	T_a °C	d_{pe} μm	T_{pe} °C	t_{pe} hours	b hrs^{-c}	c
63	500	2.18	210	9	8.6	0.28
84	400	1.51	280	1	3.4	0.10
101	"	2.57	280	3	3.93	0.40
74	"	3.3	230	32	4.26	0.40
65	350	2.11	260	4	2.06	0.35
81	"	2.68	260	3	2.35	0.35
82	"	2.83	230	21	2.4	0.35
102	"	2.86	280	1	2.4	0.35
61	300	1.64	230	9	0.95	0.31
93	"	1.71	210	6	1.04	0.32
103	"	2.23	230	15	1.1	0.32

Table 7.8: Annealing parameters for $\Delta d = b\, t_a^c$

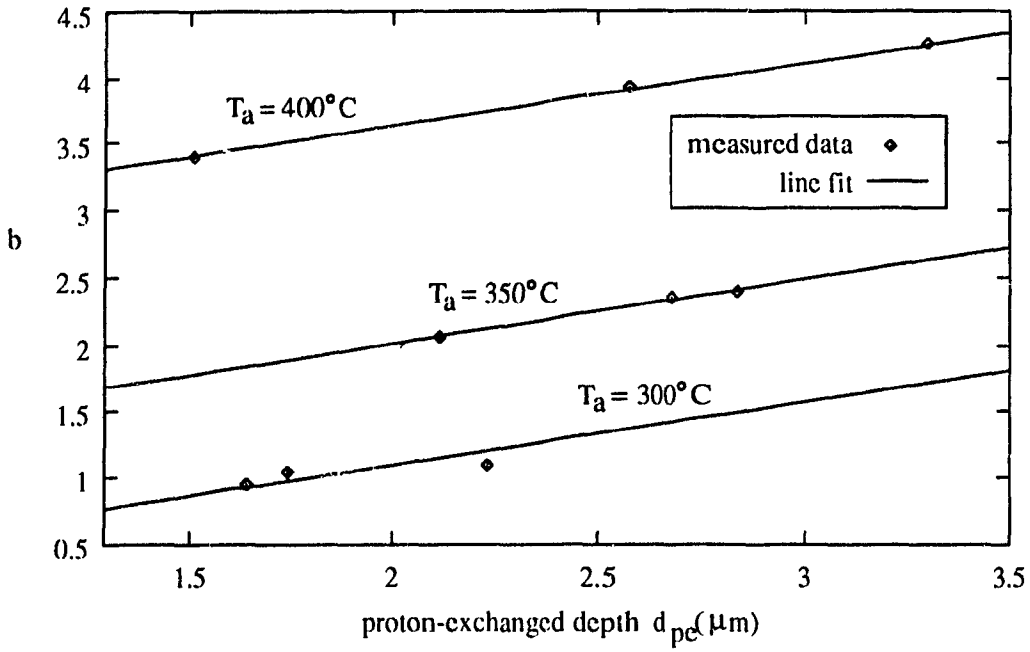

Figure 7.13: Dependence of b on d_{pe}

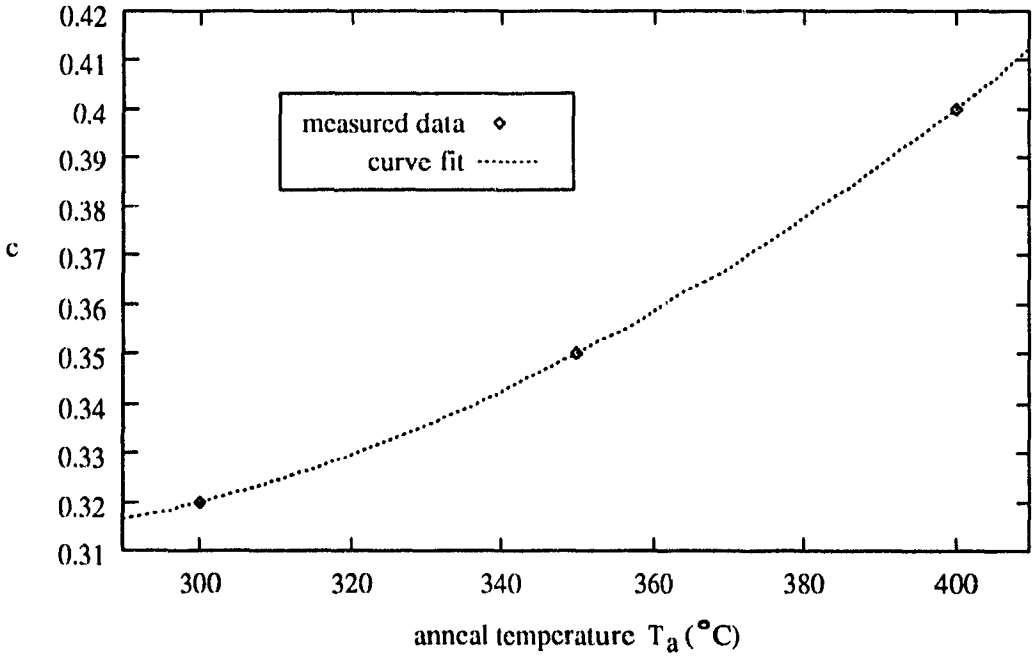

Figure 7.14: Dependence of c on anneal temperature T_a

7.4.2 Surface Index Increase Δn_s

With annealing, the waveguide's surface index initially increases quickly, peaks, and then decreases slowly. The variation of the surface index increase Δn_s with anneal time t_a is shown in Figures 7.15 - 7.17. As discussed in Chapter 1, the conversion of H-OH ions to OH ions causes this increase. When most of the H-OH ions have been converted, the surface index peaks and then declines due to diffusion. The rate of conversion is greater at higher temperatures: for T_a = 300°C the index peak occurs at about 16 hours (see Fig. 7.15); for T_a = 500°C the peak occurs before 15 minutes (see Fig. 7.17). Anneal temperatures of 350°C or 400°C strike a good balance between processing time and accurate control over the surface index.

The surface index increase upon annealing explains the dependence of Δn_e on temperature for proton-exchange. Temperatures of 230°C to 280°C are high enough for annealing to take place simultaneously with proton-exchange, albeit at a slow rate. This slow and continuous annealing process converts H-OH ions into OH ions even *during* proton-exchange. Since the conversion is faster at higher anneal temperatures, Δn_e will consequently also be greater at higher exchange temperatures. This annealing effect, which increases Δn_e, will in part nullify the effects of buffering, which decreases Δn_e. This explains why the effects of buffering are more pronounced at lower exchange temperatures, where the annealing effect is weaker. For pure proton-exchange, Δn_e may also depend on the exchange time. More H-OH ions are converted for longer exchange times, so the index increase ought to be greater. Therefore, the combination of a higher temperature and longer duration should produce a waveguide with a larger Δn_e; conversely, a lower temperature and shorter duration should produce a smaller Δn_e.

The general behaviour of Δn_s in Figures 7.15 - 7.17 is thus: initially, Δn_s increases, with the slope of the curve positive and decreasing. The slope approaches zero at the Δn_s peak (Δn_{pk}), which has an average value of 0.02566 (standard deviation = 0.00065).

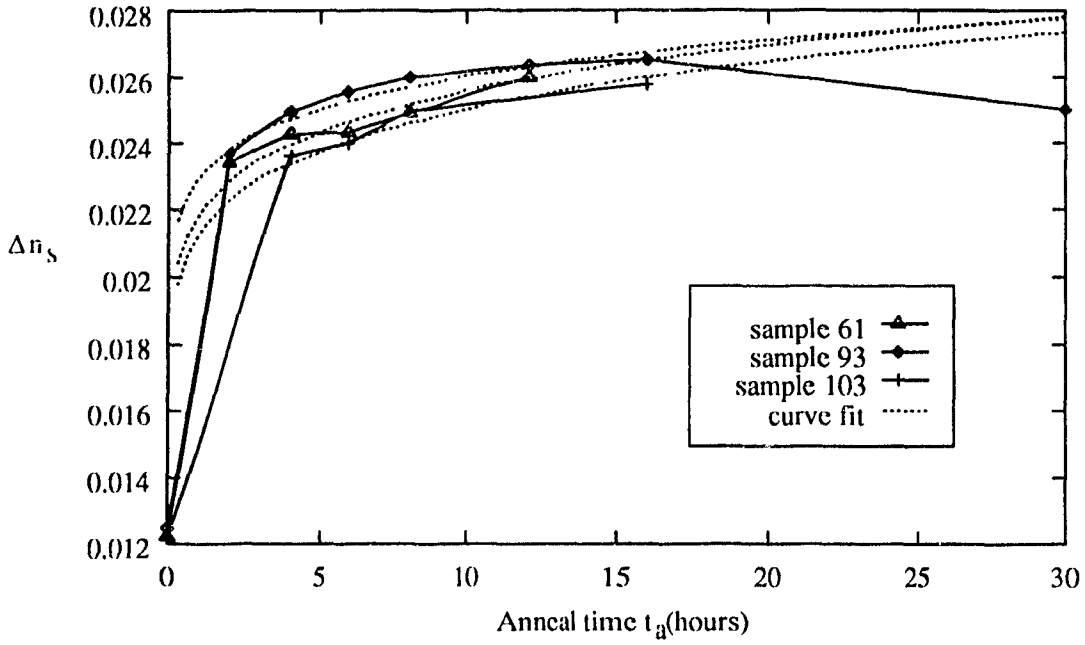

Figure 7.15: Surface index increase Δn_s versus anneal time: T_a = 300°C

Then Δn_s begins to descend, and the slope is negative and still decreasing. The slope then reaches an inflexion point and begins to increase. The surface index continues to decrease but the slope approaches zero for very long anneal times (see Fig. 7.17).

At a fixed T_a, the influence of the initial proton-exchange conditions is apparent. Comparing sample 65 (d_{pe} = 2.1μm) with sample 102 (d_{pe} = 2.86μm) in Fig. 7.16, it is observed that the index peak Δn_{pk} occurs later for the waveguide with the larger d_{pe}. For two waveguides with the same d_{pe}, the measured peak occurs later for the waveguide exchanged at a higher T_{pe} (compare samples 82 [T_{pe} = 230°C] and 102 [T_{pe} = 280°C] in Figure 7.16). The index peak deserves closer scrutiny. When the depth d at Δn_{pk} (this depth is refered to as d_{pk}) is normalized by the waveguide's proton-exchanged depth, it was found that the ratio d_{pk}/d_{pe} was very similar for all waveguides, regardless of the anneal temperature. The average value was d_{pk}/d_{pe} = 2.27, with the standard deviation = 0.15. For example, d_{pk} = 6.8μm for sample 102, and d_{pk}/d_{pe} = 2.38. The measured Δn_{pk} may not be the highest that Δn_s reaches, since the annealing and hence the measurement

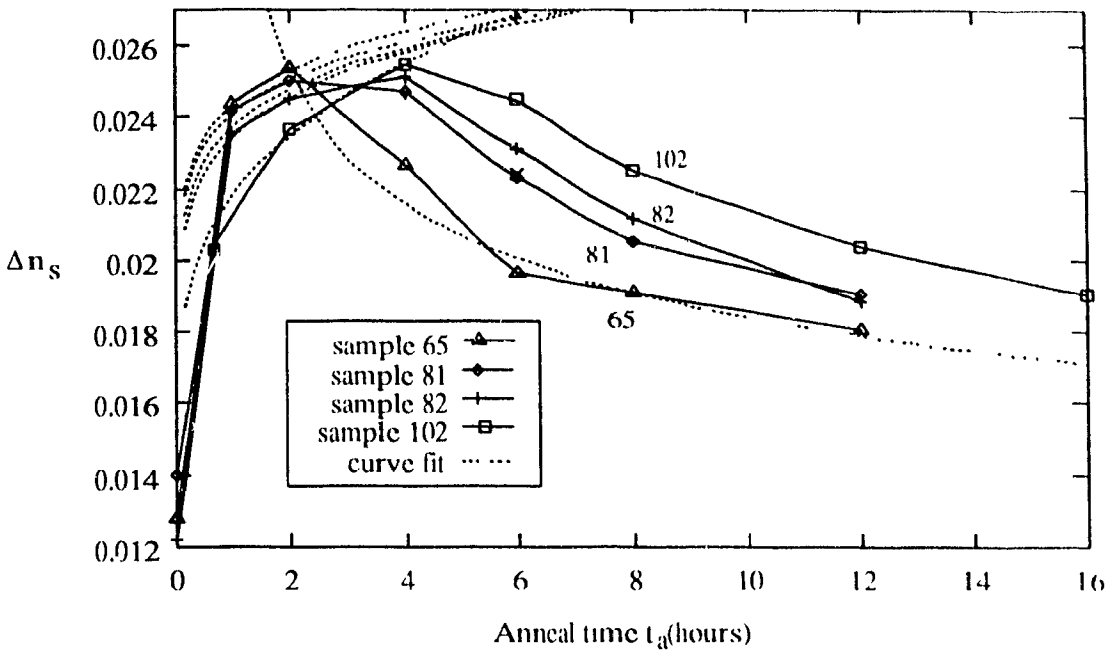

Figure 7.16: Surface index increase Δn_s versus anneal time: $T_a = 350°C$

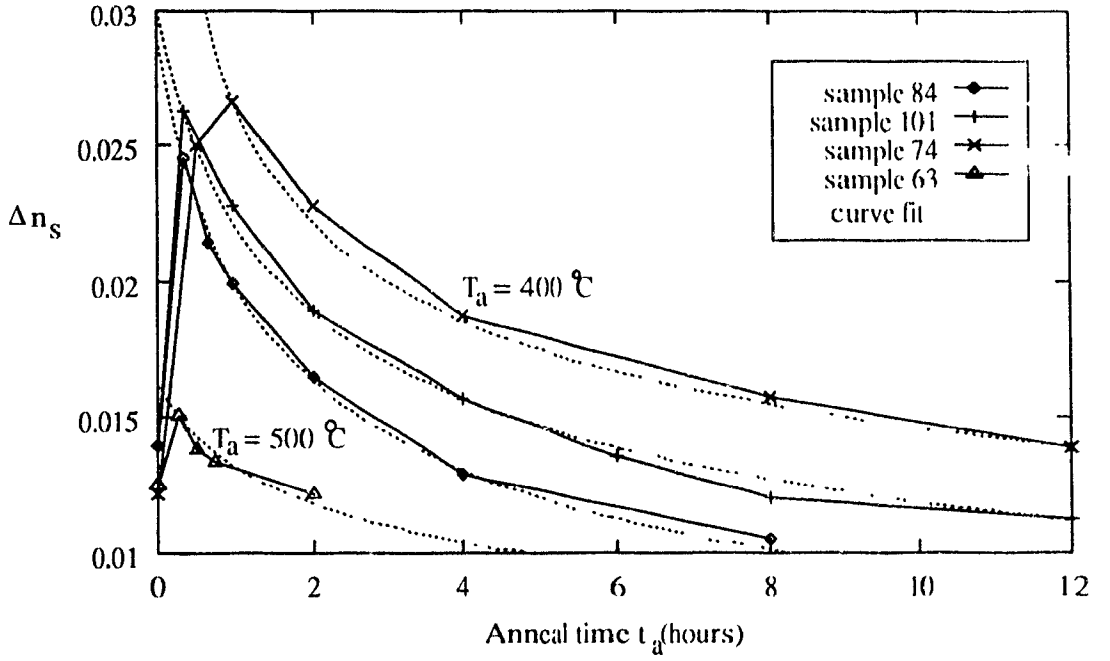

Figure 7.17: Surface index increase Δn_s versus anneal time. T_a = 400°C, 500°C

interval is not fine enough to resolve the exact peak. The exact peak will occur slightly before or after the measured peak, and be slightly higher. As for the height of the measured peak, there is some variation in the values but no discernible relation to either proton-exchange conditions or T_a. In general, the Δn_s versus t_a curve exhibits more complicated behaviour and dependencies than the Δd versus t_a curve.

Empirical Relations

After attempting several curve fits (e.g. polynomial, exponential, etc.), the following power law relations have been found to provide the best fit to the Δn_s versus t_a curves. In region of initial increase, up to the peak, the relation is given by:

$$\Delta n_s = \Delta n_\epsilon + \epsilon\, t_a^f \tag{7.10}$$

where Δn_ϵ is the index increase due to proton-exchange, and ϵ, f are curve fitting parameters. This formula was fitted to the data for T_a = 300°C and T_a = 350°C, as shown in Figures 7.15 and 7.16. For T_a = 400°C and T_a = 500°C, Δn_s peaks quickly and there are not enough data points for a meaningful curve fit. Another power law relation is used to fit the data after the peak:

$$\Delta n_s = \Delta n_{pk}[t_a - t_{pk} + 1]^g \tag{7.11}$$

where Δn_{pk} is the measured Δn_s peak, t_{pk} is t_a at Δn_{pk}, and g a fitting parameter. This formula was fitted to the data for T_a = 350°C, 400°C and 500°C, as shown in Figures 7.16 and 7.17. For T_a = 300°C, Δn_s peaks very slowly and there are not enough data points for a curve fit. The values of ϵ, f, Δn_{pk}, and g are given in Table 7.9. The parameter g was found to be linearly related to $d_{p\epsilon}$ (see Figure 7.18); the relations are given by

$$g = 0.086 d_{p\epsilon} - 0.55 \quad \text{for } T_a = 400°C \tag{7.12}$$

$$g = 0.010 d_{p\epsilon} - 0.23 \quad \text{for } T_a = 350°C \tag{7.13}$$

Unfortunately, a dependence on fabrication conditions could not be found for ϵ or f. Nevertheless, equations 7.10 - 7.13 can be used to select the proper annealing conditions for a waveguide with almost any desired Δn_s. Examples of how these equations and graphs can be used will be presented in Section 7.5.

Sample	T_a °C	d_{pe} μm	ϵ hrs^{-f}	f	Δn_{pk} hrs^{-g}	g
63	500	2.18	*	*	0.0151	-0.21
84	400	1.51	*	*	0.0265	-0.11
101	"	2.57	*	*	0.0268	-0.35
74	"	3.3	*	*	0.0266	-0.26
65	350	2.11	0.0115	0.12	0.02534	-0.115
81	"	2.68	0.01125	0.12	0.025	-0.115
82	"	2.83	0.0112	0.14	0.0251	-0.128
102	"	2.86	0.0078	0.28	0.02514	-0.11
61	300	1.64	0.0097	0.11	*	*
93	"	1.74	0.0105	0.11	*	*
103	"	2.23	0.0091	0.15	*	*

Table 7.9: Annealing parameters for Δn_s. * indicates values not obtained.

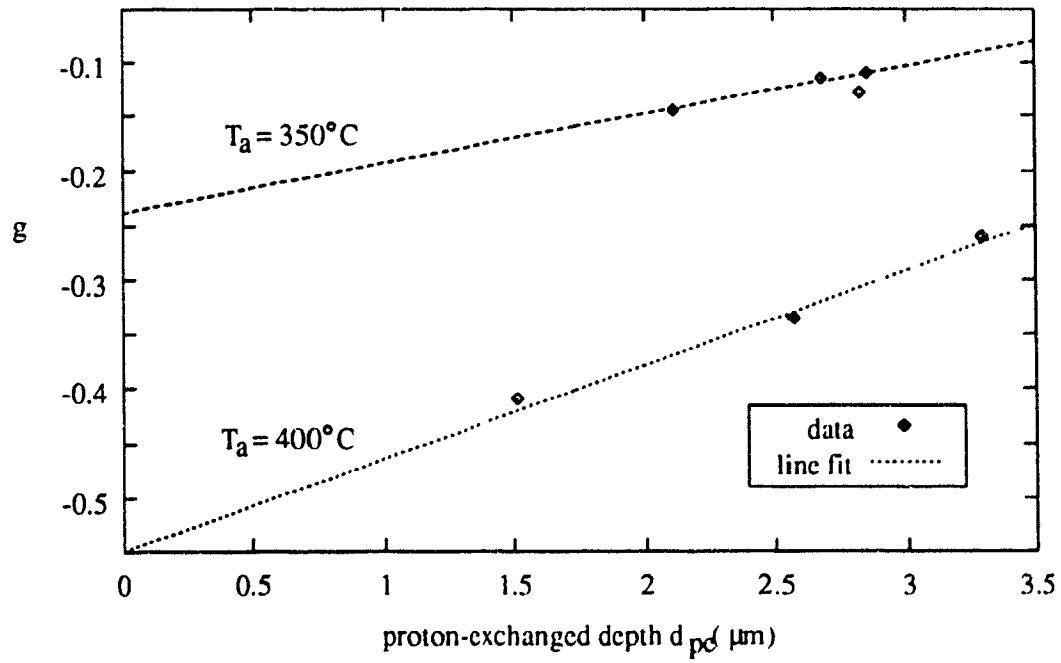

Figure 7.18: Linear dependence of g on d_{pe}: T_a = 350°C, 400°C

7.4.3 Index Profile Area and Index Instability

The area of the index profile (the integral of the refractive index profile with respect to depth) is a measure of total amount of OH ions in the waveguide. The H-OH ions do not affect the refractive index, but as the H-OH ions are converted into OH ions during annealing, both Δn, and d increase, resulting in a growing index profile area. The area is plotted against anneal time in Figure 7.19. After most or all of the H-OH ions are converted, the area levels off to a stable value, or a plateau. This plateau area ar_{pl} can be quantified by taking the average of all the areas in the stable region. The start of the plateau is found by noting the time t_a when the area begins to level in Fig. 7.19. It was observed that for all waveguides, no significant changes in the area occur after t_{pk}, the time when the index peak is reached. Thus, t_{pk} defines the start of the plateau. For sample 74, t_{pk} = 1hr, the plateau area ar_{pl} = [0.171(1hr) + 0.173(2hrs) + 0.179(4hrs) + 0.183(8hr) + 0.168(12hr)]/5 = 0.175. Tables 7.10-7.12 contains the parameters t_{pk}, ar_{pl}, and other annealing data for each waveguide. The column in these tables, labelled "poly. deg.", gives the degree of the polynomial effective index function used in the IWKB reconstruction of that index profile (refer to Section 6.4). Different degrees may be used, resulting in slightly different reconstructed profiles, so the degree actually used is given here to prevent confusion.

Annealing condition for eliminating index instabilities

It was observed that the effective indices of waveguides annealed for less than the time required for attaining the plateau area were not stable. Similar to index instabilities in proton-exchanged waveguides, the effective indices of the fundamental and first-order modes decreased, while higher order modes did not change much. The indices were stable for long anneal times (for example, 30 hours at 300°C, 16 hours at 350°C, and 6 hours at 400°C). The source of index instabilities are believed to be H-OH ions. When they are all

converted into OH ions, index instabilities should disappear. The H-OH ions are almost fully converted when the index profile area of the waveguide reaches the plateau area. In order to ensure that the waveguide is free of index instabilities, it should be annealed into this stable region. The plateau begins at $t_a = t_{pk}$, so the anneal time necessary to guarantee stable waveguides is given by

$$t_a \geq t_{pk} \tag{7.11}$$

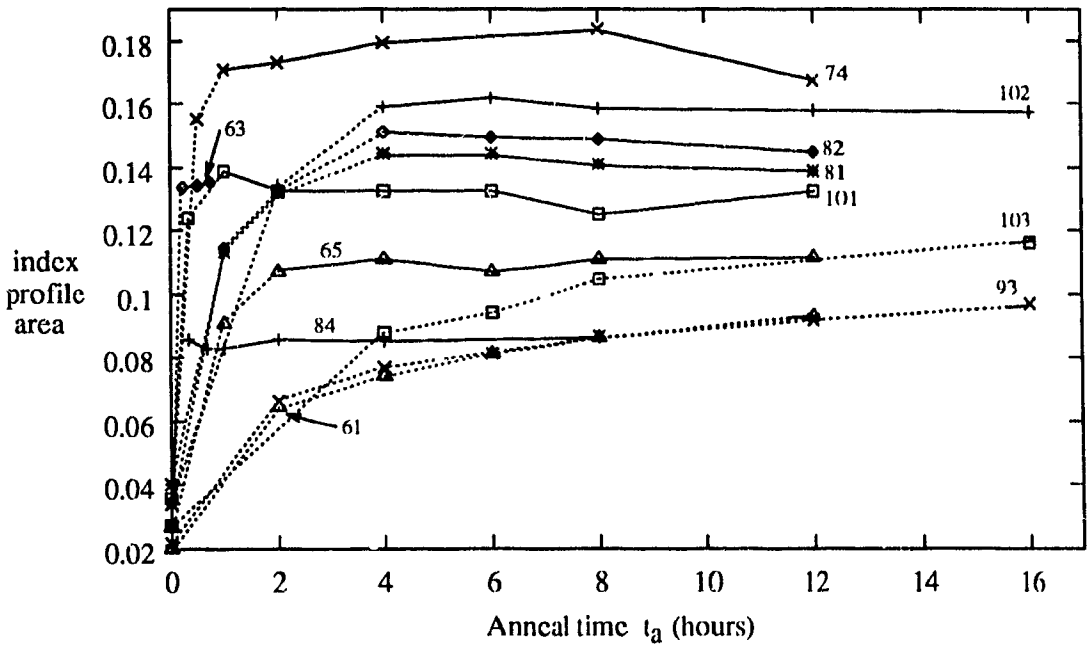

Figure 7.19: Area of index profiles with time. Samples are labelled by their number. Solid lines indicate the areas used in the calculation of ar_{pl}.

A waveguide's plateau area ar_{pl} was found to be related to its index profile area after proton-exchange (ar_{pe}). Figure 7.20 plots ar_{pl} against ar_{pe}, and a simple linear dependence is observed (see Fig. 7.20 for the empirical equations). For the same proton-exchange area ar_{pe}, the plateau area ar_{pl} is greater for waveguides exchanged at T_{pe} = 230°C than at T_{pe} = 280°C (see Fig. 7.20). Since the proton-exchange area $ar_{pe} = \Delta n_e \times d_{pe}$, and d_{pe} is a function of both temperature T_{pe} and time t_{pe}, a longer t_{pe} is needed to achieve the same ar_{pe} at a lower T_{pe}. The longer the exchange time, the greater the number of H-OH

ions that diffuse into the waveguide, and hence the greater ar_{pl} will be.

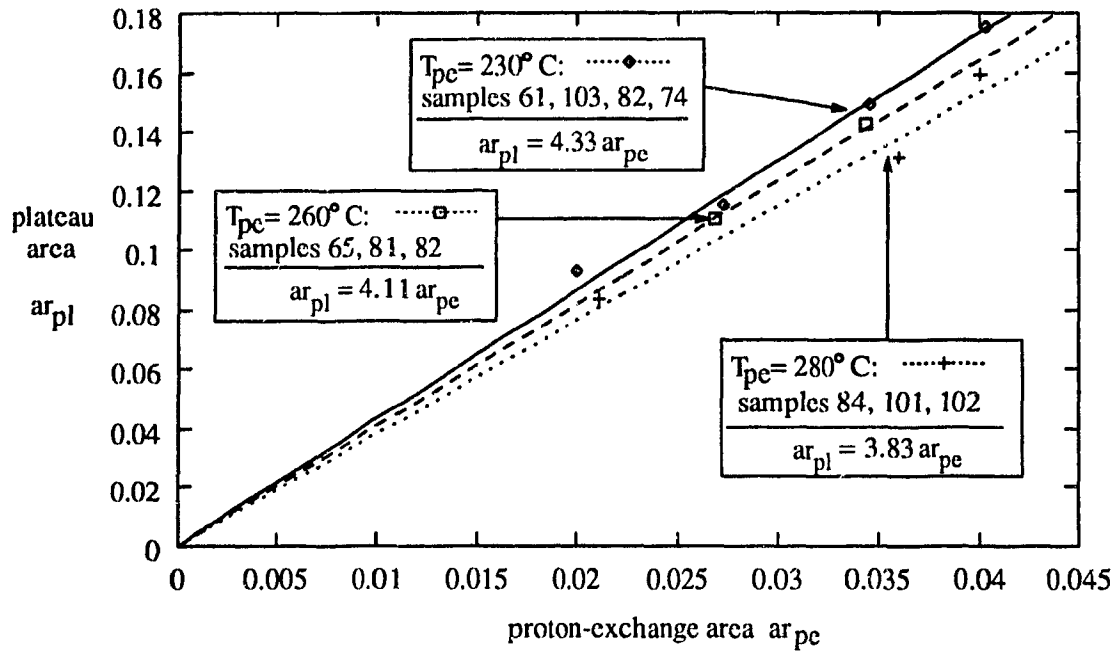

Figure 7.20: Dependence of ar_{pl} on profile area after proton-exchange

Physio-Chemical Interpretation

The proton-exchange area ar_{pe} is a measure of the total number of OH ions in the waveguide after proton-exchange. H-OH ions do not affect the refractive index, so they are not taken into account. Annealing converts H-OH ions to regular OH ions, and the plateau area ar_{pl} is a measure of the total number of OH ions after annealing. Therefore, ar_{pl} also reflects the number of H-OH ions after exchange, plus the original OH ions. By plotting ar_{pl} against ar_{pe}, the ratio between the amount of OH and H-OH ions present in the waveguide after proton-exchange is revealed. If $ar_{pl} = ar_{pe}$, then there would be no H-OH ions; if $ar_{pl} = 4ar_{pe}$, then there must be three times the number of H-OH ions than OH ions. The linear dependence of ar_{pl} on ar_{pe} indicates a constant ratio between the two ion types, with a slightly different ratio at different exchange temperatures. This result differs from that of Savatinova *et al* [61], who found the ratio of H-OH to OH ions

to increase with increased exchange time. However, Savatinova *et al* used *x*-cut $LiTaO_3$, which is much more susceptible to H-OH ions than *z*-cut substrates.

After all the H-OH ions are converted, the amount of OH ions in the waveguide remains constant. If the refractive index depends linearly on concentration, then the index profile area would remain constant upon further annealing. A non-linear dependence on concentration, on the other hand, would cause the index profile area to vary as the concentration changes during annealing. The existence of ar_{pl}, a constant value for the index profile area, implies an approximately linear index dependence on OH ion concentration.

7.4.4 Propagation Losses

The propagation losses of the fundamental mode of four waveguides (samples 84, 81, 82, 61) were measured throughout annealing, and are presented in Tables 7.10-7.12. The losses invariably decreased to low values (> 0.5dB/cm) after long anneal times, but initially increased. The initial increase may be attributed to greater intermodal coupling, since a waveguide supports more modes upon annealing. The high concentration of H-OH ions at the waveguide surface after exchange is the probable source of scattering and mode conversion losses (refer to Section 3.5.1). Annealing causes a reduction in the H-OH ion concentration. With prolonged annealing all the H-OH ions are converted into OH ions, so the source of mode conversion losses is eliminated. Thus, losses eventually decrease despite an increase in the number of guided modes. Annealing the waveguide well into the plateau area ar_{pl} clearly has beneficial effects not only for stability, but also for propagation losses.

t_a (hrs)	Δn_s	d (μm)	a	# of modes	poly. deg.	profile area	Loss (dB/cm)
sample 63 - T_a = 500°C t_{pk} = 0.25hr, n_{pk} = 0.01511, d_{pk} = 3.8 d_{pe}, ar_{pl} = 0.125							
0	0.0125	2.18	step	2	*	0.0273	*
0.25	0.01511	8.3	8	8	1	0.1181	*
0.5	0.01383	9.45	5.1	8	3	0.1201	*
0.75	0.01336	10.5	3.3	9	3	0.1258	*
2.0	0.01218	12.6	2.0	10	2	0.1360	*
sample 84 - T_a = 400°C t_{pk} = 0.33hr, n_{pk} = 0.02454, d_{pk} = 2.58 d_{pe}, ar_{pl} = 0.085							
0	0.0110	1.51	step	1	*	0.0211	0.97
0.333	0.02454	3.9	3.3	5	3	0.0859	*
0.666	0.02111	4.3	3.8	5	3	0.0833	*
1	0.01993	4.7	3.1	5	3	0.0831	1.16
2	0.01646	5.9	2.0	6	2	0.0861	0.42
4	0.01289	7.4	1.7	7	3	0.0851	0.40
8	0.01051	9.2	1.6	8	2	0.0867	*
sample 101 - T_a = 400°C t_{pk} = 0.33hr, n_{pk} = 0.02626, d_{pk} = 2.04 d_{pe}, ar_{pl} = 0.1311							
0	0.0110	2.57	step	2	*	0.0360	*
0.333	0.02626	5.25	3.5	6	4	0.1240	*
1	0.02281	6.8	3	7	3	0.1385	*
2	0.01895	7.8	3	7	3	0.1320	*
4	0.01570	9.4	3.3	9	3	0.1321	*
6	0.01403	10.6	3	9	3	0.1328	*
8	0.01220	11.6	1.7	9	1	0.1263	*
12	0.01121	13.3	1.9	11	2	0.1327	*
sample 74 - T_a = 400°C t_{pk} = 1hr, n_{pk} = 0.02660, d_{pk} = 2.18 d_{pe}, ar_{pl} = 0.175							
0	0.01220	3.3	step	2	*	0.0103	*
0.5	0.02505	6.75	5	8	5	0.1552	*
1	0.02660	7.2	3.5	9	5	0.1711	*
2	0.02278	8.55	2.7	9	3	0.1732	*
4	0.01873	10.8	2.3	11	2	0.1792	*
8	0.01576	13.1	1.8	12	2	0.1836	*
12	0.01392	13.5	1.5	12	2	0.1677	*

Table 7.10: Detailed annealing data. * indicates values not measured/available.

t_a (hrs)	Δn_s	d (μm)	a	# of modes	poly. deg.	profile area	Loss (dB/cm)
sample 65 - T_a = 350°C, wet O_2 atmosphere t_{pk} = 2hrs, n_{pk} = 0.02534, d_{pk} = 2.19 d_{pc}, ar_{pl} = 0.110							
0	0.0128	2.1	step	2	*	0.0270	*
1	0.02437	4.0	7	4	3	0.0912	*
2	0.02531	4.6	4.7	5	3	0.1070	*
4	0.02270	5.4	4.2	6	3	0.1111	*
6	0.01966	6.0	4.2	7	3	0.1072	*
8	0.01912	6.45	3.5	7	3	0.1110	*
12	0.01805	7.0	2.4	8	3	0.1120	*
sample 81 - T_a = 350°C t_{pk} = 2hrs, n_{pk} = 0.0250, d_{pk} = 2.15 d_{pc}, ar_{pl} = 0.112							
0	0.0128	2.68	step	2	*	0.0313	1.1
1	0.02416	5.05	6	6	5	0.1132	1.3
2	0.02500	5.75	5	7	5	0.1320	*
4	0.02471	6.5	3.5	8	3	0.1115	*
6	0.02232	7.2	3.5	9	4	0.1116	0.3
8	0.02055	7.6	3.7	9	4	0.1110	*
12	0.01903	8.13	3.4	9	4	0.1390	0.31
sample 82 - T_a = 350°C t_{pk} = 4hrs, n_{pk} = 0.0251, d_{pk} = 2.36 d_{pc}, ar_{pl} = 0.1486							
0	0.0122	2.83	step	2	*	0.0315	0.97
1	0.0235	5.25	6.2	6	7	0.1147	*
2	0.0245	5.85	6	7	4	0.1330	1.16
4	0.02510	6.67	3.85	8	3	0.1511	*
6	0.02311	7.2	3.4	9	4	0.1195	0.42
8	0.02117	7.8	3.6	9	4	0.1188	*
12	0.01887	8.52	3.5	9	4	0.1147	0.40
sample 102 - T_a = 350°C t_{pk} = 4hrs, n_{pk} = 0.02511, d_{pk} = 2.38 d_{pc}, ar_{pl} = 0.159							
0	0.0140	2.86	step	2	*	0.01001	*
0.333	*	*	*	1	2	*	*
0.666	0.02036	*	*	1	3	*	*
2	0.02368	6.1	6.2	7	3	0.1312	*
4	0.02544	6.8	5	8	3	0.1588	*
6	0.02447	7.3	4	8	3	0.1619	*
8	0.02251	7.8	3.6	8	3	0.1582	*
12	0.02041	8.6	3.5	9	4	0.1579	*
16	0.01906	9.2	3.3	9	4	0.1573	*

Table 7.11: Detailed annealing data. * indicates values not measured/available.

t_a (hrs)	Δn_s	d (μm)	a	# of modes	poly. deg.	profile area	Loss (dB/cm)
sample 61 - T_a = 300°C t_{pk} = 12hrs, n_{pk} = 0.0260, d_{pk} = 2.4 d_{pe}, ar_{pl} = 0.093							
0	0.0122	1.64	step	1	*	0.0200	0.73
2	0.02343	2.9	10	3	2	0.0646	0.89
4	0.02428	3.2	10	3	2	0.0739	0.69
6	0.02434	3.55	8	4	3	0.0814	0.61
8	0.02495	3.7	7	4	3	0.0861	0.44
12	0.0260	3.95	4.5	5	5	0.0931	*
sample 93 - T_a = 300°C t_{pk} = 16hrs, n_{pk} = 0.0265, d_{pk} = 2.3 d_{pe}, ar_{pl} = 0.101							
0	0.0125	1.74	step	1	*	0.0218	*
1	*	*	*	1	*	*	*
2	0.0237	2.95	9	3	2	0.0662	*
4	0.0250	3.25	9	3	2	0.0769	*
6	0.02556	3.4	7	4	3	0.0813	*
8	0.02599	3.6	6.5	4	3	0.0872	*
12	0.02634	3.8	5.5	4	3	0.0919	*
16	0.0265	4.0	5	5	5	0.0973	*
30	0.02502	4.85	5	6	3	0.1113	*
sample 103 - T_a = 300°C t_{pk} = 16hrs, n_{pk} = 0.02579, d_{pk} = 2.15 d_{pe}, ar_{pl} = 0.112							
0	0.0122	2.23	step	2	-	0.0272	*
2	*	*	*	3	*	*	*
4	0.02365	3.95	8	4	3	0.088	*
6	0.0240	4.2	7	5	5	0.0913	*
8	0.025	4.45	7	5	4	0.1011	*
16	0.02579	4.8	4	6	3	0.1122	*

Table 7.12: Detailed annealing data. * indicates values not measured/available.

7.4.5 Annealing of Buffered Waveguides

The aim in this section was merely to observe general trends for buffered waveguides, and compare against unbuffered waveguides. No attempt was made to gather extensive data, as was done for unbuffered waveguides. Index instabilities still plagued buffered $LiTaO_3$ waveguides, and since H-OH ions are the likely cause of these instabilities, it is concluded that H-OH ions are still present in the waveguiding layer. The reduced Δn_e means that the concentration of OH ions is lower, which would imply that the concentra-

tion of H-OH ions is also lowered. If less H-OH ions are present, then less can be converted into OH ions. Thus, one would expect the surface index and depth of buffered waveguides to increase during annealing, but not as much as unbuffered waveguides. It is likely that the greater the degree of buffering, the less the increase in n_s and d.

Four buffered waveguides were annealed (samples 112, 54, 111, and 75). Of the four, three were exchanged at the same temperature and time, but with 2%, 4% and 6% buffering (samples 112, 54, and 111 respectively). Their d_{pe} were about the same and their Δn_e were marginally different (0.0117, 0.0115, 0.0113) (see Table 7.6). The purpose was to observe the effect of the amount of buffering on the index profile during annealing. Surprisingly, the profiles of all three waveguides were identical throughout annealing. This means that their Δd, Δn_s, and profile area curves were all the same, as were their annealing parameters b, c, e, f, and g. Thus, the amount of H-OH ions in all three waveguides was the same, and the degree of buffering had very little or no effect on the index profile.

sample	d_{pe}	b	c	Δn_{pk}	e	f	g	ar_{pl}	t_{pk}
buf. 111, 112, 54	2.7	1.9	0.35	0.025	0.0122	0.12	-	0.128	2 hrs
pure melt 81	2.68	2.35	0.355	0.025	0.01125	0.12	-0.115	0.142	2 hrs

Table 7.13: Annealing parameters of buffered vs. unbuffered waveguides

Table 7.13 compares annealing parameters for samples 112, 54, and 111 against those of sample 81, which was exchanged in a pure melt but otherwise has the same d_{pe} and was also annealed at $T_a = 350°C$. The parameter c is the same for both, in accordance with the earlier finding that c is constant for all waveguides annealed at the same T_a. For the buffered waveguide, b is noticeably lower, indicating that the increase in depth is much less (see Fig. 7.21 and equation 7.5). Contrary to expectation, the index peak Δn_{pk} remained the same and occured at $t_{pk} = 2$ hrs for both. However, Δn_s decreased in a linear fashion after the peak (see Fig. 7.22), and remained slightly higher for the buffered waveguide.

The plateau area ar_{pl} was, as expected, lower, confirming the hypothesis that there are less H-OH ions in the buffered waveguide than in the unbuffered one.

It is difficult to draw conclusions from such scant data. For the same anneal time, the depth d of a buffered waveguide will definitely be lower than that of an unbuffered one, and Δn_s will likely be higher (compared to unbuffered waveguides of the same d_{pe}). For the same Δn_s, therefore, the buffered waveguide will have a smaller depth d. For example, at t_a = 2hrs, $\Delta n_s = 0.025$ for both, but $\Delta d = 2.4\mu m$ ($d = 5.1\mu m$) for sample 111 and $\Delta d = 3.07\mu m$ ($d = 5.75\mu m$) for sample 81 (see Table 7.14). In terms of tailoring the index profile for design requirements, the use of buffered waveguides would lead to combinations of Δn_s and d values which may not be possible with unbuffered waveguides. Further investigation in this area should prove worthwhile.

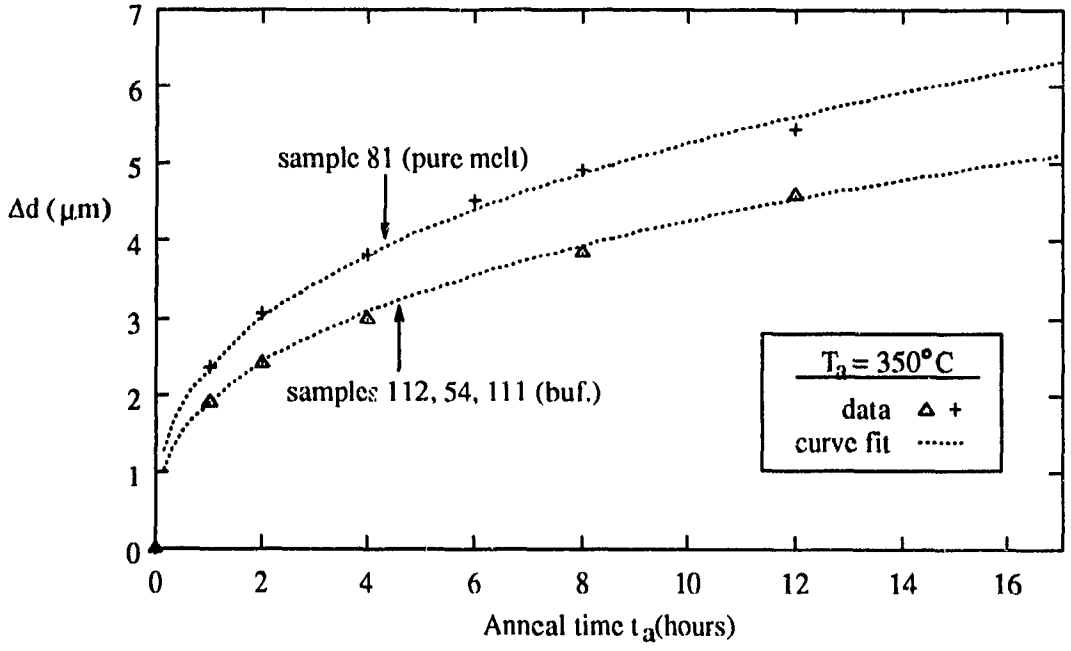

Figure 7.21: Comparing Δd curves for buffered and unbuffered waveguides

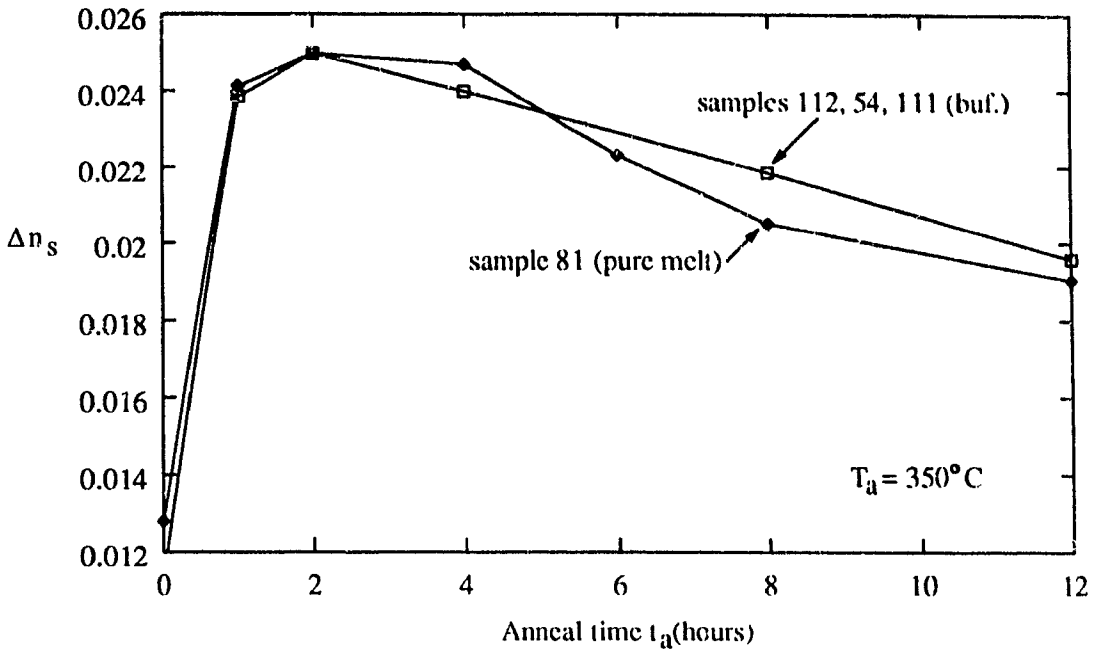

Figure 7.22: Comparing Δn_s curves for buffered and unbuffered waveguides

t_a (hrs)	Δn_s	d (μm)	a	# of modes	poly. deg.	profile area
samples 112,54,111 (6%) - T_a = 350°C $b = 1.9$, $c = 0.35$, $\epsilon = 0.0122$, $f = 0.12$ t_{pk} = 2hrs, $n_{pk} = 0.0250$, $d_{pk} = 1.89\ d_{pc}$, $ar_{pl} = 0.128$						
0	0.0115	2.7	step	2	-	0.0311
1	0.02387	4.6	6	5	3	0.1019
2	0.0250	5.1	6	6	4	0.1183
4	0.0210	5.7	4	7	3,1	0.1240
8	0.02187	6.6	4	8	3	0.1308
12	0.01962	7.3	3.8	8	4	0.1294
sample 75 (2%) - T_a = 350°C $b = 2.51$, $c = 0.35$, $\epsilon = 0.009$, $f = 0.20$ t_{pk} = 16hrs, $n_{pk} = 0.02521$, $d_{pk} = 2.86\ d_{pc}$, $ar_{pl} = 0.235$						
0	0.01337	3.7	step	2	-	0.0195
1	0.01886	6.3	6.8	6	3	0.1110
2	0.02016	6.8	7.1	6	3	0.1286
4	0.02203	7.8	6	8	3	0.1591
6	0.02244	8.1	5	9	3	0.1731
8	0.02353	8.6	5	9	3	0.1858
12	0.02508	9.7	4.5	11	3	0.2220
16	0.02524	10.3	4	12	3	0.2356

Table 7.14: Annealing data for buffered waveguides

7.5 Waveguide Design and Fabrication with Proton-Exchange and Annealing Data

In this section, it will be demonstrated how the characterization data and the empirically derived formulas of the previous sections (except Section 7.4.5, since the data for buffered waveguides is not extensive enough) can be put to use in a waveguide design and fabrication process. Our goal is to be able to select the conditions (i.e. T_{pe}, t_{pe}, T_a, and t_a) required to fabricate a waveguide with the desired refractive index profile, specified by Δn_s, d, and a.

7.5.1 Design Curves

A waveguide, if its modal indices are not stable, will drift away from its originally designed parameters and cease to be useful. The first criterion that any waveguide must meet is that of stability. In Section 7.4.3, a condition for obtaining stable waveguides was established: the waveguide must be annealed past the surface index peak and into the plateau area region ($t_a \geq t_{pk}$). This requirement will limit the range of possible d, Δn_s, and a values. The stability condition $t_a \geq t_{pk}$ can be translated into the following constraints by the results of Section 7.1.2:

$$d \geq d_{pk} \quad or \quad d \geq 2.27 d_{pe} \tag{7.15}$$

$$\Delta n_s \text{ is past } \Delta n_{pk} \quad or \quad \Delta n_s \leq 0.02566 \tag{7.16}$$

$$a \text{ is past } a_{pk} \quad or \quad a \leq 5 \tag{7.17}$$

where d_{pk}, Δn_{pk}, and a_{pk} are the values of d, Δn_s, and a, respectively, at the surface index peak (at time t_{pk}). In Section 7.4.2, it was noted that for all waveguides, d_{pk} averaged 2.27 d_{pe}, and Δn_{pk} averaged 0.02566. By examining Table 7.10, one will note that a is always less than or equal to 5 at t_{pk}. The average a_{pk} is 3.43 for T_a = 400°C, 4.64 for T_a = 350°C, and 4.5 for T_a = 300°C.

The empirically derived relations of the previous sections can be manipulated to provide us with an equation which will guide our selection of fabrication conditions. The waveguide depth as a function of anneal time is given by equation 7.5. The surface index increase as a function of anneal time is given by two equations: 7.10 for before the index peak, and 7.11 for after the peak. Since we are interested in stable waveguides for which $t_a > t_{pk}$, equation 7.11 is the applicable equation. Therefore, we have

$$\Delta d = d - d_{pe} = b\, t_a^c \tag{7.18}$$

$$\Delta n_s = \Delta n_{pk}(t_a - t_{pk} + 1)^q \tag{7.19}$$

By rearranging equation 7.18 we obtain

$$t_a = \left[\frac{d - d_{pe}}{b}\right]^{\frac{1}{c}} \tag{7.20}$$

Note that at the surface index peak t_{pk}, equation 7.20 still applies, i.e.:

$$t_{pk} = \left[\frac{d_{pk} - d_{pe}}{b}\right]^{\frac{1}{c}} \tag{7.21}$$

Earlier in Section 7.4.2, it was observed that d_{pk} occurs at an average of $d_{pk}/d_{pe} = 2.27$. Using this relation together with equation 7.21, we arrive at an expression for t_{pk} in terms of d_{pe}:

$$t_{pk} = \left[\frac{1.27 d_{pe}}{b}\right]^{\frac{1}{c}} \tag{7.22}$$

Now, by substituting equations 7.20 and 7.22 into 7.19; we arrive at the following:

$$\Delta n_s = \Delta n_{pk}\left(\left[\frac{d - d_{pe}}{b}\right]^{\frac{1}{c}} - \left[\frac{1.27 d_{pe}}{b}\right]^{\frac{1}{c}} + 1\right)^q \tag{7.23}$$

where $b = 0.47 d_{pe} + 1.075,\ q = 0.010 d_{pe} - 0.23, c = 0.35$ for $T_a = 350$ °C

$b = 0.47 d_{pe} + 2.7,\ q = 0.086 d_{pe} - 0.55, c = 0.10$ for $T_a = 400$ °C

and $\Delta n_{pk} = 0.02566$

In equation 7.23, c and Δn_{pk} are constants, and b and g are functions of d_{pe}. Therefore, Δn_s is a function of two variables only, d and d_{pe}. A curve may be plotted, relating Δn_s (y-axis, the dependent variable) to d (x-axis, the independent variable) by holding d_{pe} constant. In Figures 7.23 and 7.24, such curves are plotted for various values of d_{pe}, at T_a = 350°C and T_a = 400°C, respectively. Each curve represents a waveguide of a certain d_{pe}, and shows how that waveguide's index profile parameters (Δn_s and d) will evolve during annealing. At the start of each curve (near the top of each figure), $a \approx a_{pk}$ since this is close to the index peak; as d increases, a will decrease. Unfortunately, the behaviour of a could not be quantified. A thick curve in each figure is plotted for d_{pe} = 0, which represents the limiting values of possible (Δn_s, d) combinations. For example, it is not possible to produce a waveguide of $d = 2\mu m$ and Δn_s = 0.01 (see both Figures 7.23 and 7.24). Of course, without the minimum anneal time requirement, such a waveguide could be fabricated, but index instabilities would be present.

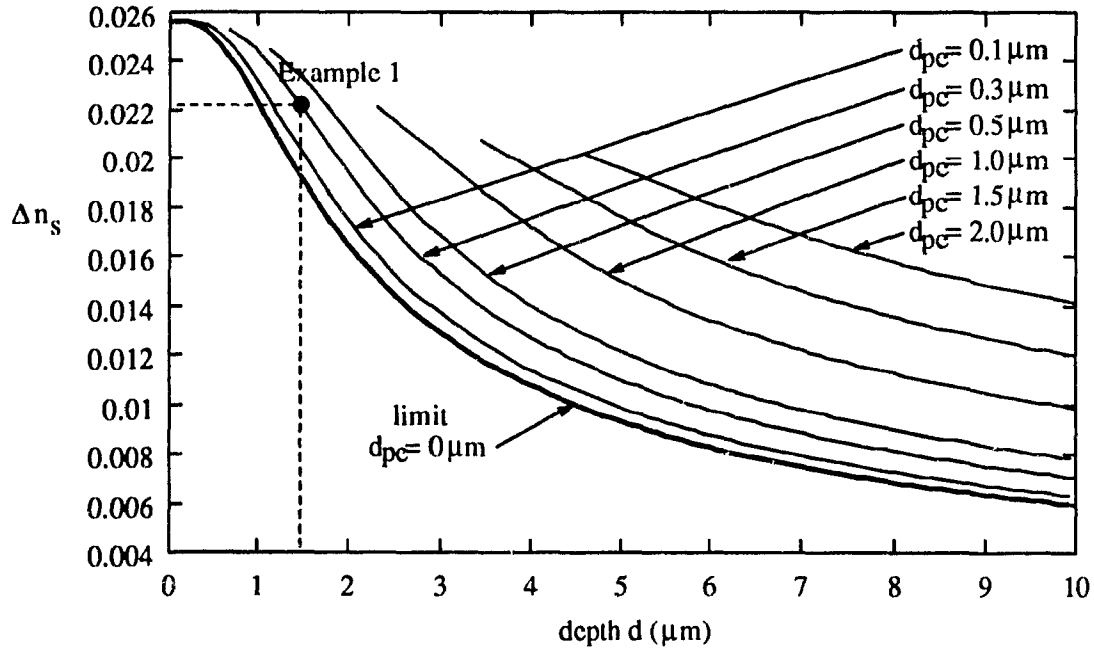

Figure 7.23: Design curve for T_a = 350°C: possible values of d and Δn_s

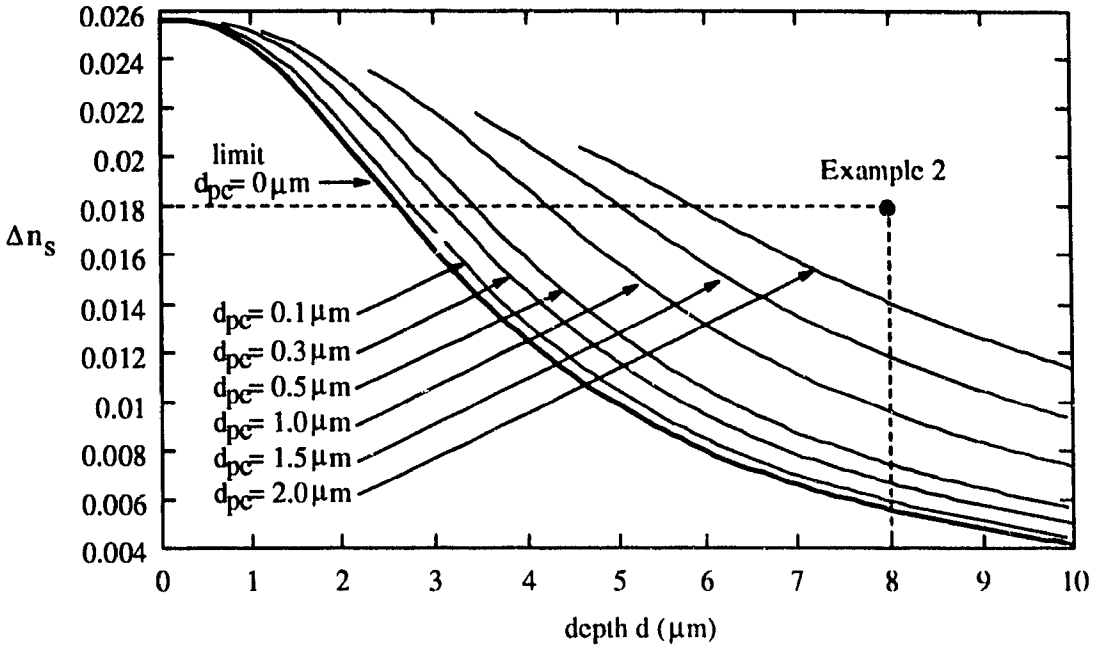

Figure 7.24: Design curve for $T_a = 400°C$: possible values of d and Δn_s

7.5.2 Design Examples

Let us now consider specific design examples using these curves and equations.

Example 1: We wish to design a strongly guiding (i.e. large Δn_s), shallow waveguide. Let us chose $T_a = 350°C$ and use Figure 7.23. We shall pick $d_{pe} = 0.3\mu m$, and a point on this curve that suits our requirements is $d = 1.5\mu m$, $\Delta n_s = 0.0221$. An estimate for the shape parameter a (equation 6.2) would be $a \approx 2$. At $d/d_{pe} = 5$, this point is neither close to the index peak (where the a_{pk}(average) = 4.6) nor too far from it. Having chosen d and d_{pe}, we use equation 7.20 to find the anneal time t_a: $t_a = [(d - d_{pe})/b]^{1/c} = [(1.5 - 0.3)/(0.47 * 0.3 + 1.075)]^{1/0.35} = 0.963hr$. Therefore, the annealing conditions are $T_a = 350°C$, $t_a =$ 0.963hr. For the proton-exchange conditions, we have the freedom to chose either T_{pe} or t_{pe} since only d_{pe} is fixed. Let us then extrapolate from the proton-exchange data and use $T_{pe} = 200°C$, a temperature for which no measured data is available. With equation 7.2, the effective diffusion coefficient D_e can be calculated: $D_e = D_0 exp(-E_a/[kT_{pe}])$, where

E_a and D_0 are parameters found in Table 7.2, and k is Boltzmann's constant. Thus, $D_e = 1.195 \times 10^8 exp(-0.9101/[8.583 \times 10^{-5} \times (200 + 273)]) = 0.02196$. Now we rearrange equation 7.1 to find t_{pe}: $t_{pe} = d_{pe}^2/[4 \times D_e] = 0.3^2/[4 \times 0.02196] = 1.02 hrs$. Therefore, the fabrication conditions are: t_{pe} = 1.02hrs, T_{pe} = 200°C, t_a = 0.963hr, T_a = 350°C.

Example 2: For this example, we have specific requirements for the index profile: $d = 8\mu m$, and $\Delta n_s = 0.018$. This time we shall use T_a = 400 °C, and equation 7.23 instead of Fig. 7.24. Substituting the values of d and Δn_s into equation 7.23 gives us an equation in which d_{pe} is the sole variable and which can be solved by a root searching technique [96]. Solving this equation results in $d_{pe} = 2.17\mu m$. With this information, t_a can be found in the same way as demonstrated in the previous example (using equation 7.20); doing so gives t_a = 2.46hrs. Note that the index profile parameters of sample 101 is close to that of this example: for sample 101, $d_{pe} = 2.57\mu m$, and after 2 hours of annealing, $d = 7.8\mu m$ and $\Delta n_s = 0.01895$ (see Table 7.10). Numerical calculations based on the empirical formulas do seem to model reality fairly well. For proton-exchange, let us fix t_{pe} at 1.5hrs and solve for T_{pe}. From equation 7.1, $D_e = d_{pe}^2/[4 \times t_{pe}] = 2.47^2/[4 \times 1.5] = 1.0168$. By manipulating equation 7.2, T_{pe} can be found in terms of D_e: $T_{pe} = -E_a/[k \times ln(D_e/D_0)] = -0.9101/[8.583 \times 10^{-5} ln(1.0168/1.195 \times 10^8)] = 297.6$°C. Therefore, the fabrication conditions for this waveguide are: T_a = 400°C, t_a = 2.46hrs, T_{pe} = 297.6°C, t_{pe} = 1.5hrs.

Chapter 8

Summary and Conclusion

Z-cut $LiTaO_3$ waveguides were fabricated by proton-exchange and buffered exchange in pyrophosphoric acid, followed by annealing. The waveguides' refractive index profile parameters were related to the fabrication conditions. The goal is to be able to accurately predict the proper proton-exchange and annealing conditions for a waveguide with specific design requirements. This has been the primary objective of this research, and the results show that the objective has been largely fulfilled.

The step-index profile model was found to be accurate for waveguides proton-exchanged in pyrophosphoric acid. The index increase Δn_e, the proton-exchanged depth d_{pe}, the effective diffusion coefficient D_e, the propagation loss α, the minimum exchange temperature, and the constants D_0 and E_a were obtained. Simple equations relating d_{pe} to the exchange time t_{pe} and D_e (equation 7.1), D_e to the exchange temperature T_{pe} (equation 7.2), and Δn_e to T_{pe} (equation 7.3) were found. These equations and parameters will prove invaluable when designing and fabricating waveguides. The waveguide's modal indices were found to fluctuate after exchange (i.e. index instabilities). The unexpected temperature dependence of Δn_e is explained by the annealing effect during proton-exchange. The advantage of using pyrophosphoric acid instead of benzoic acid is that waveguides can be fabricated faster.

Annealing caused the waveguide's index profile to smooth out, the depth to increase, and the surface index to initially increase but later decrease. Annealing proved to be

a versatile tool for tailoring the index profile to a wide range of heights, depths, and to a lesser degree, shapes. The generalized Gaussian function was found to model the index profile quite well, from very step-like to very smooth profiles. Propagation losses decreased for prolonged annealing. Empirical equations relating the depth increase Δd to the anneal time t_a (equation 7.5) and the surface index increase Δn_s to t_a (equations 7.10 and 7.11) were found. The parameters in these equations showed dependence upon the initial exchange conditions, and further empirical equations relating the parameters to the exchange conditions (equations 7.6-7.9, 7.12-7.13) were also found. These equations and parameters will prove invaluable when designing and fabricating waveguides. By plotting the area of the index profile versus anneal time, a minimum anneal time requirement for eliminating index instabilities (equation 7.14) was discovered. The profile area attains a stable value ar_{pl}, and this figure can be used as an indicator of the ration of H-OH ions to OH ions in the waveguide. Examples of how to use the empirical equations and the data accumulated in the proton-exchange and annealing sections to predict fabrication conditions were given.

Buffering the acid during exchange reduced Δn_e, but did not affect the profile shape, the waveguide depth, or the propagation losses. Index instabilites were present despite the buffering. The degree of buffering had a small effect on Δn_e, and this effect was more pronounced at lower exchange temperatures. An equation relating Δn_e to T_{pe} (equation 7.4) was found. Upon annealing, the Δd and Δn_s vs. t_a curves were different from those of waveguides with the same d_{pe} proton-exchanged in pure melts. This result leads to the possibility of fabricating waveguides with index profiles that cannot be normally achieved employing pure melts. Further investigation, though, is necessary before the annealing behaviour of buffered waveguides becomes predictable.

A mathematical model of annealing in $LiTaO_3$ was developed, and a numerical simulation was attempted (see Appendix A). The results from this preliminary effort were encouraging. However, further work is necessary to improve and refine the model.

Appendix A

Mathematical Modelling and Simulation of Annealing in $LiTaO_3$

A.1 Mathematical Modeling

The diffusion and conversion processes that comprise the annealing process (refer to Section 4.4) can be modeled by differential equations. The following describes how each process is modeled.

Diffusion of OH and H-OH ions

To model annealing in $LiTaO_3$, we use the same equation that is used to model annealing in $LiNbO_3$ (Ficke's Law - refer to Section 4.3):

$$\frac{\partial C_{OH}(z,t)}{\partial t} = \frac{\partial}{\partial z}\left(D_{OH}\frac{\partial C_{OH}(z,t)}{\partial z}\right) \tag{A.1}$$

where $C_{OH}(z,t)$ is the OH ion concentration profile as a function of time, and D_{OH} the diffusion coefficient ($\mu m^2/hr$) for annealing. D_{OH} may be a constant or a function of concentration. This equation can also be used to model H-OH ion diffusion. The variables $C_{HOH}(z,t)$ and D_{HOH} are then used to represent the H-OH ion concentration profile and diffusion coefficient, respectively.

H-OH to OH ion conversion

The H-OH to OH ion conversion during annealing in $LiTaO_3$ couples the H-OH and OH concentration profiles in a way that renders the annealing process much more difficult to model for $LiTaO_3$ than $LiNbO_3$. The difficulty of modelling the conversion process lies in establishing the rate of conversion. Although little is known about the conversion process, it is hypothesized that the rate depends on these factors:

- the concentration of H-OH ions C_{HOH}
- the concentration of regular OH ions C_{OH}
- the anneal temperature T_a

Intuitively, one expects the conversion rate to be high for **a)** a high H-OH ion concentration, **b)** a low OH ion concentration, and **c)** a high anneal temperature. One possible formulation for the rate of conversion that behaves accordingly is

$$\frac{\partial C_{HOH}(z,t)}{\partial t} = -\frac{\partial C_{OH}(z,t)}{\partial t} = p_1 \frac{C_{HOH}(z,t)}{p_2 C_{OH}(z,t) + 1} \tag{A.2}$$

where p_1, p_2 are constants, and likely depend on T_a. The 1 in the denominator prevents the rate from escalating to infinity when $C_{OH} = 0$. Many formulations are possible and several were tested to see which produced the best results.

The Nonlinear Index Dependence on Concentration

Once the annealing is finished, the hydrogen concentration profile can be translated into an index profile by an index function $n(C_{OH})$. The index function for $LiTaO_3$ has yet to be found, so for the sake of simplicity, a linear index function (i.e. $n = kC_{OH}$) was used for this simulation.

A.2 Numerical Methods

A finite difference method can be used to solve the nonlinear partial differential equations of the previous section. The basic concept is simple and well-suited to implementation on a computer. The continuous concentration function $C(z,t)$ is discretized by sampling it at regular intervals in z and t (i.e. Δz, Δt). Thus $C(z,t)$ is replaced by C_i^n:

$$C_i^n = C(z_i, t_n) \qquad (z_i = i\Delta z, t_n = n\Delta t) \tag{A.3}$$

where i, n are integers. The smaller Δz and Δt are, the better the resolution and the more accurate the solution, but the longer the computing time. The partial derivatives of the diffusion equations can now be replaced with finite differences [100]. At a certain point z_i, the derivative may be approximated in one of three ways (see Fig. A.1):

$$\left.\frac{\partial C}{\partial z}\right|_{z_i} = \begin{cases} \frac{C_{i+1}-C_i}{\Delta z} & \text{forward difference method} \\ \frac{C_i-C_{i-1}}{\Delta z} & \text{backward difference method} \\ \frac{C_{i+1}-C_{i-1}}{2\Delta z} & \text{central difference method} \end{cases} \tag{A.4}$$

The forward difference method is so named because data from z_{i+1} is used to evaluate the derivate at z_i; the two other methods also derive their names in the same fashion. The central difference method is the most accurate because it uses the points on either side of z_i, so the estimated slope will be nearly parallel to the actual slope at z_i.

Second order derivatives may be evaluated by applying the central difference method twice, but using a half interval instead:

$$\begin{aligned} \left.\frac{\partial^2 C}{\partial z^2}\right|_{z_i} &= \frac{1}{\Delta z}\left(\left.\frac{\partial C}{\partial z}\right|_{z_{i+1/2}} - \left.\frac{\partial C}{\partial z}\right|_{z_{i-1/2}}\right) \\ &= \frac{1}{\Delta z}\left(\frac{C_{i+1}-C_i}{\Delta z} - \frac{C_i - C_{i-1}}{\Delta z}\right) \\ &= \frac{1}{\Delta z^2}(C_{i+1} - 2C_i + C_{i-1}) \end{aligned} \tag{A.5}$$

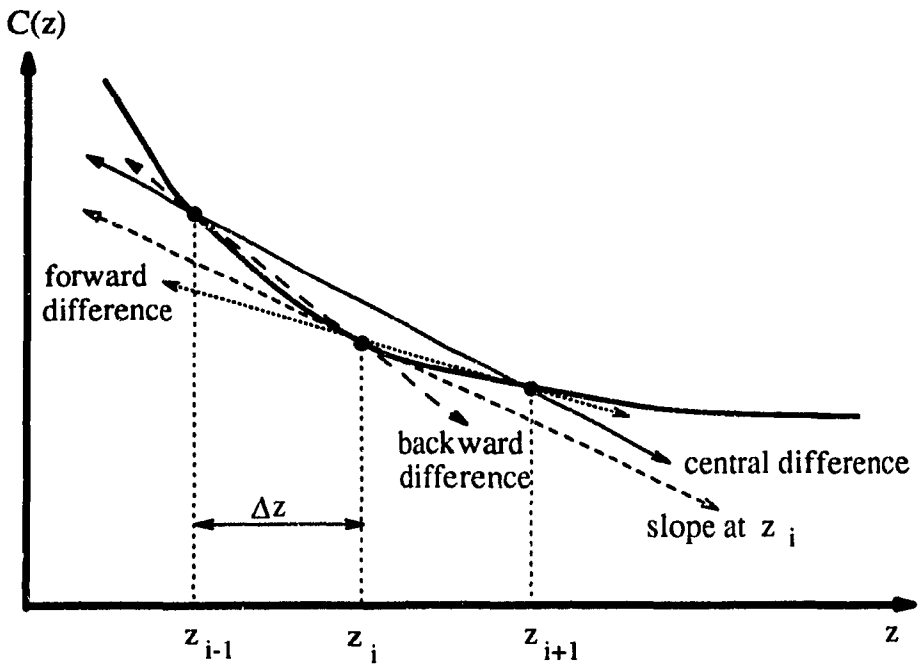

Figure A.1: Finite difference estimable of the slope

To solve Ficke's law for a constant diffusion coefficient, we combine a central difference method for z with a forward difference method for t:

$$\frac{\partial C}{\partial t} = D\frac{\partial^2 C}{\partial z^2}$$

$$\frac{C_i^{n+1} - C_i^n}{\Delta t} = \frac{D}{\Delta z^2}(C_{i+1}^n - 2C_i^n + C_{i-1}^n)$$

$$C_i^{n+1} = C_i^n + rD(C_{i+1}^n - 2C_i^n + C_{i-1}^n) \qquad \text{(A.6)}$$

$$\text{where } r = \frac{\Delta t}{\Delta z^2} \qquad \text{(A.7)}$$

A problem arises at the boundary, where $i = 0$. What is the value for C_{-1}^n? Let us imagine that C_i^n extends for both positive and negative i and is symmetric about $i = 0$. By the principle of symmetry we can see that diffusion would proceed in the same manner in this case as for a function which extends in the positive direction only. Hence we can take $C_{-1}^n = C_1^n$ (this is the same result as that obtained by applying the Neumann boundary

condition). Thus, for $i = 0$,

$$C_0^{n+1} = C_0^n + 2rD(C_1^n - C_0^n) \tag{A.8}$$

To solve Ficke's law for a concentration dependent diffusion coefficient, we adopt a similar approach:

$$\begin{aligned}
\frac{\partial C}{\partial t} &= \frac{\partial}{\partial z}\left(D(C)\frac{\partial C}{\partial z}\right) \\
\frac{C_i^{n+1} - C_i^n}{\Delta t} &= \frac{1}{\Delta z}\left(D(C_{i+1/2}^n)\left.\frac{\partial C}{\partial z}\right|_{i+1/2} - D(C_{i-1/2}^n)\left.\frac{\partial C}{\partial z}\right|_{i-1/2}\right) \\
C_i^{n+1} - C_i^n &= \frac{\Delta t}{\Delta z}\left(D(C_{i+1/2}^n)\frac{C_{i+1}^n - C_i^n}{\Delta z} - D(C_{i-1/2}^n)\frac{C_i^n - C_{i-1}^n}{\Delta z}\right) \\
C_i^{n+1} &= C_i^n + r\left(D(C_{i+1/2}^n)C_{i+1}^n - [D(C_{i+1/2}^n) + D(C_{i-1/2}^n)]C_i^n + D(C_{i-1/2}^n)C_{i-1}^n\right)
\end{aligned} \tag{A.9}$$

Here, $C_{i-1/2}^n$ may be interpolated by $(C_i^n + C_{i-1}^n)/2$, and $C_{i+1/2}^n$ by $(C_i^n + C_{i+1}^n)/2$. Once again, at the boundary $i = 0$, the principle of symmetry yields

$$C_0^{n+1} = C_0^n + 2rD(C_{1/2}^n)(C_1^n - C_0^n) \tag{A.10}$$

A.3 A Computer Simulation

The computer simulation models three concurrent processes: the diffusion of OH ions, the diffusion of H-OH ions, and the conversion of H-OH ions into OH ions. The simulation works with the following variables and constants:

- $C_{OH}(z,t)$: the normalized concentration of OH ions as a function of time t and depth z (i.e. the OH ion concentration profile)
- $C_{HOH}(z,t)$: the normalized concentration of H-OH ions as a function of time t and depth z (i.e. the HOH ion concentration profile)
- D_{OH}: diffusion coefficient for OH ions (μm^2/hr)

- D_{HOH}: diffusion coefficient for H-OH ions (μm^2/hr)
- q_1, q_2: constants for a concentration dependent diffusion coefficient function $D_{OH}(C_{OH})$
- p_1, p_2: constants in the H-OH to OH ion conversion rate equation

Using the finite difference method, the partial differential equations of diffusion and conversion are applied in incremental, discrete steps of Δz and Δt. When annealing is finished, an index function $n(C_{OH})$ translates the OH concentration profile to an index profile. Figure A.2 depicts the algorithm of the simulation.

The IWKB profiles of sample 81 (d_{pc} = 2.68μm, Δn_e = 0.0128, T_a = 350°C) were used as the basis of comparison for the simulated profiles. Depending on how well the simulated profiles match the measured profiles, the constants or even the equations in the model are revised. The simulation is repeated until the closest match possible between the simulated results and the profiles of sample 81 is achieved.

Initial conditions

The OH ion concentration profile was initialized as a step function with a depth of 2.68μm and a normalized concentration of 1 (which translates into an index of 0.0128 through the index function), in accordance with the proton-exchanged conditions of sample 81. The H-OH ion concentration profile may be initialized in a number of ways. It has yet to be measured experimentally, and the relevant information is scant and seemingly contradictory:

- After annealing, the index profile area grows to about four times the proton-exchanged area (see section 7.4.3). Further results from section 7.4.3 suggest that the index function $n(C_{OH})$ is roughly linear, so this data suggests the presence of three times more H-OH ions than OH ions.

- Infra-red spectroscopy measurements also suggest that a greater abundance of H-OH ions than OH ions [64].
- HOH ions occupy only a thin surface layer, while OH ions extend to the proton-exchanged depth [64]. Thus the H-OH ion concentration must be very high if H-OH ions exist in greater abundance than OH ions.
- Hydrogen concentration at surface is 1.15 times the bulk Li concentration [67].

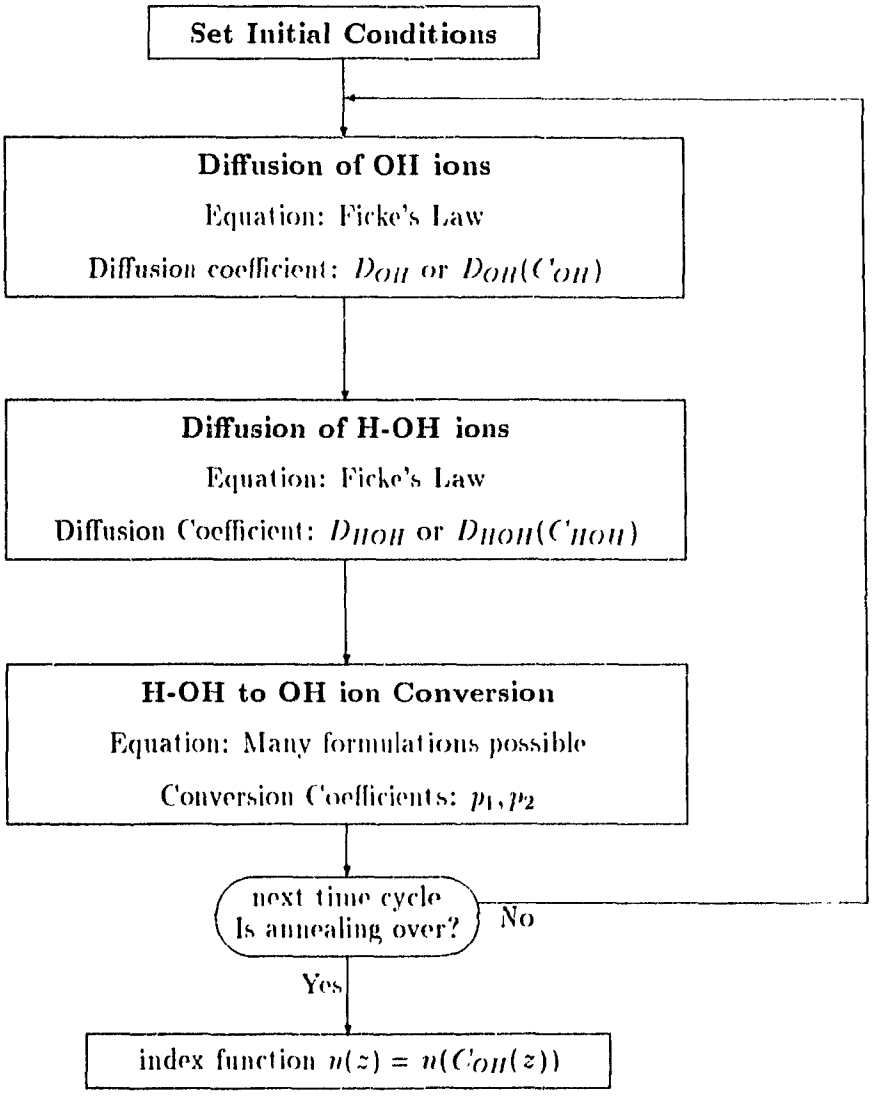

Figure A.2: Algorithm of Computer Simulation

If H-OH ions are confined to a thin surface layer (0.2-0.3 μm), and they do outnumber OH ions by a factor of three, then the H-OH ion concentration in that surface layer would have to be over twenty times greater than the OH ion concentration. This is unrealistically high, and much greater than 1.15 times the bulk Li concentration. In order to have a ratio of three between H-OH and OH ions, the H-OH ions must extend deep into the waveguide, as deep as the proton-exchanged depth, at three times the concentration of OH ions. Thus it is not possible for an initial H-OH ion concentration profile to satisfy all the conditions. Two alternatives, each of which satisfy one condition but not the other, are considered:

1. H-OH ions exist only near the surface, but not at a high enough concentration for the total to outnumber OH ions.

2. H-OH ions exist throughout the waveguide, and the total number of H-OH ions is greater than the number of OH ions by a factor of three.

In either case, the H-OH concentration profile was taken as a step function for the sake of simplicity. Both alternatives were tested: the first produced simulated profiles which were highly implausible; the second produced plausible profiles and a Δn_s versus t_a curve which matched with that of sample 81. Therefore, the second alternative was used.

OH ion diffusion

With a constant diffusion coefficient D_{OH}, the simulated index profile became smooth and graded very quickly. The IWKB profiles of sample 81 remain step-like for some time, and becomes smooth and graded only after Δn_s has begun to decline. A concentration dependent $D_{OH}(C_{OH})$ was required to produce more step-like profiles. Several "simple" functions for $D_{OH}(C_{OH})$ were tested. A simple function, in this case, is loosely defined as a function with a small number of constants and whose slope is either monotonically increasing or decreasing. Lines and exponential curves are examples of simple functions.

More complex functions, such as those with discontinuities (representing changing diffusivities in different phases of the $H_x Li_{1-x} TaO_3$ compound), require more constants in their expression. The greater the number of constants and parameters, the more complicated and unwieldy the annealing model becomes, so complex equations and functions were avoided where possible. The following exponential function was found to give reasonably step-like profiles:

$$D_{OH}(C'_{OH}) = q_1 \exp(q_2 C'_{OH}) \qquad (A.11)$$

where $q_1 = 0.43\ \mu m^2/\text{hr}$ and $q_2 = 1.0$ (dimensionless, since C'_{OH} is normalized).

H-OH ion diffusion

It was found that either a constant D_{HOH} or a concentration dependent $D_{HOH}(C'_{HOH})$ (same function as equation A.11) could be used since both lead to simulated results that matched the Δn_s versus t_a curve of sample 81. For a constant diffusion coefficient, D_{HOH} = 1 μm^2/hr. For a concentration dependent function, $D_{HOH}(C'_{HOH}) = 0.2 \exp(C'_{HOH})$ μm^2/hr. Depending on which D_{HOH} is used, the values of some of the other constants (i.e. $p_1, p_2, etc.$) will change slightly, for optimal results.

H-OH to OH ion conversion

Several equations describing the conversion process were tested. The most successful (i.e. producing profiles that were the closest match to those of sample 81) was equation A.2 described earlier in Section A.1:

$$\frac{\partial C'_{OH}(z,t)}{\partial t} = -\frac{\partial C'_{HOH}(z,t)}{\partial t} = \frac{p_1 C'_{HOH}(z,t)}{p_2 C'_{OH}(z,t) + 1} \qquad (A.12)$$

The rate of conversion is linearly dependent on the H-OH ion concentration and inversely dependent on the OH ion concentration. Here, $p_1 = 0.55\ hr^{-1}$, and $p_2 = 0.2$.

Simulation Results

It was possible to simulate the change in the surface index increase Δn_s with annealing time t_a - the initial rise, the peak, and the decline (see Figure A.3) - with some accuracy. Unfortunately, the model was not as successful at simulating changes in the depth d (Figure A.4) or at simulating the IWKB profiles of sample 81 (Figure A.5), despite trying numerous equations and constants for the diffusion and conversion processes.

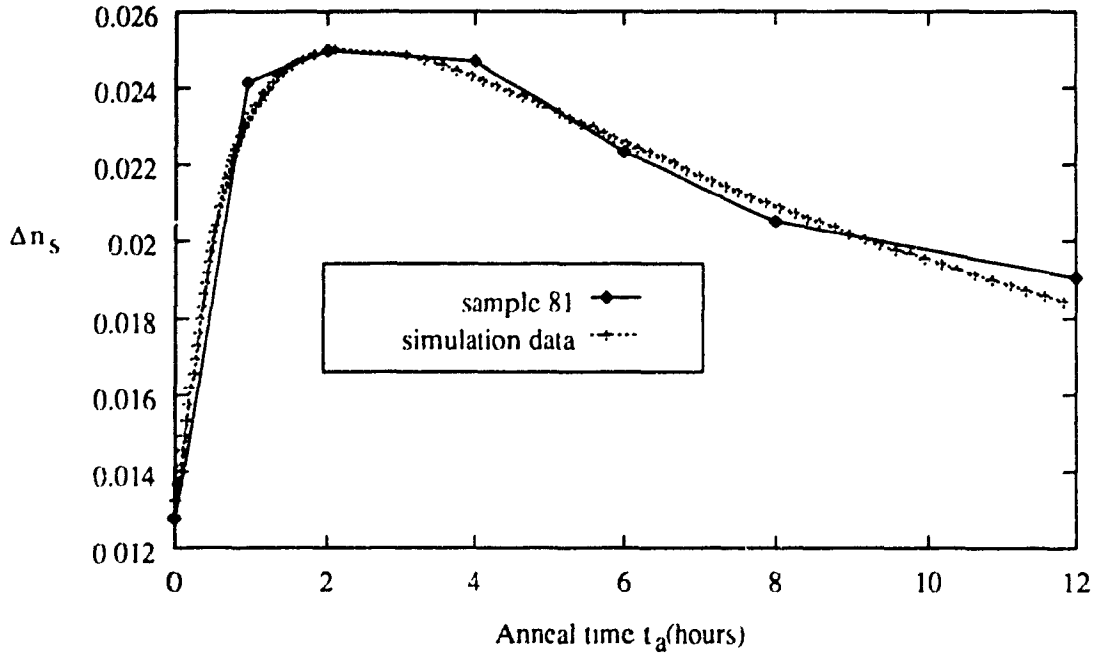

Figure A.3: Δn_s versus t_a: simulation data compared to sample 81

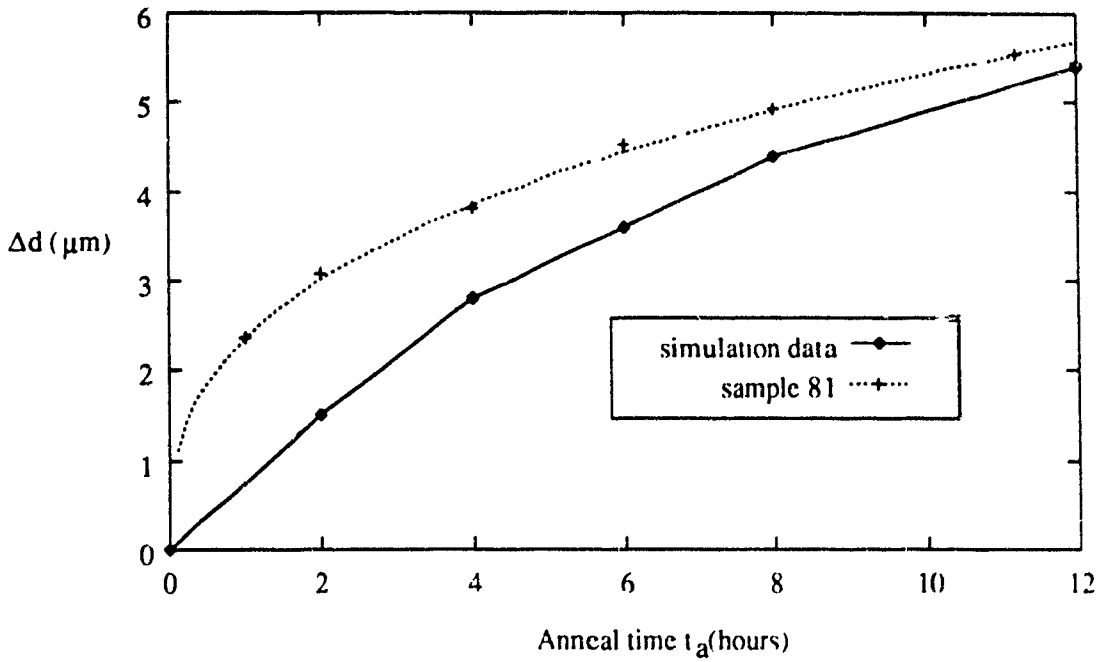

Figure A.4: Δd versus t_a simulation data compared to sample 81

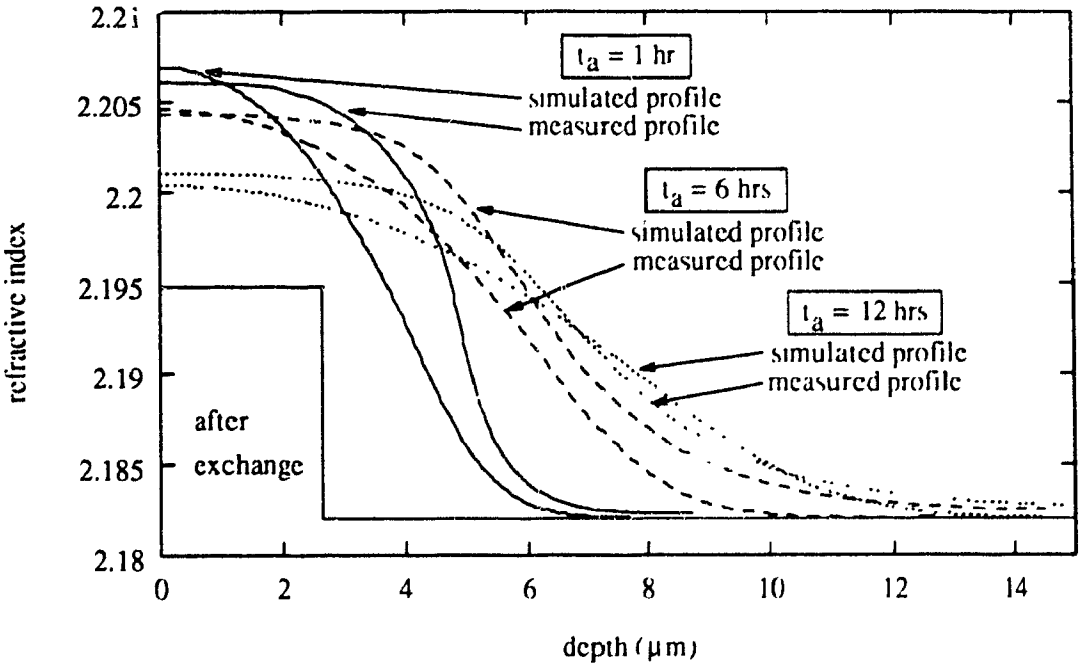

Figure A.5: Simulated profiles compared to IWKB profiles of sample 81

Discussion

The annealing model correctly simulates the change in Δn_s, but is not accurate for Δd or the profile shape. This prompts the question: where is the model flawed?

- OH diffusion: The effect of distinct phases of $H_xLi_{1-x}TaO_3$, and the effect of both lithium atoms and H-OH ions were not taken into account. The diffusion coefficient may depend on much more than the concentration of OH ions.
- H-OH diffusion: The diffusion mechanisms of H-OH ions are not known, and again, the diffusion coefficient function may be highly complex.
- H-OH to OH ion conversion: The rate conversion equation was simple and based on intuition. Possibly it has a space dependence (i.e. it depends on the concentration at several points) or perhaps a dependence on the slope of the concentration profiles.

Unfortunately, because the model is flawed, any conclusions based on the results of this simulation exercise are tenuous. Nonetheless, the fact that the model is successful at simulating the change in Δn_s indicates that parts of the model are correct. This exercise has laid the foundation for further work, having outlined the essential features of modelling annealing in $LiTaO_3$, and charted successful avenues of pursuit. With more testing and new findings in this area, an accurate model may yet be found.

Bibliography

[1] T. Tamir, ed., Topics in Applied Physics Volume 7: Integrated Optics, Springer-Verlag, New York, 1986.

[2] J.L. Jackel, C.E. Rice, and J.J. Vaselka, "Proton-exchange for high index waveguides in $LiNbO_3$", Appl. Phys. Lett. **41**, 607 (1982).

[3] W.B. Spillman, N.A. Sanford, and R.A. Soref, "Optical waveguides in $LiTaO_3$ formed by proton-exchange", Opt. Lett. **8**, 497 (1983).

[4] J.L. Jackel, "Proton-exchange: past, present, and future" in SPIE Vol. 1583, Integrated Optical Circuits, 54-63 (1991).

[5] K.K. Wong, "Integrated optical waveguides and devices fabricated by proton exchange: a review", in SPIE Vol. 993, Integrated Optical Circuit Engineering VI, 13-25 (1988).

[6] K. Tada, T. Murai, T. Nakabayashi, T. Iwashima, and T. Ishikawa, "Fabrication of $LiTaO_3$ optical waveguides by H+ exchange method", Jap. J. Appl. Phys. **26**, 503-4 (1987).

[7] Y.S. Li, K. Tada, T. Murai, and T. Yuhara, "Electrooptic coefficient r_{33} in proton-exchanged z-cut $LiTaO_3$ waveguides", Jap. J. Appl. Phys. **28**, L263-5 (1989).

[8] Y.S. Li, T. Yuhara, K. Tada, and Y. Sakaguchi, "Characteristics of low propagation loss $LiTaO_3$ optical waveguides proton-exchanged in pyrophoshoric acid", in 'Integrated Photonics Research 1990', 141 (1990).

[9] V.V. Atuchin and T.I. Zakhar'yash, "Investigation of H:$LiTaO_3$ optical waveguides", Sov. Phys. Tech. Phys. **29**, 581 (1984).

[10] G.L. Yip and J. Nikolopoulos, "Characterisation of proton- exchange and annealed proton-exchanged planar waveguides in z-cut $LiNbO_3$", IEE Proceedings-J **138**, 389 (1991).

[11] H. Nishihara, M. Haruna, and T. Suhara, Optical Integrated Circuits, McGraw-Hill Book Company, 1985, New York.

[12] H. Kogelnik and V. Ramaswamy, "Scaling rules for thin-film optical waveguides", Appl. Opt. **13**, 1857-62 (1974).

[13] G.B. Hocker and W.K. Burns, "Modes in diffused optical waveguides of arbitrary index profile", J. Quant. Elect. **JQE-11**, 270-6 (1975).

[14] R.S. Weis and T.K. Gaylord, "Lithium niobate: Summary of physical properties and crystal structure", Appl. Phys. A **37**, 191-203 (1985).

[15] From information brochure supplied by Crystal Technologies Inc., (415) 856-7911.

[16] J.M. Hammer and W. Phillips, "Low-loss single mode optical waveguides and efficient high speed modulators of $LiNb_xTa_{1-x}O_3$ on $LiTaO_3$", Appl. Phys. Lett. **24**, 545-7 (1974).

[17] V. Ramaswamy and R.D. Standley, "Growth strains and losses in Nb-diffused $LiTaO_3$ optical film waveguides", Appl. Phys. Lett. **26**, 10-12 (1975).

[18] S.K. Sheem, W.K. Burns, and A.F. Milton, "Leaky-mode propagation in Ti-diffused $LiNbO_3$ and $LiTaO_3$ waveguides", Opt. Lett. **3**, 76-8 (1978).

[19] V.V. Atuchin, K.K. Ziling, and D.P. Shipilova, "Investigation of optical waveguides fabricated by titanium diffusion in $LiTaO_3$", Sov. J. Quant. Elect. **14**, 671-4 (1984).

[20] D.W. Yoon and O. Eknoyan, "Characterization of vapor diffused Zn:$LiTaO_3$ optical waveguides", J. Lightwave Tech. **JLT-6**, 877-80 (1988).

[21] B. Chen and A.C. Pastor, "Elimination of LiO_2 outdiffusion waveguide in $LiNbO_3$ and $LiTaO_3$", Appl. Phys. Lett. **30**, 570-1 (1977).

[22] J.L. Jackel, D.H. Olson, and A.M. Glass, "Optical damage resistance of monovalent ion diffused $LiNbO_3$ and $LiTaO_3$ waveguides", J. Appl. Phys. **52**, 1855-6 (1981).

[23] J. Noda, T. Saku, and N. Uchida, "Fabrication of optical waveguiding layer in $LiTaO_3$ by Cu diffusion", Appl. Phys. Lett. **25**, 308-310 (1974).

[24] J.L. Jackel, "Optical waveguides in $LiTaO_3$: silver lithium ion exchange", Appl. Opt. **19**, 1996-9 (1980).

[25] J.L. Jackel, "High Δn waveguides in $LiNbO_3$: thallium lithium ion exchange", Appl. Phys. Lett. **37**, 739-41 (1980).

[26] T. Findakly, P. Suchoski, and F. Leonberger, "High quality $LiTaO_3$ integrated optical waveguides and devices fabricated by the annealed proton exchange technique", Opt. Lett. **13**, 797-9 (1988).

[27] T. Findakly, P. Suchoski, and F. Leonberger, "High optical power performance of high quality $LiTaO_3$ integrated optical waveguide devices" in SPIE Vol. 1177, Integrated Optics and Optoelectronics, 312-6 (1989).

[28] K.K. Wong, T.G. Palanisamy, K.P. Dimitrov-Kuhl, and H. van de Vaart, "High performance proton-exchange $LiTaO_3$ devices for integrated optical sensor applications" in SPIE Vol. 1177, Integrated Optics and Optoelectronics, 40-7 (1989).

[29] K.K. Wong, A.C. O'Donnell, I.A. Wood, and N.J. Parsons, "Integrated optical Mach-Zehnder interferometers in $LiTaO_3$ fabricated by proton-exchange", in Proc. of the Fourth European Conference on Integrated Optics, Glasglow, Scotland, 123-6 (1987).

[30] K.K. Wong, K.M. Killian, K.P. Dimitrov-Kuhl, M. Long, J.T. Fleming, and H. van de Vaart, "Proton-exchanged X-cut $LiTaO_3$ fiber optic gyro chips" in SPIE Vol. 1374, Integrated Optics and Optoelectronics II, 278-86 (1990).

[31] J.F. Duffy, S.M. Al-Shukri, and R.M. De La Rue, "Guided-wave acousto-optic interaction on proton-exchanged lithium tantalate", Elect. Lett. **23**, 849-50 (1987).

[32] N.A. Sanford, J.A. Aust, K.J. Malone, D.R. Larson, and A. Roshko, "Nd:$LiTaO_3$ waveguide laser", Opt. Lett. **17**, 1578-80 (1992).

[33] K. Yamamoto, K. Mizuuchi and T. Taniuchi, "Quasi-phase-matched second harmonic generation in a $LiTaO_3$ Waveguide", J. Quantum Elect. **JQE-28**, 1909-11 (1992).

[34] D.F. Clark, A. Nutt, K.K. Wong, P. Laybourn, and R.M. De La Rue, "Characterization of proton-exchange slab optical waveguides in z-cut $LiNbO_3$", J. Appl. Phys. **54**, 6218-20 (1983).

[35] C. Canali, A. Carnera, G. Della Mea, P. Mazzoldi, S.M. Al Shukri, A.C.G. Nutt, and R.M. De La Rue, "Structural characterization of proton exchanged $LiNbO_3$ optical waveguides", J. Appl. Phys. **59**, 2643-9 (1986).

[36] V.A. Ganshin, Yu.N. Korkishko, and T.V. Morozova, "Fabrication of H:$LiNbO_3$ optical waveguides", Sov. Phys. Tech. Phys. **30**, 1313 (1985).

[37] K. Yamamoto and T. Taniuchi, "New proton-exchange technique for $LiNbO_3$ waveguide fabrication" in OFC/IOOC'87, paper TUH2, 65 (1987).

[38] N. Goto and G.L. Yip, "Characterisation of proton-exchange and annealed $LiNbO_3$ waveguides with pyrophosphoric acid", Appl. Opt. **28**, 60-5 (1989).

[39] J. Nikolopoulos and G.L. Yip, "Characterisation of proton-exchange optical waveguides in z-cut $LiNbO_3$ using pyrophosphoric acid" in SPIE Vol. 1177, Integrated Optics and Optoelectronics, 21 (1989).

[40] A. Loni, R.W. Keys, R.M. De La Rue, M.A. Foad, and J.M. Winfield, "Optical characterisation of z-cut proton exchanged $LiNbO_3$ waveguides fabricated using orthophosphoric and pyrophosphoric acid", IEE Proc. **136**, 297-300 (1989).

[41] M.A. Foad, A. Loni, R.W. Keys, J.M. Winfield, and R.M. De La Rue, "Proton exchanged lithium niobate optical waveguides made from phosphoric acids: detailed studies and comparisions with guides made with benzoic acid" in SPIE Vol. 1177, Integrated Optics and Optoelectronics, 31-9 (1989).

[42] E.Y.B. Pun, "Recent development of proton-exchanged waveguides and devices in lithium niobate using phosphoric acid" in SPIE Vol. 1374, Integrated Optics and Optoelectronics II, 2-13 (1990).

[43] E.Y.B. Pun, T.C. Kong, P.S. Chung, and H.P. Chan, "Index profile of proton-exchanged waveguides in $LiNbO_3$ using pyrophosphoric acid", Elect. Lett. **26**, 81 (1990).

[44] C. Ziling, L. Pokrovskii, N. Terpugov, M. Kuneva, I. Savatinova, and M. Armenise, "H:$LiNbO_3$ optical waveguides made from pyrophosphoric acid" in SPIE Vol. 1583, Integrated Optical Circuits, 90-101 (1991).

[45] E.Y.B. Pun, S.A. Zhao, K.K. Loi, and P.S. Chung, "Proton-exchanged $LiNbO_3$ optical waveguides using stearic acid", IEEE Phot. Tech. Lett. **3**, 1006-8 (1991).

[46] V.A. Ganshin, Yu.N. Korkishko, T.V. Morozova, and V.V. Saraikin, "The study of proton exchange in lithium tantalate crystals", Phys. Stat. Sol. A **114**, 457-65 (1989).

[47] E.Y.B. Pun, K.K. Loi, and P.S. Chung, "Index profile of proton-exchanged waveguides in lithium niobate using cinnamic acid", Elect. Lett. **27**, 1282-3 (1991).

[48] E.Y.B. Pun, K.K. Loi, and P.S. Chung, "Experimental studies of proton-exchanged waveguides in lithium niobate using toluic acid", in SPIE Vol. 1583, Integrated Optical Circuits, 64-70 (1991).

[49] V.A. Ganshin and Yu.N. Korkishko, "Proton-exchange in lithium niobate and lithium tantalate single crystals: regularities and specific features", Phys. Stat. Sol. A **119**, 11-25 (1990).

[50] M. De Micheli, J. Botineau, S. Neveu, P. Sibillot, and D.B. Ostrowsky, "Independent control of index and profiles in proton-exchanged lithium niobate guides", Opt. Lett. **8**, 114 (1983).

[51] J.T. Cargo, A.J. Filo, M.C. Hughes, V.C. Kannan, F.A. Stevie, J.A. Taylor, and R.J. Holmes, "Characterization of sulfuric acid proton-exchanged lithium niobate", J. Appl. Phys. **67**, 627-33 (1990).

[52] K.K. Wong, "An experimental study of dilute melt proton- exchange waveguides in x- and z- cut lithium niobate", GEC J. of Research **3**, 243 (1985).

[53] Y.S. Son, H.J. Lee, Y.K Jhee, S.Y. Shin, and B.G. Kim, "Fabrication of $LiNbO_3$ channel waveguides using water", IEEE Photonics Tech. Lett. **4**, 457-9 (1992).

[54] A.C.G. Nutt, K.K. Wong, D.F. Clark, P.J.R. Laybourn, and R.M. De La Rue, "Proton-exchange lithium niobate slab and stripe waveguides: Characterization and comparisons", in 2nd European Conference in Integrated Optics 1983, 53 (1983).

[55] W. Bollman, "Diffusion of hydrogen (OH^- ions) in $LiNbO_3$ crystals", Phys. Stat. Sol. (a) **104**, 643-8 (1987).

[56] J. Crank, The Mathematics of Diffusion, Oxford University Press, London, 1956.

[57] W. Bollman and H.J. Stohr, "Incorporation and mobility of OH^- ions in $LiNbO_3$ crystals", Phys. Stat. Sol. (a) **39**, 177-81 (1977).

[58] C.E. Rice, "The structure and properties of $Li_{1-x}H_xNbO_3$", J. Sol. St. Chem. **64**, 188-99 (1986).

[59] C.E. Rice and J.L. Jackel, "$HNbO_3$ and $HTaO_3$: New cubic perovskites prepared from $LiNbO_3$ and $LiTaO_3$ via ion exchange", J. Sol. St. Chem. **41**, 308-14 (1982).

[60] M. Minakata, K. Kumagai, and S. Kawakami, "Lattice constant changes and electro-optic effects in proton-exchanged $LiNbO_3$ optical waveguides", Appl. Phys. Lett. **49**, 992-4 (1986).

[61] V.A. Ganshin, Yu.N. Korkishko, and T.V. Morozova, "Properties of proton-exchanged optical waveguiding layers in $LiNbO_3$ and $LiTaO_3$", Phys. Stat. Sol. A **110**, 397-402 (1988).

[62] V.A. Gan'shin, Yu.N. Korkishko, T.V. Morozova, and V.Z. Petrova, "Formation and properties of H:$LiTaO_3$ optical waveguides", Sov. Phys. Tech. Phys. **34**, 884-5 (1989).

[63] A. Loni, G. Hay, R.M. De La Rue, and J.M. Winfield, "Proton- exchanged $LiNbO_3$ waveguides: The effects of post-exchange annealing and buffered melts as determined by infrared spectroscopy, optical waveguide measurements, and hydrogen isotopic exchange reactions", J. Lightwave Tech. **JLT-7**, 911-9 (1989).

[64] I. Savatinova, M. Kuneva, Z. Levi, V. Atuchin, K. Ziling, and M. Armenise, "Proton-exchange in $LiTaO_3$ with different stoichiometric composition" in SPIE Vol. 1374, Integrated Optics and Optoelectronics II, 37-46 (1990).

[65] S.T. Vohra, A.R. Mickelson, and S.E. Asher, "Diffusion characteristics and waveguiding properties of proton-exchanged and annealed $LiNbO_3$ channel waveguides", J. Appl. Phys. **66**, 5161-74 (1989).

[66] C. Canali, A. Carnera and G. Arnold, "Li and H concentration profiles in $LiNbO_3$ waveguides measured by nuclear techniques", in IOOC-ECOC'85, p.13-6, 1985.

[67] T. Yuhara, K. Tada, and Y.S. Li, "Anomalous refractive index changes in proton-exchanged $LiTaO_3$ optical waveguides - effects of annealing and dilution of proton source" in 'Technical Digest of 3rd Microoptics Conference', MOC '91 Yokohama', paper D3 (1991).

[68] A. Yi-Yan, "Index instabilities in proton-exchanged $LiNbO_3$ waveguides", Appl. Phys. Lett. **42**, 633-5 (1983).

[69] K.K. Wong, N.J. Parsons, A.R. Oldroyd, and A.C. O'Donnell, "High quality optical waveguides in $LiNbO_3$ by dilute melt proton-exchange" in IOOC-ECOC'85, 59-62 (1985).

[70] M.L. Bortz and M.M. Fejer, "Linear and nonlinear optical properties of annealed proton-exchanged lithium niobate waveguides" in 'Integrated Photonics Research 1992', 10-11 (1992).

[71] C.E. Rice, J.L. Jackel, and W.L. Brown, "Measurement of the deuterium concentration profile in a deuterium exchanged $LiNbO_3$ crystal", J. Appl. Phys. **57**, 4437-40 (1985).

[72] M.M. Howerton, P.R. Skeath, A.S. Greenblatt, and W.K. Burns, "Experimental determination of refractive index dependence on hydrogen concentration in proton-exchanged $LiNbO_3$", in Integrated Photonics Research 1990, 140 (1990).

[73] V. Neuman, O. Parriaux, and L.M. Walpita, "Double-alkali effect: Influence on index profile of ion-exchanged waveguides", Elect. Lett. **15**, 704-6 (1979).

[74] S.T. Vohra and A.R. Mickelson, "The effects of finite melt volume on Proton Exchanged Lithium Niobate", J. Lightwave Tech. **JLT-6**, 1848-53 (1988).

[75] S.M. Al-Shukri, J.F. Duffy, R.M. De La Rue, G. Mazzi, A. Carnera, and M.N. Armenise, "Single mode planar and stripe waveguides by proton exchange in lithium tantalate and lithium niobate" in SPIE Vol. 651, Integrated Optical Circuit Engineering III, 20-5 (1986)

[76] M. De Micheli, D.B. Ostrowsky, J.P. Barety, C. Canali, A. Carnera, G. Mazzi, and M. Papuchon, "Crystalline and optical quality of proton- exchanged waveguides", J. Lightwave Tech. **JLT-4**, 743-4 (1986).

[77] W. Hou, W. Hua, Y. Zhang, and H. Tan, "Possible mechanism for increase of extraordinary refractive index in proton-exchanged $LiNbO_3$ waveguides", Elect. Lett. **27**, 755 (1991).

[78] M.M. Howerton, W.K. Burns, P.R. Skeath, and A.S. Greenblatt, "Dependence of refractive index on hydrogen concentration in proton-exchanged $LiNbO_3$", J. Quantum Elect. **JQE-27**, 593-600 (1991).

[79] J. Nikolopoulos and G.L. Yip, "Theoretical modelling and characterisation of annealed proton-exchanged planar waveguides in z-cut $LiNbO_3$", J. Lightwave Tech. **JLT-33**, 111 (1991).

[80] T. Yuhara, and K. Tada, "Effects of benzoic acid dilution on proton-exchanged $LiTaO_3$ optical waveguides" in 'Integrated Photonics Research 1992', 251-5 (1992).

[81] P.G. Suchoski, T.K. Findakly, and F.J. Leonberger, "Stable low-loss proton-exchanged $LiNbO_3$ waveguide devices with no electro-optic degradation", Opt. Lett. **13**, 1050 (1988).

[82] A. Loni and R M. De La Rue, "Proton-exchanged $LiNbO_3$ waveguides: relevance of atmospheric environment during annealing", Appl. Opt. **31**, 5096-8 (1992).

[83] E.Y.B. Pun, K.K. Loi, S.A. Zhao, and P.S. Chung, "Annealing properties of proton-exchanged waveguides in $LiNbO_3$ fabricated using stearic acid" in SPIE Vol. 1583, Integrated Optical Circuits, 102-8 (1991).

[84] W.E. Lee, N.A. Sanford, and A.H. Heuer, "Direct observation of structural phase changes in proton-exchanged $LiNbO_3$ waveguides using transmission electron microscopy", J. Appl. Phys. **59**, 2629-33 (1986).

[85] A. Loni, R.M. De La Rue, and J.M. Winfield, "Proton-exchanged, lithium niobate planar optical waveguides: Chemical and optical properties and room-temperature hydrogon isotopic exchange reactions", J. Appl. Phys. **61**, 64-7 (1987).

[86] X.F. Cao, R.V. Ramaswamy, and R. Srivastava, "Characterization of annealed proton-exchanged $LiNbO_3$ waveguides for nonlinear frequency conversion", J. Lightwave Tech. **JLT-10**, 1302-13 (1992).

[87] M.L. Bortz and M.M. Fejer, "Annealed proton-exchanged $LiNbO_3$ waveguides", Opt. Lett. **16**, 1844-6 (1991).

[88] T. Yuhara, Y.S. Li, and K. Tada, "Anomalous refractive index change in proton exchanged $LiTaO_3$ optical waveguides after annealing", in 'Integrated Photonics Research 1991', 62-3 (1991).

[89] Deltronic Crystals Inc., 60 Harding Ave., Dover, New Jersey 07801, U.S.A.; tel: (401) 553-3040, fax: (401) 553-4532; Jeff Brunner.

[90] P.K. Tien and R. Ulrich, "Theory of prism-film coupler and thin- film light guides", J. Opt. Soc. Amer. **60**, 1325 (1970).

[91] Meyer-Arendt, Jurgen R. Introduction to Classical and Modern Optics. Prentice Hall: New Jersey, 1989.

[92] I.P. Kaminow and L.W. Strulz, "Loss in cleaved Ti-diffused $LiNbO_3$ waveguides", Appl. Phys. Lett. **33**, 62 (1978).

[93] H.P. Weber, F.A. Dunn, and W.N. Leibolt, "Loss measurements in thin film optical waveguides", Appl. Opt. **12**, 755 (1973).

[94] Y.H. Won, P.C. Jaussaud, and G.H. Chartier,"Three-prism loss measurements of optical waveguides", Appl. Phys. Lett. **37**, 269 (1980).

[95] Y. Okamura et al,"Measuring mode propagation losses of integrated optical waveguides: a simple method", Appl. Opt. **22**, 3892 (1983).

[96] G. Bach, Notes from course on Numerical Analysis given at McGill University, Montreal, Dept. of Electrical Engineering.

[97] G.L. Yip and J. Albert, "Characterization of planar optical waveguides by K^+-ion exchange in glass", Opt. Lett. **10**, 151 (1985).

[98] K.S. Chiang, "Construction of refractive-index profiles of planar dielectric waveguides from the distribution of effective indexes", J. Lightwave Tech. **JLT-3**, 385-91 (1985).

[99] J.M. White and P.F. Heidrich, "Optical waveguide refractive index profiles determined from measurement of mode indices: a simple analysis", Appl. Opt **15**, 151-5 (1976).

[100] Ghez, R. A Primer of Diffusion Problems. John Wiley and Sons: New York, 1988.

[101] M.M. Howerton and W.K. Burns, "Photorefractive Effects in Proton-Exchanged $LiTaO_3$ Optical Waveguides", J. Lightwave Tech. **JLT-10**, 142-9 (1993).